University of Cape Town

Faculty of Engineering and the Built Environment

Mechanical Engineering/Centre for Materials Engineering

FEASIBILITY STUDY INTO THE USE OF DIGITAL IMAGE CORRELATION FOR CREEP STRAIN MONITORING OF FOSSIL POWER PLANT WELDS

By
Nicolas Cardenas
Supervisor: Professor Robert Knutsen
Co-supervisor: Dr Thorsten Becker
April 2018

A dissertation submitted to the Faculty of Engineering and the Built Environment, at the University of Cape Town, in fulfilment of the degree of Master of Science in Engineering

Abstract

The life span of high temperature power plant pipework is principally a function of material creep damage – an irreversible plastic deformation of the material when subjected to temperatures and loads beyond a certain threshold. Within Eskom, the South African parastatal power utility, creep damage is primarily quantified by way of Metallographic Replication (replicas). This is a quasi Non-Destructive Examination (NDE) technique that looks at the microstructure of the sample in question. Although well-known and used extensively, replicas, as with any technology, have their shortcomings. Extracting of replicas and their subsequent analysis are manual processes that inherently suffer from subjectivity. Furthermore, storage and archiving of vast quantities of physical replica slides for future reference is cumbersome – a challenge that digitisation can address.

The aforementioned vulnerability to analysis subjectivity and benefits of digitisation are areas which a technology known as Digital Image Correlation (DIC) - a non-contact, full field, deformation measurement technique - can potentially address. Some research has been done on using DIC for power plant creep measurement; however literature quantifying its performance in this specific application is scarce. This study thus looks into setting up a DIC system optimised for measuring strain in an area of the pipework welds known as the Heat Affected Zone (HAZ) – the weakest part of the weldment. The achievable accuracy is established and the major parameters that affect DIC accuracy are investigated, elucidating the trade-offs between optimising each. In addition, two scenarios exist for the acquisition of DIC measurement data from a plant: when the plant is operating (online); or when the plant is shut down for maintenance (offline). The encumbrance of imaging a hot surface makes the former scenario the more demanding, and was thus investigated. This data was subsequently used to substantiate whether DIC has the potential to be used online (i.e. at elevated temperatures) or is limited to use during shut downs

Acknowledgements

I'd like to thank Eskom for the opportunity to pursue this qualification. The company originally offered me a bursary for my undergraduate degree, which relieved the financial pressure on my family, particularly when my sister also started university. Eskom may be going through troubled waters as the writing of this work is concluding, but they have forever changed the quality of my life and that of my family through supporting me through continued education.

Carving out a work from a clean slate is painful, and I thank Dr Thorsten Becker and Professor Robert Knutsen for their patience in guiding me on how to use the chisel and hammer of postgraduate research.

Through this process, I am very thankful to have had the companionship of friends and family in the times of hardship, not only with this work but also in life's inevitable highs and lows. A man is not an island. I am very thankful to Trisha Rasiawan and Ryan Matthews who were on this journey with me from the start. I am forever grateful for my mother Liliana, my father Fernando and my sister Amanda, whom I love dearly.

Declaration

I know the meaning of plagiarism and declare that all the work in the document, save for that which is properly acknowledged, is my own. This thesis/dissertation has been submitted to the Turnitin module (or equivalent similarity and originality checking software) and I confirm that my supervisor has seen my report and any concerns revealed by such have been resolved with my supervisor.

Name: NICOLAS CARDENAS

Signature: Signed by candidate

Date: 2018/10/17

Contents

1 Introduction

1.1 Background and Aims

Socio-economically, electricity, and the utilities that supply it, support the well-being of a country. It facilitates necessities such as lighting, warmth and cooking and enables intangibles such as education via the use of computers and the internet. An electricity utility in large part also supports the Gross Domestic Product (GDP) growth of a country - electricity being an input cost to many businesses. The maintenance of equipment within such a utility's assets is therefore paramount to reliable operation and its subsequent ability to deliver a consistent electricity supply. Eskom is such a parastatal utility, supplying the majority of electrical power capacity to South Africa as well as trading within the Southern African Power Pool (SAPP).

The maintenance of Eskom's generating assets is predominantly achieved by way of a tiered regime, concentrating resources on equipment that poses significant safety, availability and economic risks to the business. Integrity assessment of this high-risk equipment is therefore essential to optimise the said maintenance; and becomes increasingly important when the assets age or are of an advanced design. A large proportion of Eskom's thirteen coal-fired stations have reached, or are reaching, the end of their design lives but will be run further as a result of strategic business decisions. Two additional stations (amongst the biggest coal-fired in the world) are at the time of this writing being phased into commercial operation. They are of a design that operates at more severe parameters than the aforementioned thirteen, improving their thermal efficiency and reducing greenhouse gas emissions to curb climate change. Considering the above, Eskom places high value on the integrity assessment of their equipment to hedge their risks, and ultimately bolster South Africa socio-economically.

Within a typical fossil-fuelled power station, high energy steam is transported in specialised pipework from the boiler to the turbine, which in turn powers the generator to produce electricity. Such a power station typically constitutes six of these turbine-boiler units in the Eskom context, culminating in several kilometres of high-energy pipework that is welded together. Rupture of such pipework is generally unacceptable and thus their integrity assessment is an area of focus for Eskom. The predominant concerns in high-energy components, such as the said pipework, are: fatigue, thermal fatigue, creep-fatigue and creep (Viswanathan 2000). Of these, creep, which is a straining of the material at elevated temperatures and stresses, is a commonly assessed damage mechanism within the Eskom power stations. Several techniques are available to monitor and quantify creep, the most prevalent used in Eskom being metallographic replication - a microstructure characterisation technique.

Advances in a given technology often unlock its applicability in several fields. For instance, advances in the steam engine propelled it from powering reciprocating pumps, to transportation, to modern power plant steam turbines. In a similar vein, advances in camera technology and digital image processing have enabled a technology, known as Digital Image Correlation (DIC), for measuring material surface strains in several fields. DIC tracks the deformation of surface features (termed a speckle pattern) in two or more consecutive digital images of the said surface, to ultimately calculate strain. There exists the possibility of using DIC as a complementary technology to the aforementioned metallographic replication for the integrity assessment of creep strain in pipework,

possibly overcoming some of metallographic replication's shortcomings. Information on what performance can be expected of DIC for this application, and whether the technology is suitable for in-situ power station environments is however scarce. In particular, there exist questions with regard to its practical accuracy and precision in the context of measuring creep-strain. The effects of heat, as might be experienced when performing in-situ DIC measurements on a running power plant, are also a grey area. It is into this space that this work aims to position itself, ascertaining insight into the feasibility and limitations of DIC for strain measurements in a power plant context. The pipework weld area, in particular, is focused upon as it is the weakest link in the pipework system. It is envisioned that insights from this study contribute to Eskom's decision on whether to pursue further research, testing and development of DIC for their use.

This work was commissioned under the Eskom Power Plant Engineering Institute (EPPEI), a programme launched by Eskom to upskill its employees at a postgraduate level. The author of this work is an Eskom employee with experience as a Turbine Plant Systems Engineer. Within this role, work was done on the replacement of creep-damaged pipework leading into the main turbines, and this set the stage for this dissertation. This postgraduate work was carried out at the University Of Cape Town (UCT) within the Centre for Materials Engineering (CME). Extensive knowledge on DIC exists within the Material Engineering group at the University of Stellenbosch (SUN) and thus the majority of testing was done there. Supervision for this work was drawn from both UCT and SUN.

1.2 Objectives

1. Conduct a literature survey on the concepts around Digital Image Correlation and its use for creep strain measurements. This will explore the current state of this field of work and form a foundation on which informed decisions on apparatus selection can be made. A first-principles understanding of the field will also facilitate the interpretation of the results.
2. Set up a DIC system in a configuration that models what would likely be used in a creep-strain measuring application. There are several components within a DIC system and several options for each of the component. The specific combination of selected components yields the characteristics of the system, which in this work needs to be optimised for creep-strain measurement.
3. Additional to equipment selection in Objective 2, the preparation of the surface that DIC will analyse is of high importance. The application of a so-called speckle pattern to the surface and the characteristics of this speckle pattern have significant influences on the performance of the system. As such, this work will create a toolbox to analyse speckle patterns such that:
    a. Assurance is had that the speckle pattern used adheres to what research recommends is optimal.
    b. Assurance is had that the imaging system is correctly set up to optimally capture the speckle pattern – image quality control.
    c. As an additional benefit, a unique fingerprint (i.e. characterisation) of the pattern can be ascertained for referencing purposes.
4. Select an appropriate speckle pattern for the DIC system configuration chosen in Objective 2. This will be informed by the outputs of Objective 3.

5. Ascertain the strain measuring performance of DIC in ideal laboratory conditions, accounting for the several parameters that can be varied and the consequential trade-offs as a result of varying the said parameters.
6. Investigate what effects high (power plant operating) temperature will have on the DIC accuracy established in Objective 5. This data is to give insight into the plausibility of performing DIC measurement online (when the plant is running).

1.3 Scope and Limitations

- This work will use DIC technology to measure strains in an area commensurate with the size of the heat affected zone (HAZ) of a power plant pipework circumferential weld.
- The DIC technology is tested with homogeneous deformation fields as a simplifying assumption of the mode in which creep-strained pipe welds deform.
- Power station pipework in-situ speckle patterns would need to be resilient to adverse conditions for extended periods of time. The longevity of the speckle patterns is excluded from the scope of this work.
- The effects of surface temperature on DIC were simulated such that the geometry, orientation and temperature were representative of pipework known to have undergone creep damage.
- The effects of temperature were looked at in isolation, with no external strain applied.

1.1 Layout

This work starts with a review of published literature to unpack the concepts that will be encountered and to ascertain the current state that DIC technology finds itself in with respect to measuring creep damage. This will form the foundation upon which this work is built. An experimental methodology is next designed to address each of the objectives laid out. The justification of decisions made and challenges encountered are detailed in this section. The results are shown next, echoing the ordering of tests laid out in the experimental methodology. The discussion of the results is interwoven with the results so that the reader needn't oscillate between two sections. The findings are summarised and concluded upon, linking them back to the objectives laid out. The thesis is ended with possible future work. A collection of appendices supporting this work are also included.

2 Literature Review

This section explores and elaborates on the concepts that will be encountered in the rest of the work. It starts with a look into creep strain damage in power plant pipework and the current techniques used to characterise it. Digital Image Correlation is subsequently introduced as an alternative/complementary technique to metallographic replication. The concepts and components of Digital Image Correlation are then fleshed out for a rounded understanding of the technology as it applies to measuring strain in the context of power plant welds.

2.1 Creep and power plant pipework

Creep strain is one of the long-term degradation mechanisms in power plant pipework. It is the long-term plastic deformation of the material that is macroscopically measured as strain. The said strain is the cumulative result of an intricate interplay of mechanisms at the microstructural level, each contributing to the aggregate strain, but varying in dominance both temporally and spatially. These mechanisms are a function of the time, temperature, stress and the material in question. In their review of methods to estimate creep damage in low-alloy steel power station steam pipes, (Maharaj et al. 2009) schematically showed the effects of increasing stress and temperature as can be seen in Figure 2.1-1 (B). It can be seen that each of the curves show a similar general shape, albeit shifted. This general shape is elaborated on in Figure 2.1-1 (A), where the generic creep curve is subdivided into three regimes (primary, steady state and tertiary), culminating in component failure.

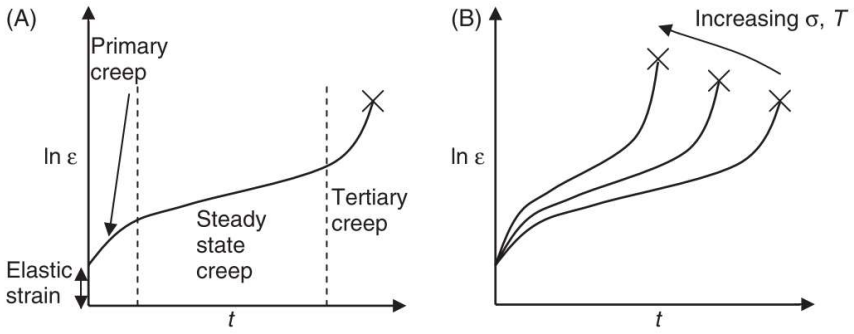

Figure 2.1-1 Creep strain versus time: (A) the three creep regimes; (B) effects of increasing temperature and stress. (Maharaj et al. 2009)

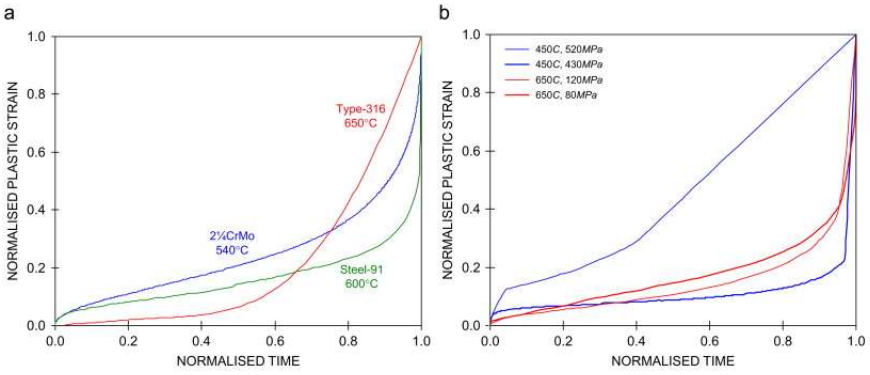

Figure 2.1-2 "Examples of creep curve shape variations for (a) 2.25CrMo, Steel-91 and Type-316 at typical application temperatures and (b) Steel-91 over a wide T, σ regime" (Holdsworth et al. 2008)

Specific examples of general creep curves described in Figure 2.1-1 (A) are shown for three different steels, as reported by (Holdsworth et al. 2008), in Figure 2.1-2 a. Note that the axes have been normalised for the sake of comparison, thus absolute time to failure for each of the steels differ. Exemplified by these curves is the differences in their gradients and duration spent in each creep regime, yet all following the same general shape. Figure 2.1-2 b illustrates the effects of temperature and stress on the strain rates for grade 91 steel, echoing what was seen schematically in Figure 2.1-1 (B).

In a steel manufacturing process, myriads of crystal lattices (termed grains), with differing orientations, nucleate upon cooling. These grains grow to meet one another at their extremities to form grain boundaries. The size, shape and crystallographic structure of these grains will be a function of the manufacturing process designed for the steel, and the said crystallographic structure correlates directly to the steel's macroscopic properties. The cooling is usually done rapidly in power plant steels to from a so-called martensitic microstructure that elicits desirable properties. As a result of the inevitable practicalities of the aforementioned manufacturing process, the crystal lattices making up each of the grains inevitably has defects in its atomic structure. The defects can be broadly grouped into three categories: point defects, line defects and planar defects.

Point defects are imperfections in the steel's atomic lattice and would typically be a missing atom in the otherwise regular lattice, termed a vacancy. Vacancies will diffuse through the crystal lattice given enough energy. Line defects are additional sheets of atoms that become wedged in an otherwise regular crystal lattice, and the edge of this additional sheet of atoms is known as a dislocation. The plastic deformation of steel will manifest itself at the atomic scale as the movement of these dislocations as the crystal lattice rearranges to accommodate a new configuration. Lastly, planar defects constitute entire adjacent crystal lattices meeting each other at oblique orientations to form the grain boundaries that were mentioned above.

The impetus for the movement of the aforementioned dislocations stem from macroscopic stress and heat applied to a material. With the application of sufficient stress to a steel, dislocations glide through the lattice, having enough energy for chemical bonds to be broken and re-bonded with other atoms in the lattice. Heat contributes additional energy to facilitate the process. Macroscopically this dislocation slip process is perceived as the material's plastic strain characteristics. The dislocations slip and interact with each other, as well as with vacancies, grain boundaries, and precipitates (that form from the steel's constituent chemical elements). These phenomena hinder dislocation movement and are thus made use of in the design of steels to alter their mechanical properties. The interaction between the dislocation slip enablers and inhibitors result in the shape of the creep strain curves seen earlier in Figure 2.1-1 and Figure 2.1-2.

Creep strain was noted in Figure 2.1-1 (A) to be categorised into three regimes - primary, secondary (or steady state) and tertiary. The primary creep stage is characterised by a steep gradient (strain rate) that tapers off rapidly. This behaviour is typically the result of the initial loading of the steel. The 2.25CrMo steel seen in Figure 2.1-2 (a) showcases the primary creep stage well. The strain rate subsequently reaches a quasi-constant strain rate which is classified as the secondary stage, and this stage occupies the largest proportion of the total creep life (Maharaj et al. 2009). In the tertiary regime, necking starts to occur which reduces load bearing area and hence increases local stresses. This exacerbates the strain rate, ultimately leading to material failure if the stress is not removed. At

the tertiary creep stage, nucleated voids become numerous within the crystal structure, grow in size, and subsequently begin to coalesce and form chains. These voids will be seen to be an important parameter in the section on Metallographic Replication.

Creep is seen to be a material degradation phenomenon that affects power plant pipework. Its rate of progression is dependent on time, temperature, stress, and material composition which affect the crystal structure of the material in question.

2.2 Creep prevalence and its quantification

Globally there is a drive to improve the efficiency of thermal power plants to reduce greenhouse gases. The United Nations Framework Convention on Climate Change (UNFCCC) considered the negative effects of greenhouse gas emissions, and in an effort to curb these effects, the Paris Agreement was put into force as of 4 November 2016 (Anon 2017). As a result, incentives (punitive and remunerative) for stakeholders operating fossil-fuelled power plants to reduce greenhouse gas emissions are becoming more prevalent. These incentives include stricter government licensing requirements and added conditions by financial houses on financing agreements.

One of the primary methods to reduce the said greenhouse gases is by increasing power plant efficiency. As is dictated by the Carnot Cycle, greater efficiency is a function of the difference between the highest (hot reservoir) and lowest (cold reservoir) temperatures within which a power plant operates. For practical reasons, it is not possible to reduce the cold reservoir temperature significantly lower than ambient conditions. Therefore, the hot reservoir temperature needs to be increased, which in a power plant context is implemented by increasing the steam temperature. For several reasons, pressure is also increased which maximises the enthalpy of the working fluid (steam).

Now prior to the drive to minimise greenhouse gas emissions, power plant designers have for many years been increasing operating temperatures and pressures to maximise efficiency for *economic* reasons as well. In their work on the history of power plants and progress in heat resistant steels, (Masuyama 2001) illustrated the aforementioned trend for Japanese power plants since circa 1950, as can be seen in Figure 2.2-1.

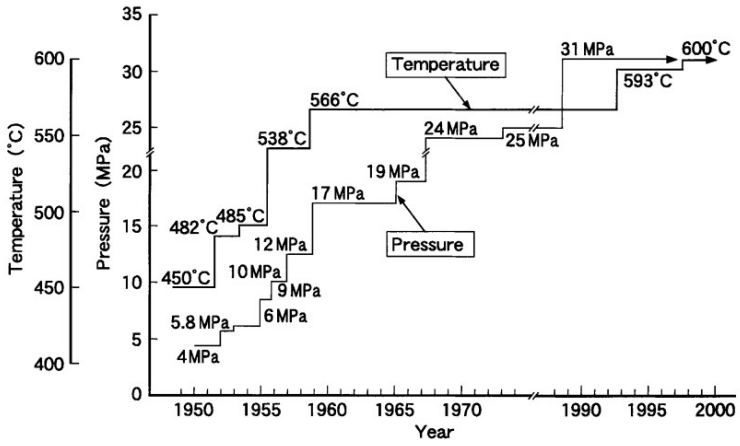

Figure 2.2-1 Trends of steam condition of power plants in Japan (Masuyama 2001)

In order to safely design power plants with increasing pipework temperatures and pressures (stresses) without significantly compromising plant operating lifetimes, metallurgists have had to design materials with higher maximum operating temperatures. In their work on creep resistant steels for power plants, (Ennis & Czyrska-Filemonowicz 2003) summarised the maximum operating temperatures for several steels based on rupture strength as can be observed in Figure 2.2-2. P92 is of the later generations of these designer steels and is seen to be capable of operating at temperatures over 85°C above older generation 1Cr0.5Mo steels. (Masuyama 1998) took this a step further and contextualised several steel's creep rupture strength in time as can be noted in Figure 2.2-3, where the upward trend in rupture strength agrees with the upward trend in operating temperatures shown in Figure 2.2-1.

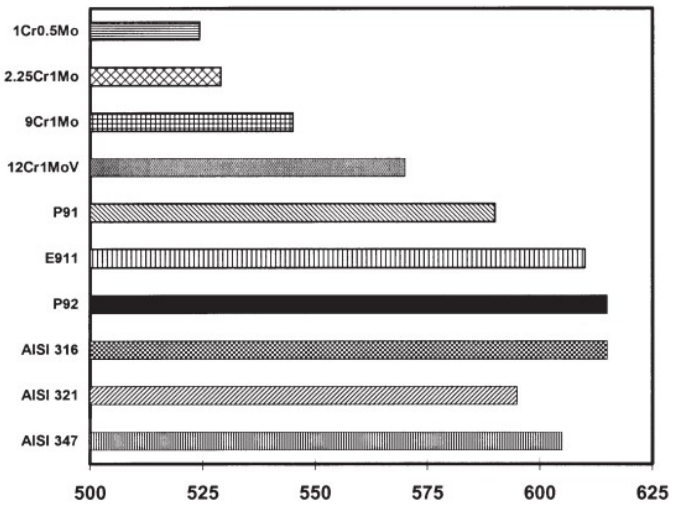

Figure 2.2-2 Maximum operating temperature in °C, based on a 100 000h average stress rupture strength of 100 MPa (Ennis & Czyrska-Filemonowicz 2003).

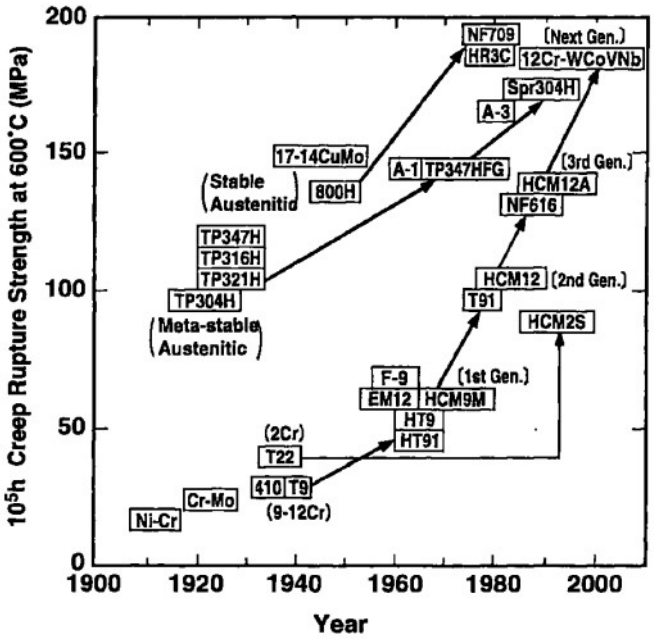

Figure 2.2-3 Historical Improvements of Creep Rupture Strength in Steels for Boilers (Masuyama 1998)

In addition to the aforementioned increasing trend in operating conditions over time, power plants may be required to run past their original design lives. Reasons for this may include maximising economic benefit from an asset; and/or operating within a constrained power capacity system, where stations cannot be taken offline without risking upsetting the power supply and demand dynamics. Figure 2.2-4 shows Eskom's thirteen coal fired stations that were in commercial operation as at 2014 – Medupi and Kusile (supercritical new builds) were still under construction at the time. It can be seen that nine of the thirteen plants had at the time already exceeded their contracted design life, with Hendrina exceeding it by 200%.

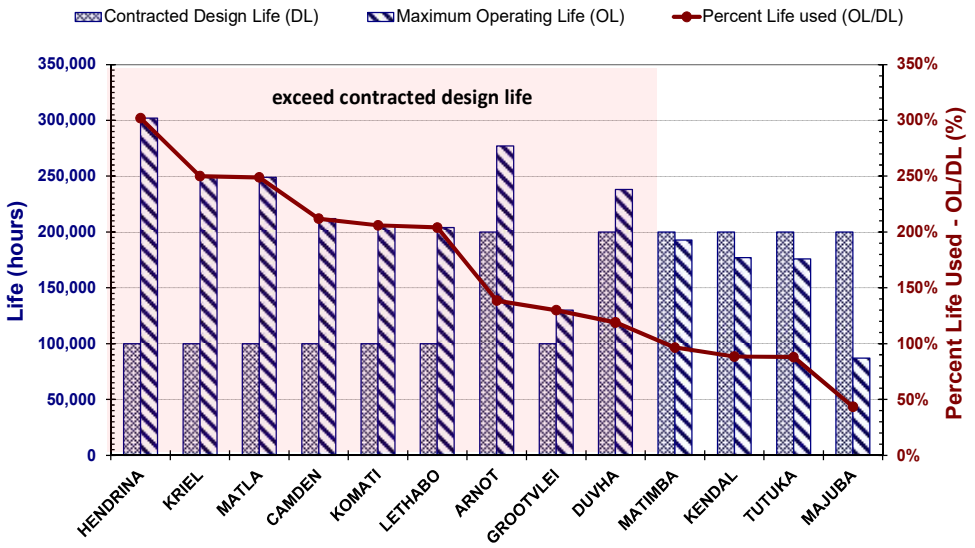

Figure 2.2-4 Life consumption of South African power plant (Molokwane 2014)

Now whether be it because of the more severe operating parameters; extending the operating life of older plants; or simply normal wear and tear, the integrity of the pipework will deteriorate (i.e. creep-strain in the case of this work) over time. This needs to be consistently assessed to mitigate the risk of failure, as safety of personnel and integrity of plant are of paramount importance. This is governed by plant maintenance processes in the business and the main concepts of creep damage assessment are looked at hereunder.

Firstly, a piping system in a power plant is only as strong as its weakest component, and a robust risk management strategy needs to focus resources on the said weakest points. Pipework in a power plant is welded together which has a detrimental side-effect on the creep strength of the system as a whole. Figure 2.2-5 shows the varied microstructure in a weldment as a function of temperature and distance from the centre of the weld. This is as a result of the heat input and subsequent cooling dynamics of the parent material and filler metal during the welding process. As was seen at the beginning of this section, microstructure has a direct correlation to the mechanical properties of steel. Therefore, the microstructure that is the mechanically weakest is the focal point of pipework integrity management.

Cracking within the weldment microstructure is classified based on the location in which it occurs, schematically shown in Figure 2.2-6 on the left. In their review on type IV cracking in ferritic power

plant steels, (Francis et al. 2006) concluded that the microstructure which is the weakest in creep is that associated with the Fine Grain Heat Affected Zone (FGHAZ) of the weld. (Mayr & Cerjak 2010) in their study on the impact of welding on creep properties of 9-12% Cr steels also concluded that for weldments of martensitic steels, Type IV cracking in the FGHAZ or ICHAZ (Inter-Critical Heat Affected Zone) is the life limiting factor. Figure 2.2-6 on the right shows an example of what Type IV cracking may look like. For this study it would therefore be prudent to focus on the HAZ of a weld as the weakest section of pipework, which poses the highest risk to integrity of the pipework as a whole.

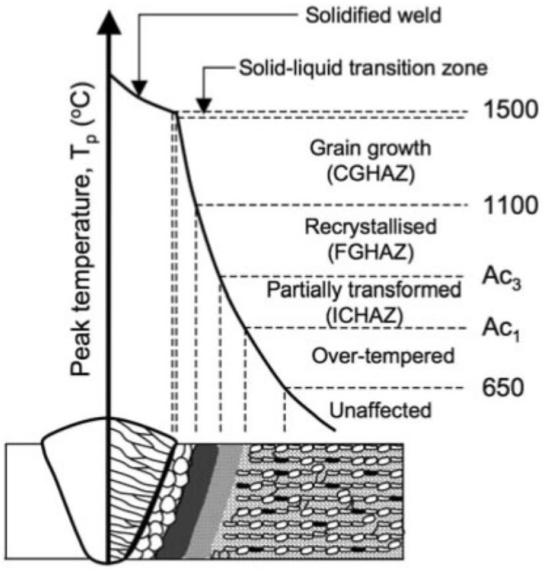

Figure 2.2-5 Schematic representation of microstructures developed in the HAZ as approximate functions of peak temperature during welding. (Francis et al. 2006)

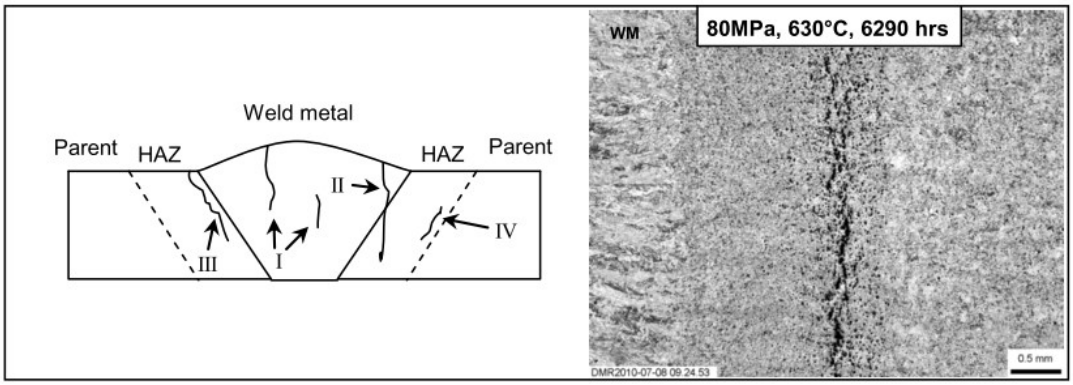

Figure 2.2-6 Left: Location of types of cracking, Right: Type IV crack in a 9Cr1MoVN steel (Rothwell & Mayr 2014)

For condition monitoring of creep strain, several techniques are available to the owner/operator of a power plant. Several of these are outlined by (Sposito et al. 2010) in their review of non-destructive techniques for the detection of creep damage in power plant steels, illustrated in Figure 2.2-7. It can be seen that the different techniques vary in their applicability during the creep life curve. This figure also eloquently shows the approximate evolution of the steels microstructure during the secondary and tertiary creep regimes.

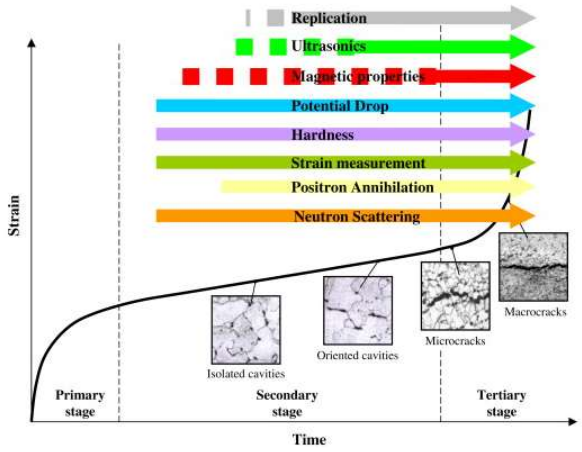

Figure 2.2-7 Typical creep curve with evolution of microstructural damage and various NDE techniques (Sposito et al. 2010)

Of these Non Destructive Examination (NDE) techniques, Metallographic Replication (replicas) is often used in Eskom power plants. (van Zyl et al. 2005) reports that nearly 60 000 replicas are taken, evaluated and archived each year, representing 15 000 locations and approximately 1 500 components, composed of materials from low alloy to 12% chromium steels. From circa 1980 to 2005, this accumulated to under one million archived replicas. The replica process works by grinding the surface area of pipework that needs to be inspected – commonly a weld. The surface is then polished to a mirror finish and etched with an etchant appropriate for the steel that is being tested. Acetate film is then wetted with a solvent to soften it and placed over the surface of interest. It is left there for a predetermined time to become imprinted with the negative of the surface's microstructure. Once removed, it is stored between glass slides and these are sent to a laboratory where they are individually analysed under a microscope. The analysis involves inspecting the microstructure qualitatively as well as counting voids per square mm, a parameter which is used in remnant life assessment models. These voids are the same ones described earlier in this chapter. This process is governed by standards, such as Eskom standard 240-75114345. As ubiquitous as the technique is, Metallographic Replication has some shortcomings:

- Storing/archiving and administering the large quantities of physical replicas can become cumbersome since records need to be kept for extended periods as baseline references, from which pipework integrity over time is trended.
- The data obtained from manually evaluating void density is subject to scatter due to the human factor.
- (Maharaj et al. 2009) state in their review of methods to estimate creep damage in low-alloy power station steam pipes that Metallographic Replication has limitations in detecting damage indicators manifesting under the pipe surface.
- (Yaguchi et al. 2010) also concluded in their study on creep strength of high chromium steel welded parts under multiaxial stress conditions, that during internal pressure conditions, the principal stress and multiaxiality were severe in the middle of the thickness at the HAZ region, which may be the cause of high voids distribution at that place. Surface replication would not be able to perceive this.

Measuring strain directly for creep quantification can be an advantageous alternative. Strain data can be directly correlated to a creep curve established for a material, as oppose to inferring the position on the creep curve from microstructural data. Strain is also less susceptible to the variance that is often present in creep curve data for a material, as is shown schematically by (Hulshof & Kraijesteijn 2011) in Figure 2.2-8 (Left). The said variance in creep curve data is exemplified by the P91 material at 600˚C (Figure 2.2-8 on the right) used by (Holdsworth et al. 2008) in their investigation on factors influencing creep model equation selection. The notion of using strain as the primary parameter to quantify creep is supported by (Hulshof et al. 2005), who state that by using criteria for strains, the strain measurements can be applied for life consumption of components. Additionally, strain is already used to monitor creep within Eskom power plants. This is done by way of high temperature capacitive strain gauges that are only used in special cases due to reasons including cost, difficulties in setup and susceptibility to vibration.

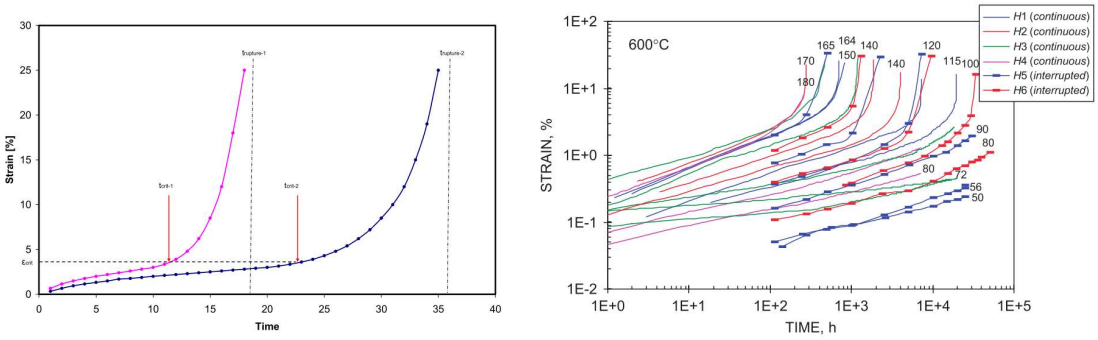

Figure 2.2-8 Left: "Scattering in time to rupture is sometimes very high while the scattering around a particular strain criteria value is still small." (Hulshof & Kraijesteijn 2011). *Right: Continuous and interrupted measurement creep curves for 6 casts of Steel-91 at 600°C* (Holdsworth et al. 2008)

An alternative and complementary method to measuring strain with the said capacitive strain gauges is by way of analysing sequential digital images of the surface in question. Application of this technology to measuring creep in power plants has been carried out under several organisations and projects:

- ARCMAC (Auto-Reference Creep Management and Control) is a technology developed by E.ON UK Power Technology and it monitors images for the movement of silicon nitride spheres placed on the surface of interest (Maharaj et al. 2009), (Morris et al. 2007), (Morris et al. 2006). Using the ARCMAC system over three experimental trials showed a mean error between 49 and 54 με (Narayanan et al. 2016).
- ARCMAC however only monitors strains between the few placed spheres. SPICA (Speckle Pattern Image Correlation Analysis) developed by KEMA takes the technology a step further by analysing a so-called speckle pattern that is applied to the surface in question. This advancement unlocks the capability to generate full field displacement and strain fields (Hulshof et al. 2005).
- CREEPIMAGE, is a project under the European Commission aiming to develop a long-term creep monitoring technique based on images. (Gao 2016) reported that it is possible to obtain an accuracy of 10 - 20 με under good conditions.
- (Van Rooyen 2016) used Digital Image Correlation to characterise thermal, mechanical and creep properties of X20 steel that is used in coal fired power stations.

Relative to Metallographic Replication, Digital Image Correlation obviates the need for physical storage and management of data (i.e. the large amount of replica slides across a fleet of stations). Digital Image Correlation also reduces the variability of the human factor, whereby the replicas need to be lifted and analysed manually, as the process is in large part software centric. The Data on Digital Image Correlation technology as applied to power plant pipework weld creep is limited and/or of proprietary knowledge. It is thus that this work takes a more detailed look into this technology, the concepts of which are expanded upon in the next several sections.

2.3 Digital Image Correlation

The technology underpinning the majority of these aforementioned projects is known as Digital Image Correlation (DIC). This is a process that quantifies deformation captured in sequential digital images by tracking the movement of a chosen subset within the image and generating a vector between its initial and final position (Figure 2.3-1). To facilitate this, markings on the surface collectively termed a speckle pattern is applied (section 2.6). The subset concept is extended to incorporate many of these subsets in an image, resulting in a field of vectors. This vector field can subsequently be mathematically manipulated to yield a strain field.

There are four high level components in a DIC system, namely: the camera technology used to capture the images of the surface being studied; the optics of the system focussing the image for the camera; the speckle patterns that are applied to the surface to facilitate the tracking of the deformation; and the correlation algorithm that is to be used to process the sequence of images. These will all be discussed in detail hereunder.

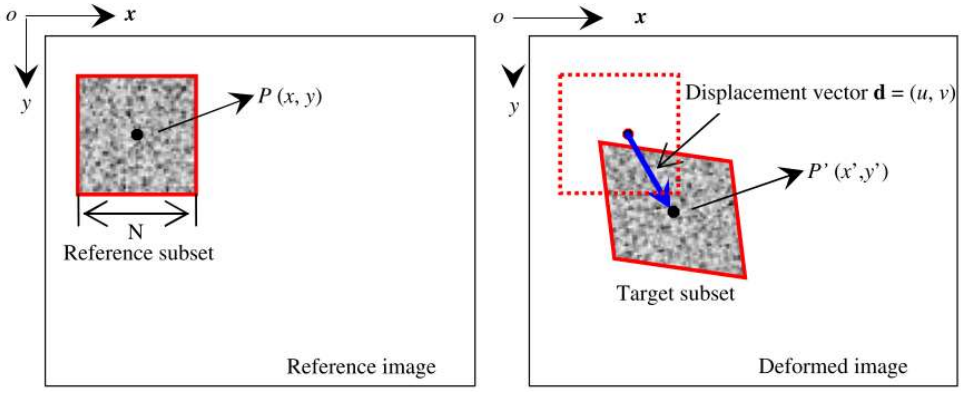

Figure 2.3-1 Vector generation from subset matching (Pan et al. 2010)

As was alluded to earlier, data on the performance of DIC for power plant applications, particularly in terms of strain accuracy and precision is scarce, as is information on the speckle patterns used. In order for Eskom to make a decision on possible implementation of DIC technology, it is prudent to investigate its performance to ascertain whether the technology is suitable for Eskom's use, as well as to have a basis upon which to validate claims made by potential service providers of the technology.

2.4 Pixels and Image Sensors

The first step in using DIC to measure the strain in power plant pipework is to capture a digitised image of the surface. This function is carried out by an image sensor, which will be delved into in this section.

The most fundamental component of an image sensor is a pixel. This is a light sensitive electrical component (a photodiode) that converts incoming photons into electrons and ultimately into a digital signal. These are clustered together into a 2D array known as an image sensor. The efficiency with which a pixel can convert photons to electrons is known as the Quantum Efficiency - defined as the ratio of the generated electrons to the number of incident photons. Light of differing wavelength will release electrons from the photodiode's atom's various orbitals, requiring differing quanta of energy and hence the quantum efficiency is wavelength dependant. Pixels are generally constructed in one of two competing technologies, Complementary Metal Oxide Semiconductor (CMOS) and Charge-Couple Devices (CCD). CMOS technology has circuitry for processing the electrons into the said digital signal next to the photodiode itself, which make them more prone to electrical noise than Charge-Couple Devices. This circuitry also takes up pixel surface area that could be used by the photodiode for capturing more potential incoming photons, and so hampers its performance relative to a CCD. CCD technology makes use of so-called bins next to the photodiode to store the electrons, which also take up pixel real estate but relatively less than that of CMOS pixels. The processing of the electrons into the digital signal is subsequently done in circuitry that is external to the pixel and used by all of them on the image sensor. The trade-offs between the two technologies for the application in pipework strain measurement are weighed up in section 3.1.

Regardless of the intervening circuitry, the charge of electrons is read out as an analogue voltage signal which is then amplified. The extent of amplification is known as the ISO. Amplification of a weak signal (few incident photons) relative to the noise floor will produce a noisy signal. This is ultimately manifested in the digital image being perceived as "grainy". A large signal-to-noise ratio is thus desirable, which can be achieved by maximising the pixel's ability to capture a large number of photons. This is directly linked to the pixel surface area - hence a CCDs superior low light performance. A signal is ideally maximised by increasing the incident light onto the pixel/image sensor, which will be dealt with in the section 2.5. For pipework strain measurements, the combination of surface lighting and signal amplification must be adequate to ensure high signal-to-noise data for the DIC correlation algorithms to work with.

Once the voltage signal has been amplified, it is digitised by an analogue to digital converter (ADC). The number of graduations into which the analogue voltage signal is divided to yield a digitised signal is termed the bit depth. The greater the bit depth, the more shades of a colour that can be discerned. A larger bit depth will however generate a larger digital file since more digital bits are needed to store the data for each pixel. A pixel with no photons incident upon it will theoretically read a value of zero and once it has reached its so called well capacity – maximum number of electrons it can contain - will register a value equal to the maximum number that the bit depth dictates. Upon converting additional photons to electrons, the pixel is said to be saturated and this additional data cannot be registered. Such a pixel may also 'bleed' electrons into the next pixel, negatively affecting the data signal from that pixel.

A large pixel will result in a good so-called dynamic range, which is the ability to capture very bright as well as very dim light. The length of time that the sensor is exposed to light will also naturally affect the quantity of photos that are incident onto the image sensor, termed the exposure time. The degree to which the pixels in an image sensor are filled is commonly represented by an intensity histogram as is illustrated in Figure 2.4-1. Here the possible intensity range of a pixel is indicated on the horizontal axis. The range of this scale is dependent on the bit depth, and seen to be 12bit =

4096 possible graduations, including zero, in this particular figure. Lower numbers represent fewer incident photons (darker) and vice versa.

The vertical axis is a count of how many of the pixels within the image sensor are at a particular intensity. In Figure 2.4-1, the left-hand side histogram is seen to have proportionally more pixels being darker for the particular image captured and the right histogram shows the opposite. By varying the ISO and exposure on the imaging system and the illumination of a scene, the intensity distribution of the image is altered. The shape of the distribution is representative of the scene that is imaged, and of import is to adjust the aforementioned parameters such that significant amounts of pixels do not lie at either extreme of the intensity range. Pixels at the extremities are hampered from providing additional information and artefacts such as the aforementioned electron-bleeding between pixels may occur. The bit depth (in conjunction with the number of pixels available on the sensor) will determine the density of information available to the DIC correlation algorithm discussed in section 2.7.

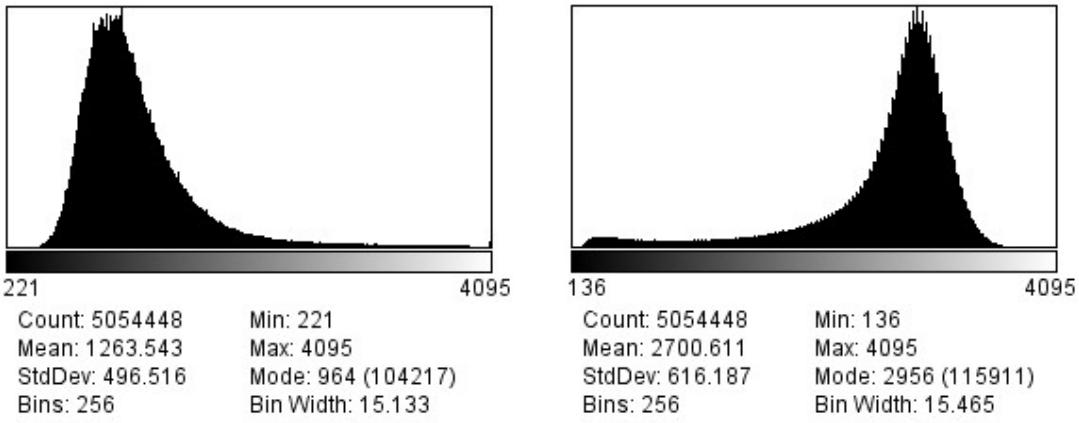

Figure 2.4-1 Intensity histogram with Left: greater proportion of the pixel in the image being darker; Right: greater proportion of the pixels being brighter.

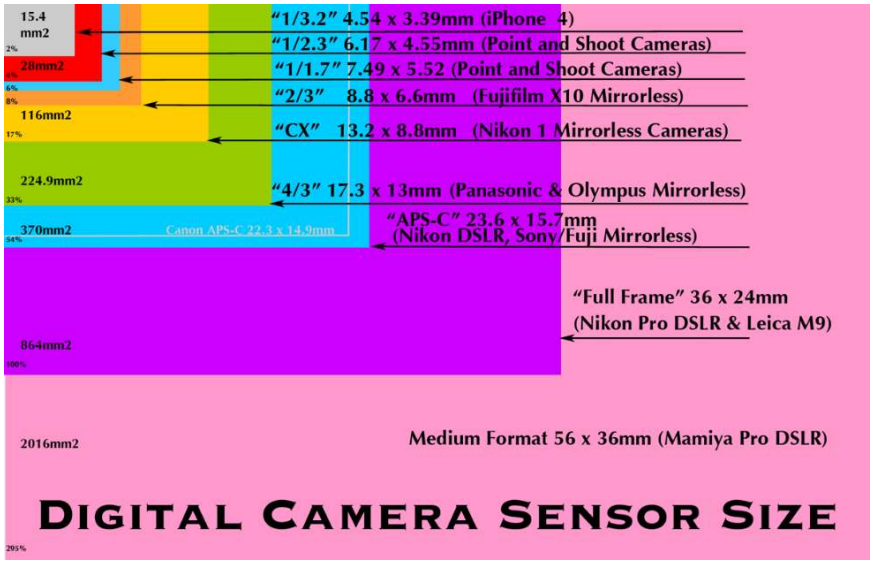

Figure 2.4-2 Physical sizes of standard digital image sensors (Anon n.d.)

Digitisation of the light intensity as described above will yield a greyscale image. A colour image sensor differs from the greyscale sensor by incorporating a colour filter over the pixels (e.g. Bayer filer) so as to produce intensity signals for the three primary colours (Red, Green, and Blue). This ultimately generates three intensity images, one for each primary colour. The tracking of features that is done by the DIC correlation algorithms is primarily concerned with the intensity of pixels. Colour information is therefore superfluous and hence colour sensors will not be used in this work and thus, additionally, the effects of spatial interpolation of Bayer images was not considered.

Image sensors are constructed into standardised sizes, as can be seen in Figure 2.4-2. For a given standard sensor size, an increase in the number of pixels (termed resolution) will inevitably result in pixels with smaller surface areas. This result is a trade-off between low light performance and spatial/optical resolution. Optical resolution will be looked at next.

This section delved into the theory of image sensors, that will be used to capture the images of the pipework surface for DIC processing. It was seen that several parameters need to be taken into account to ensure images of adequate quality are captured. These parameters included amount of lighting, ISO, exposure time, bit depth, and sensor resolution.

2.5 Optics

Optics in an imaging system control the incidence of light onto an image sensor, which is practically achieved by way of lenses. This section looks at the practicalities of manipulating the optics that will affect the image quality of the pipework surface.

A camera lens produces an image circle within which the image sensor will lie. The fringes of the image circle may be vulnerable to optic artefacts and hence the image sensor lies well within the image circle in practical applications to avoid this. There exist several other optical distortions and aberrations as a result of the limiting practicalities of focussing incoming light with manufactured glass lenses. The reflection and refraction of light through the said glass diverges from approximating theoretical models and engineers correct for these divergences with refined designs and materials, improved manufacturing techniques and software calibration.

The area within an entire scene that an image sensor will capture is termed the Field of View (FOV) and will be dictated by the size of the image sensor and the so-called focal length of the lens. The focal length is defined as the distance between the lens centre and the image sensor. In practical terms, the larger the focal length is, the smaller the FOV will be for a given sensor size. This is commonly known as the degree of ‘zoom’. Figure 2.5-1 shows the aforementioned relationship for a sensor size of 35mm.

It is observed that as the focal length increases, the building is seen to be more zoomed in, but less of it is visible. Lenses are manufactured with choices of adjustable or fixed focal lengths, the latter being termed prime lenses. This optical zooming functionality allows DIC to be scale independent, meaning that it can track deformations ranging from movement of avalanches on the macro scale down to deformations in crystallographic grains at the microscopic scale. For the sake of this work, the focal length is to be chosen such that the FOV will encompass the weld HAZ, which was seen to be the weakest (and hence of most interest) part of a weldment in section 2.2.

In Figure 2.5-1, graphical perspective is evident in the narrowing of the imaged building's pathway from the 14mm to 35mm focal length, i.e. the path is seen to be narrower further from the camera. The human brain interprets this distortion to perceive the distance between objects. This phenomenon is however problematic in applications where calculations need to be made from feature dimensions and positions within the image, as is the case with DIC. The distorted size relationship of objects at different distances from the lens leads to a DIC system perceiving feature sizes incorrectly, especially so when they move outside of their initial plane (parallel to the image sensor).

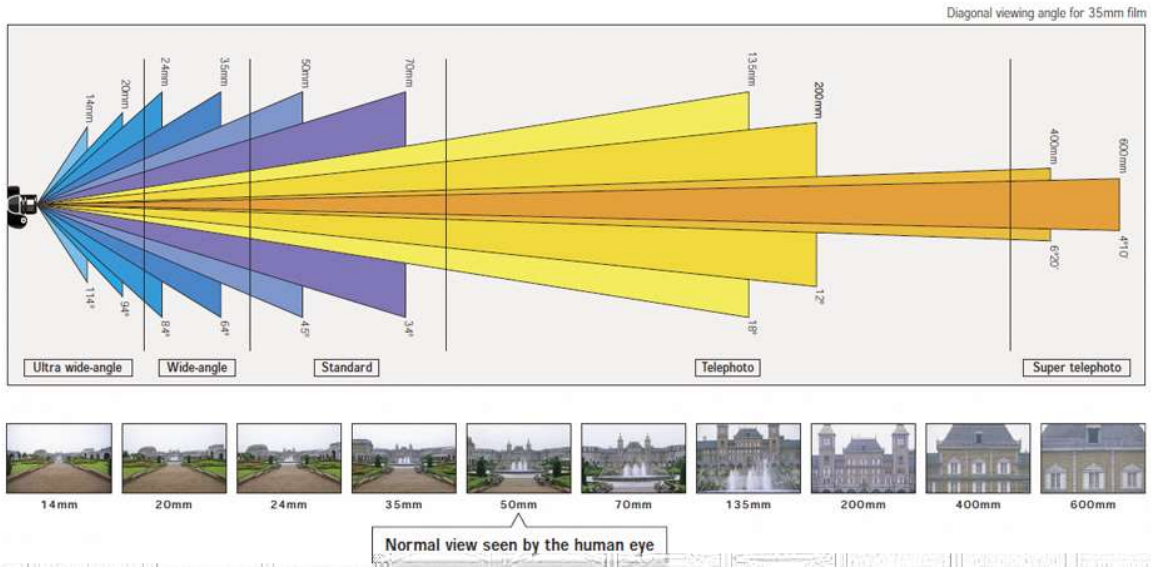

Figure 2.5-1 Effects of focal length on FOV (Anon n.d.)

A special variety of lens used to cancel out the perspective error is the telecentric lens. These lenses have a constant FOV (equal to the diameter of the lens itself) regardless of the object distance from the lens. This results in the loss of depth perception and objects of the same physical dimensions are perceived as such in the image regardless of distance from the lens, as is demonstrated in Figure 2.5-2. Disadvantages of telecentric lenses include physical size and weight, cost, fixed magnification and limited depth of field (covered next) (Sutton et al. 2008). Unless a feature's change in distance from its initial plane is accounted for (such as by using more than one camera), perspective in pipework images needs to be mitigated as far as possible to minimise artificial measurements.

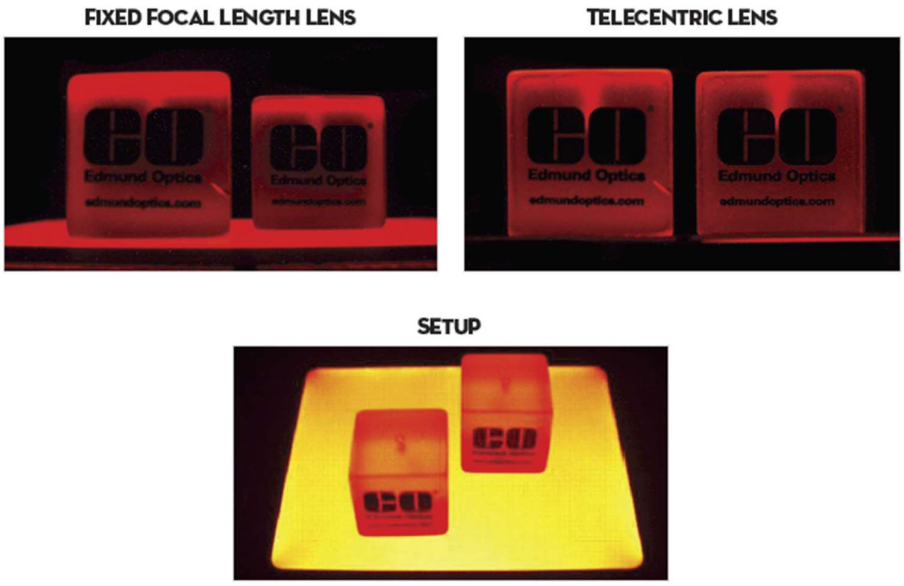

Figure 2.5-2 Concept of Parallax Error (Edmund Optics n.d.)

The aperture is the diameter of the opening that regulates light into the camera. The ratio of focal length to aperture diameter is known as the F-stop number and is used in practice to regulate what is termed the depth of field. The depth of field is the range in front and behind the plane of optimal focus in which an image remains acceptably in focus, as is schematically demonstrated in Figure 2.5-3. Within the context of imaging powerplant pipework, it is to be ensured that the surface is well within the imaging system's depth of field to ensure feature are well defined. In particular, the curvature of the pipe within the FOV needs to fall within the depth of field.

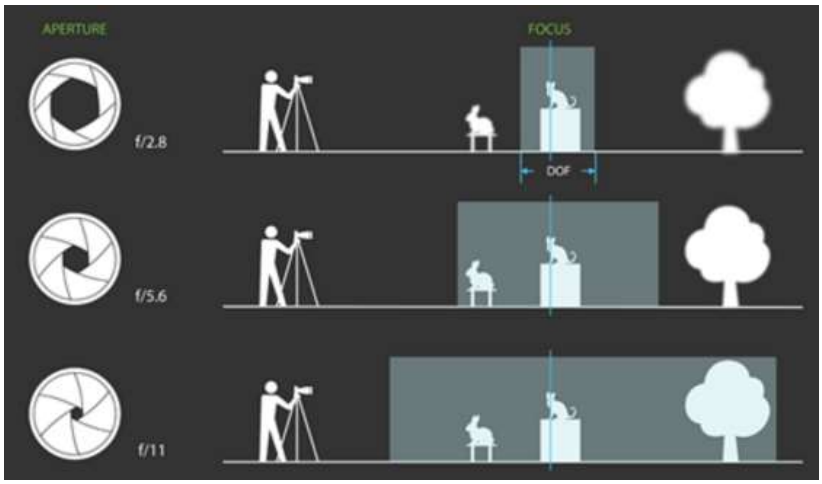

Figure 2.5-3 Concept of depth of field (Xu n.d.)

Optical resolution determines the minimum size of object that can be discerned by an imaging system. At a given focal length, the sensor pixel resolution will determine the optical resolution that will be resolvable. This can be understood with reference to the optical test chart seen in Figure 2.5-4.

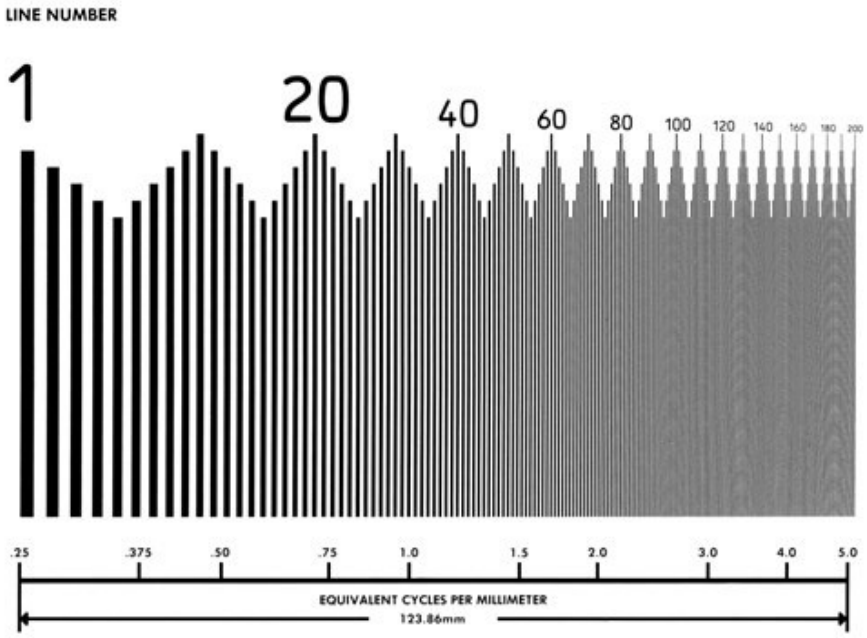

Figure 2.5-4 R72 Sayce Logarithmic Test Chart for optical resolution (Anon n.d.)

Here the black bars and spaces between them reduce in thickness logarithmically from left to right, starting the numbering at bar 1 and ending at 200 in this particular chart. A set of pixels that are the optimal size to resolve bar 1 and 2 without significant oversampling will be too large to adequately resolve bar 199 and 200. This will have a bearing on the number of pixels that are used to resolve features in the so-called speckle pattern, which will be looked at next. As was detailed in section 2.4, the trade-off of smaller pixels for greater optical resolution will be a loss in light sensitive surface area for each pixel, and hence image sensor low-light performance is compromised.

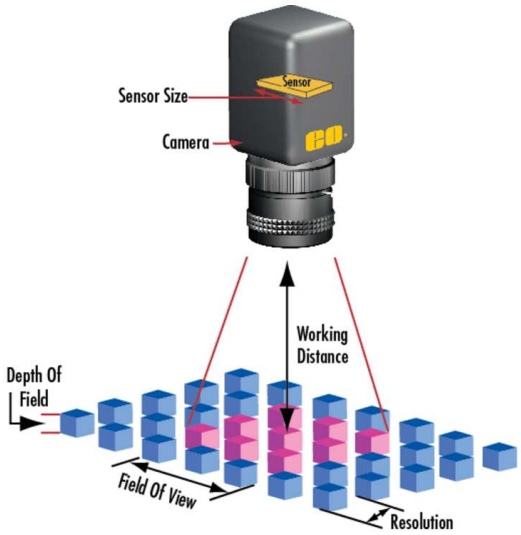

Figure 2.5-5 Fundamental parameters of an Imaging System (Edmund Optics n.d.)

In this section, parameters related to the optical setup of the imagining system were looked at. Several of the parameters detailed in this section are well summarised by Edmund Optics in Figure

2.5-5. The parameters looked at included FOV, Focal Length, Aperture, Depth of Field and optical resolution. The selection of these parameters for this work must be optimised so as to yield a quality image of the pipework surface within an area representative of the weld HAZ.

2.6 Speckle pattern

As has been mentioned, DIC tracks features in a sequence of captured images. For materials testing, the features are generally in the form of speckles applied to the surface of the material being imaged, termed a speckle pattern. It is assumed that the speckle pattern deforms with the substrate to which it is applied, which is reasonable until spalling of the applied speckle pattern occurs at extreme deformations and strains.

2.6.1 Speckle pattern application

There are several methods with which a speckle pattern can be applied. In their work on optimising the preparation of speckle patterns, (Lionello & Cristofolini 2014) reviewed literature to summarise several methods for producing them (Figure 2.6-1). This table also attests to the scale independence of DIC technology that was mentioned previously, with feature sizes ranging in orders of magnitude from nanometres to micrometres in this case. This list is however not exhaustive, overlooking common techniques like spray-can speckle patterns.

The choice of speckle pattern has an influence on the resulting outputs of DIC processing as can be attested to by (Crammond et al. 2013) in Figure 2.6-2, where discrepancies were noted between strain results from airbrush and spray-can speckle patterns relative to strain gauge references. (Haddadi & Belhabib 2008) proposed tests that explored the errors related to the different sources including speckle pattern quality and concluded that it is very important because of its influence on the image correlation (section 2.7) in the DIC process.

Methods	Typical speckle size	Typical specimen dimensions and application	Limitations
Nano platinum dots and focused electron beam (FEB) deposition	>15 nanometres	5.43 × 4.66 μm field emission gun scanning electron microscope – focused ion beam (FEGSEM/FIB)	DIC accuracy depends on magnification. FEBs generate surface heat, which may lead to micro-structural changes due to phase transformation.
Chemical deposition of yttria-stabilised zirconium particles	20–30 nanometres	FEGSEM/FIB microscope	DIC accuracy depends on magnification
Nano platinum dots and focused ion beam (FIB) deposition	>30 nanometres	23.3 × 20 μm FEGSEM/FIB microscope	DIC accuracy depends on magnification. FIB-assisted deposition induces surface damage.
Solution deposition of fluorescent silica nanoparticles	140–180 nanometres	170 × 140 μm fluorescent microscope	
Compounding of epoxy resin and graphite powder particle	3 micrometres	Optical microscope	Difficult to eliminate agglomeration during the preparation of the pattern
Paint with fine point airbrush (0.18 mm nozzle)	10–30 micrometres	6.4 × 4.8 mm stereomicro-scope	
Calibrated polyamide particles	150 microme-tres	6 × 10 mm CCD camera	Agglomeration; underestimation for strain values over 10% due to rigidity of particles
Computer generated random pattern screen printed on the surface of the specimens	Not indicated	80 × 12.5 mm CCD camera	Only flat surfaces can be coated

Figure 2.6-1 Overview of the possible methods for producing speckle patterns of different sizes (Lionello & Cristofolini 2014)

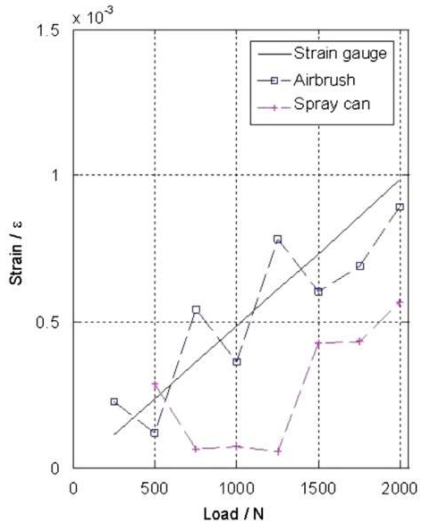

Figure 2.6-2 Discrepancies between strain results of different speckle patterns (Crammond et al. 2013)

The lens, image sensor and other hardware selection will also have an influence on the speckle pattern's perceived feature size, sampling density and quality as has been detailed in the previous section.

2.6.2 Qualitative speckle pattern traits

There are a few speckle pattern fundamentals that are difficult to quantify but are generally agreed upon in literature to be constituents of a good speckle pattern. In their book, (Sutton et al. 2009)

suggest that an ideal surface texture should be isotropic (not having a preferential direction) and they showed that periodic patterns may lead to feature registration problems. (Lionello & Cristofolini 2014) concur that the pattern should be isotropic, adding that it should also be stochastic and highly contrasted. (Crammond et al. 2013) agree that the pattern needs to be stochastic, having high levels of unique features and randomness to maximise the correlation function response in each subset (section 2.7).

2.6.3 Feature size

(Lionello & Cristofolini 2014) suggest that the speckle pattern should have an average size that exceeds the image pixel size by a factor of 3–5, claiming that smaller speckles cause poor contrast, and larger speckles cause poor spatial resolution. In their book on image correlation, (Sutton et al. 2009) recommend a feature size range of 3 to 6 pixels so as to facilitate a reasonable amount of over-sampling and accurate reconstruction with suitable interpolation filters. This is shown qualitatively by them in Figure 2.6-3 for optimal samping, over-sampling, and under-sampling respectively.

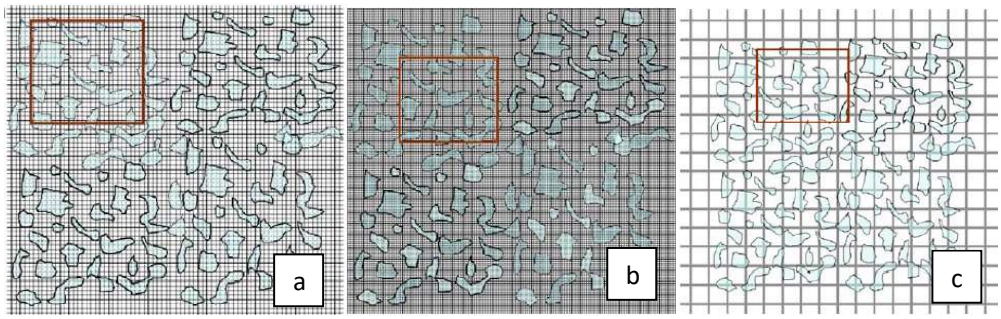

Figure 2.6-3 Approximate pixel density per feature for (a) optimal sampling; (b) over-sampling; (c) under-sampling (Sutton et al. 2009)

As was alluded to in section 2.5, the number of pixels per feature is a function of both the speckle pattern used and the imaging system hardware selected. This is in agreement with (Reynolds & Duvall 1999), who state that the size of the speckle pattern feature depends on the spatial resolution required and therefore the magnification used to view the pattern.

There obviously also exists inherent variability in a speckle pattern that is by design stochastic. The characteristic feature size profile for an airbrush and spray-can speckle pattern was generated by (Rajan et al. 2012) as can be observed in Figure 2.6-4. It is seen that both are statistically skewed in a similar manner but have characteristic profiles of their own nonetheless. (Rajan et al. 2012) report that the long tails entail that there will be a few features within the speckle pattern several times larger than that of the median. This observation implies that some subsets will be inadequately sized to deal with these features, which affect correlation (as will be discussed in section 2.7), however these are proportionally few.

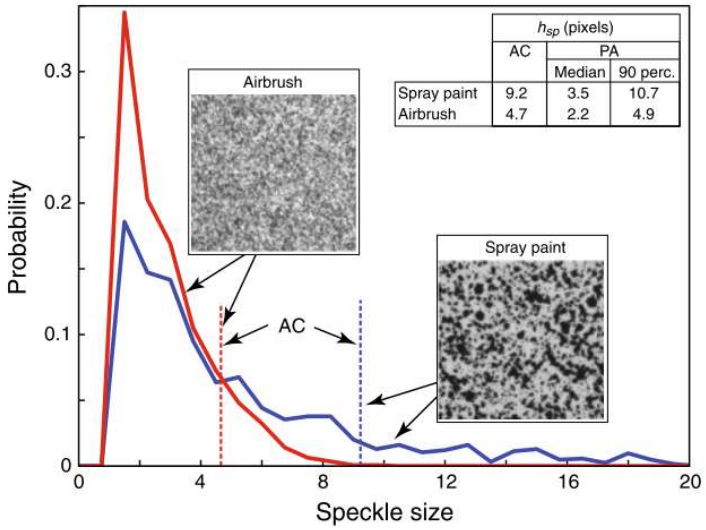

Figure 2.6-4 Speckle size distribution (Rajan et al. 2012)*. The methods used were particle analysis (PA, solid lines) which was done with ImageJ, and autocorrelation (AC, dashed lines) which is a more involved algorithmic sizing scheme used by* (Rubin 2004) *and others.*

2.6.4 Intensity gradient

Related to the intensity distribution is the intensity gradient, which is the first-order derivative of the pixel intensities within a defined neighbourhood. In general image processing, intensity gradients are used as a building block for processes such as edge detection. In DIC, intensity gradients are important since they are used as part of the DIC optimisation algorithm (gradient based). It is also used in several other aspects of DIC, two instances are: for the quality control of the speckle patterns; and for algorithms designed to make DIC parameter choices easier. Cases in point of each are detailed below.

(Pan 2011) concluded in their study on a novel global parameter used to assess the quality of the entire speckle pattern, that mean bias error and standard deviation of the measured displacement are closely related to their novel parameter. Their so-called *mean intensity gradient* (MIG) parameter is a function of the image first-order intensity derivatives as can be seen below.

$$\delta_f = \sum_{i=1}^{W}\sum_{j=1}^{H}\left|\nabla f(\boldsymbol{X}_{ij})\right| / (W \times H)$$

Where W and H are the image width and height of the image respectively (in units of pixels), $\left|\nabla f(\boldsymbol{X}_{ij})\right| = \sqrt{f_x(\boldsymbol{X}_{ij})^2 + f_y(\boldsymbol{X}_{ij})^2}$ is the modulus of the local intensity gradient vector, $f_x(\boldsymbol{X}_{ij})$ and $f_y(\boldsymbol{X}_{ij})$ are the first-order intensity derivatives at pixel $\boldsymbol{X}_{ij}$. (Yu et al. 2014) in their work on evaluating speckle patterns, took the aforementioned work on MIG and used second-order derivatives to define an additional parameter that they termed the *Mean Intensity of the Second Derivative* (MIOSD).

(Pan et al. 2008) developed an algorithm to recommend a subset size for theoretically optimal displacement accuracy for a given speckle pattern. The subset size (dealt with later) is crucial to the accuracy of DIC. The said algorithm is based on the Sum of Square Subset Intensity Gradients (SSSIG),

which is a parameter defined by the authors. The mathematical derivation is beyond the scope of this work, but as the name suggests, first-order derivatives of the greyscale intensities are once again used.

It is thus highlighted that intensity gradients are an elemental building block of DIC and are therefore seen as a vital parameter to take into account for the characterisation of speckle patterns. A change in this parameter has ramifications for several DIC aspects, some of which were illustrated above.

2.7 Image correlation

The next concept that will be looked at is the implementation of image matching within DIC and how displacements and strain are subsequently derived.

2.7.1 Correlation algorithm

In DIC, image correlation is the process of matching features in two subsequent images. The image to which features are referenced is termed the reference image and the subsequent images are the target images. The correlation process is done by subdividing the reference image into groups of pixels termed subsets; and mapping the positions of those subsets to their positions in the target image. The displacement of the centre of a given subset relative to the centre of that particular subset's position in the target image yields a displacement vector – recall Figure 2.3-1

By tracking groups of pixels (using subsets), subpixel accuracy can be achieved. Using a uniaxial tensile specimen with a subset size of 19 × 19 pixels, (Lava et al. 2009) showed the achievable sub-pixel displacements when an applied strain of up to two pixels was applied (Figure 2.7-1). Their work made use of their own correlation software platform which they called MatchID, as well as commercial software in the form of Vic2D for validation.

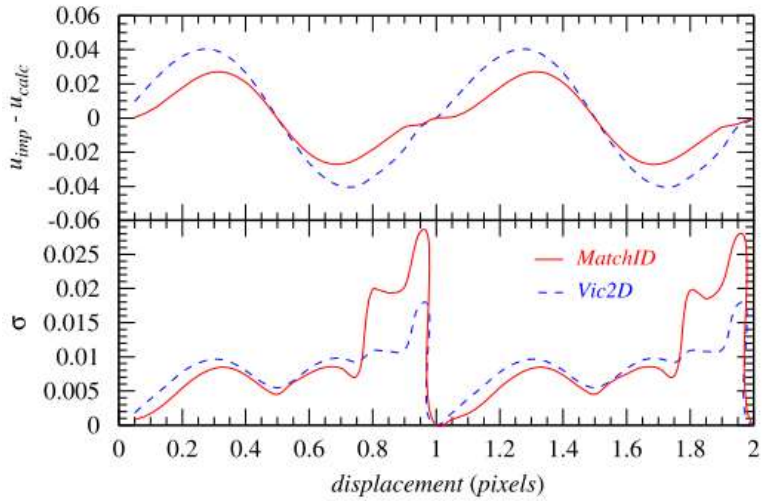

Figure 2.7-1 Top panel: Difference between the imposed and DIC calculated deformations. Bottom panel: Standard deviations of the displacement measurements. Vertical axis units are in pixels. (Lava et al. 2009)

In other work on assessing three algorithms popularly used for sub-pixel displacement registration, (Bing et al. 2006) also measured this error parameter (Figure 2.7-2). This was performed by using computer-generated speckle images to be able to numerically control the deformation, and it was repeated for two subset sizes, namely 31 × 31 pixel and 61 × 61 pixel. The applied deformations

were 50 % of that applied by (Lava et al. 2009) but it is be noted that in both cases, deformations measurements well below the size of a pixel are readily possible with DIC technology.

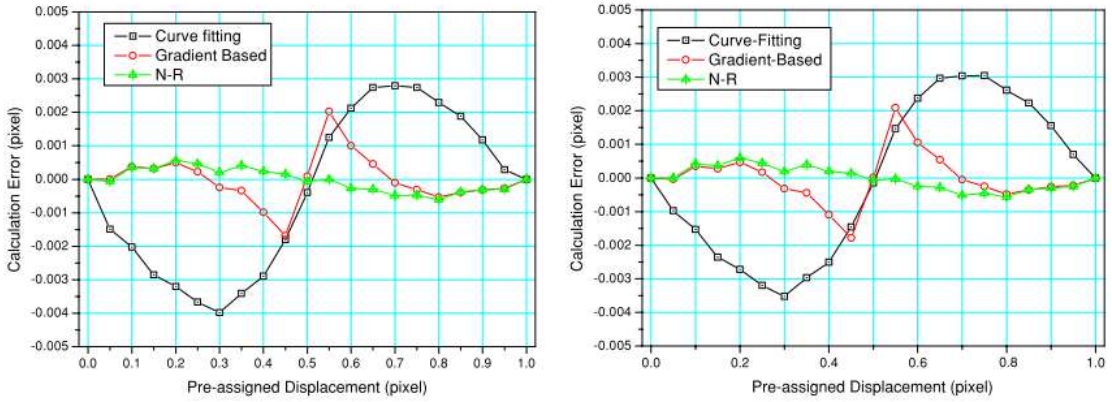

Figure 2.7-2 Errors in DIC deformation measurements as a function of an imposed deformation up to 1 pixel. Left: 31 × 31 pixel Right: 61 × 61 pixel. (Bing et al. 2006)

Using several of the aforementioned subsets will generate a vector displacement field that is representative of the deformation of the speckle pattern, and hence the substrate onto which it is applied. As was seen above, the said displacement vectors are expressed in units of pixels. This can be converted into conventional units of length by way of an image calibration. One method recommended by (Sutton et al. 2009) is the use of a planar calibration target. This involves taking an image of the said target, whose dimensions are accurately known, and which is temporarily placed where the speckle-patterned specimen will ultimately be positioned. An algorithm is then used to map the pixel dimensions of the image and the real-world dimensions of the target plate. Since strain is defined as the dimensionless ratio of the original length of a specimen divided by its change in length, any unit of length will suffice as long as it is consistent. That is, for strain measurements, it is not necessary to convert from pixel units of length.

The process of determining the displacement of the target subset is one of iteratively guessing its position in the target image and evaluating its similarity to that of the subset in the reference image. The position that is found to be the most similar out of all the iterations is then used to calculate the aforementioned displacement vector.

The similarity between reference and target subsets is quantified by comparing pixel intensity values in the subsets. Two methods commonly used are Cross Correlation (CC) and Sum of Squared Differences (SSD). There are several derivatives of the two methods and (Pan et al. 2009) in their review of 2D DIC for strain measurements have summarised the most common of these derivatives, which are shown in Table 2.7-1. These are organised in rank of increasing complexity. $f(x_i, y_j)$ is the intensity of a pixel at position x_i, y_j in the reference subset, and $g(x_i', y_j')$ is the intensity of a pixel at position x_i', y_j' in the target subset.

The remaining terms are defined as follows:

$$\bar{f} = \sqrt{\sum_{i=-M}^{M} \sum_{j=-M}^{M} \left[f(x_i, y_j)\right]^2} \qquad \bar{g} = \sqrt{\sum_{i=-M}^{M} \sum_{j=-M}^{M} \left[g(x_i', y_j')\right]^2}$$

$$\Delta f = \sqrt{\sum_{i=-M}^{M}\sum_{j=-M}^{M}\left[f(x_i,y_j) - f_m\right]^2} \qquad \Delta g = \sqrt{\sum_{i=-M}^{M}\sum_{j=-M}^{M}\left[g(x_i',y_j') - g_m\right]^2}$$

$$f_m = \frac{1}{(2M+1)^2}\sum_{i=-M}^{M}\sum_{J=-M}^{M} f(x_i,y_j) \qquad g_m = \frac{1}{(2M+1)^2}\sum_{i=-M}^{M}\sum_{J=-M}^{M} g(x_i',y_j')$$

	Cross-Correlation	**Sum of Squared Differences**
Standard	$C_{CC} = \sum_{i=-M}^{M}\sum_{j=-M}^{M}\left[f(x_i,y_j)g(x_i',y_j')\right]$	$C_{SSD} = \sum_{i=-M}^{M}\sum_{j=-M}^{M}\left[f(x_i,y_j) - g(x_i',y_j')\right]^2$
Normalised	$C_{NCC} = \sum_{i=-M}^{M}\sum_{j=-M}^{M}\left[\frac{f(x_i,y_j)g(x_i',y_j')}{\overline{f}\,\overline{g}}\right]$	$C_{NSSD} = \sum_{i=-M}^{M}\sum_{j=-M}^{M}\left[\frac{f(x_i,y_j)}{\overline{f}} - \frac{g(x_i',y_j')}{\overline{g}}\right]^2$
Zero-Normalised	$C_{ZNCC} = \sum_{i=-M}^{M}\sum_{j=-M}^{M}\left\{\frac{\left[f(x_i,y_j) - f_m\right]\times\left[g(x_i',y_j') - g_m\right]}{\Delta f \Delta g}\right\}$	$C_{ZNSSD} = \sum_{i=-M}^{M}\sum_{j=-M}^{M}\left[\frac{f(x_i,y_j) - f_m}{\Delta f} - \frac{g(x_i',y_j') - g_m}{\Delta g}\right]^2$

Table 2.7-1 Derivatives of Cross-Correlation and Sum of Squared Differences algorithms, modified from (Pan et al. 2009)

(Pan et al. 2009) recommend Zero-Normalised CC or Zero-Normalised SSD correlation criteria because of their insensitivity to offset and linear change in illumination lighting, which essentially adds robustness to DIC in terms of the acceptable variability in the applied lighting on the speckle pattern being investigated. It is noted that the CC algorithms are related to the SSD algorithms and one can be derived from the other.

Now the iterative displacement mapping of co-ordinates x_i, y_j in the reference subset to x_i', y_j' in the target subset is accomplished by way of a so-called shape function. The complexity of the shape function used depends on the deformations expected between the reference and target subsets. A zero order shape functions will only take translation of the subset into account. First order functions account for constant shear and normal strains, and progressively higher order functions model more complex subset deformations. It is desirable to model the deformation (and hence mapping) of the subsets accurately to maximise the correlation algorithms ability to match the said subsets. This notion is supported by (Schreier & Sutton n.d.), who conclude that higher order shape functions are desirable to minimise the difference between the shape function and the actual displacement field encoded in the images.

The digitisation of the speckle pattern into discrete data points by the image sensor can be limiting on the capabilities of DIC algorithms. A shape function may need to map inter-pixel locations, by using interpolated data between discrete points, in order for the correlation algorithm to calculate sub-pixel deformations as was detailed earlier. The interpolation schemes applied follow the same principles as one-dimensional interpolation and are simply extended to encompass data from the pixels around the point of interest, resulting in two-dimensional interpolation. As such, traditional

linear interpolation becomes bilinear interpolation. (Bruck et al. 1989) found that more sophisticated interpolation algorithms such as bicubic interpolation yielded higher accuracy. This was also found by (Chu et al. 1985). In more recent work on accuracy enhancement of DIC, (Luu et al. 2011) found that B-spline interpolation functions were superior to the bicubic algorithms.

The relationship between reference and target images can be defined in several ways, the two most common being relative-to-first and relative-to-prior. The former uses the first image of the set as the reference for all subsequent target images. This method has the advantage of precluding the incremental accumulation of errors at each image step. It however suffers from deterioration in correlation with large deformations, where the correlation algorithm increasingly struggles to match the deformed subsets to their references. The latter method uses the image directly preceding the target image in question as the reference image. In this method, there is an accumulation of error but the correlation throughout the image set will remain high relative to the prior method, as deformations between consecutive images will be smaller than that relative to the first image. The former method was used in this work.

2.7.2 Subset size

In their work on quality assessment of speckle patterns (Lecompte et al. 2006) concluded that the size of the speckle pattern features in combination with the size of the subset have an influence on the accuracy of the measured homogeneous displacements. They also concluded that it is important that the subset size is chosen in accordance with the expected deformation, as too large a subset will smooth real material behaviour in areas where there are steep deformation/strain gradients. (Pan et al. 2008) and (Pan et al. 2010) agree that subset size is critical to the accuracy of the measured displacements.

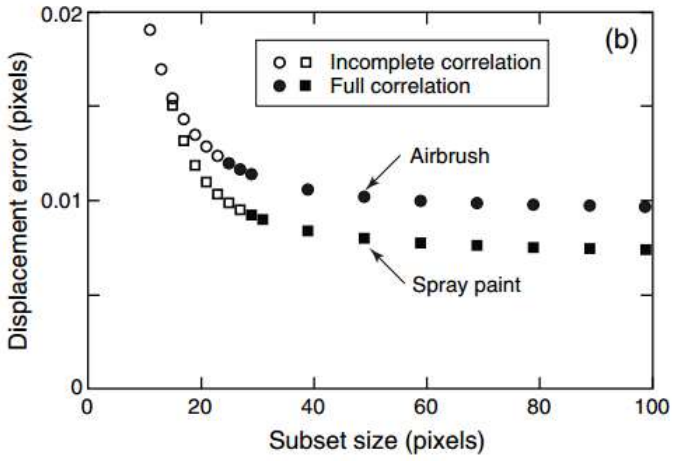

Figure 2.7-3 Effects of subset size on displacement error for differing speckle pattern techniques (Rajan et al. 2012)

In their work on optimising DIC for high resolution strain mapping of ceramic composites, (Rajan et al. 2012) found that increasing the subset size decreased the displacement error. This trend was consistent for two different speckle pattern application techniques as can be seen in Figure 2.7-3. (Pan et al. 2008) in their study on subset size selection in DIC for speckle patterns, did a similar exercise using three different speckle patterns. Their findings agree with that of (Rajan et al. 2012),

showing that the standard deviation of the DIC calculated displacement decreases with an increase in subset size for all three speckle patterns, as can be observed in Figure 2.7-4

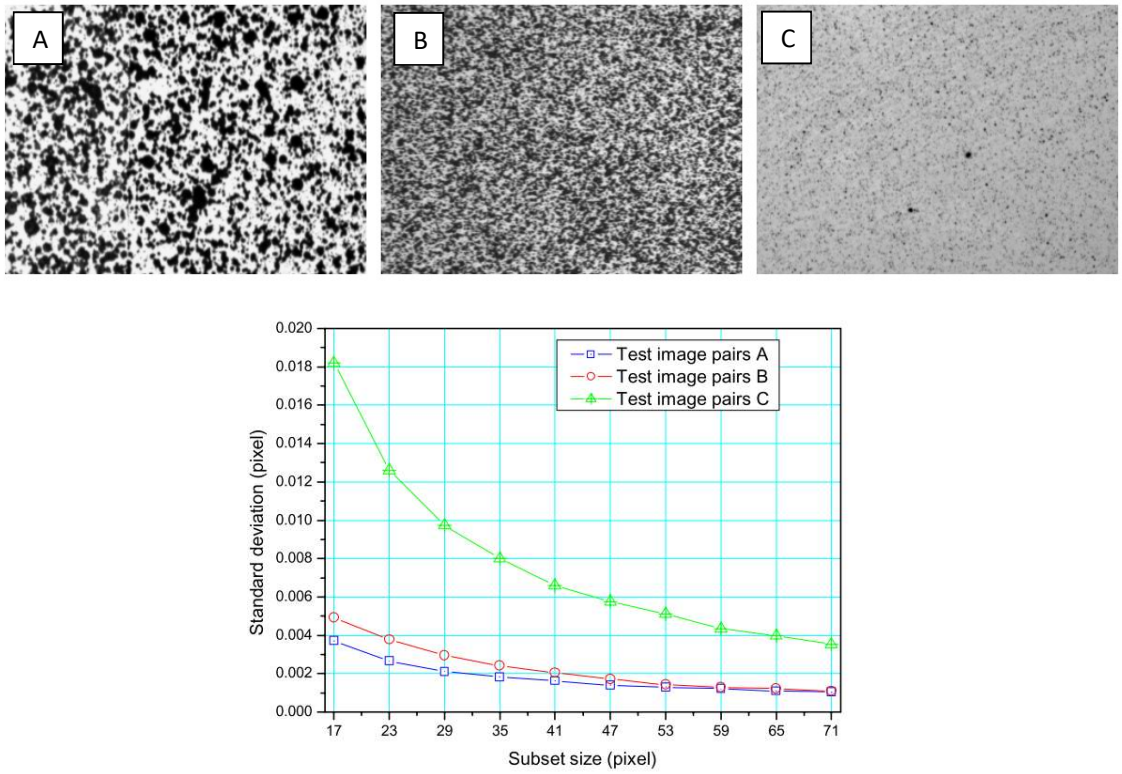

Figure 2.7-4 Decreasing standard deviation in calculated displacement with subset size (Pan et al. 2008)

The above also shows that a single subset size is not ideal for all speckle patterns and that the correct subset size needs to be discerned for the application that DIC is intended to be used for – creep strain in a FOV the size of a pipework weld in the case of this work.

2.7.3 Step size

The step size is the spacing between centres of the subsets in the reference image of a set being analysed. It is measured in units of pixels and will determine the distancing between data points, both in the vertical and horizontal directions in the image frame of reference. A decrease in step size will hence also result in a higher density of data points per area.

Literature focussing exclusively on the relation between step size and accuracy was found to be scarce, with most of the found literature using only a few variations in step size, if not settling on a single step size altogether. Hence this parameter is explored further in section 3.7.

Some work found on varying step size was done by (Lava et al. 2010), who studied the effects of step size on the strain values obtained from DIC analysis of heterogeneous deformation of a bi-axial tensile specimen. They define a so-called *smoothing area* as [(N-1) × step size] + 1, where N is the side length of an N×N subset; and used step sizes and subset sizes that would have a constant *smoothing area* of 13×13 pixels. They then observed the average and standard deviation of strain in the vertical, horizontal and shear directions. For this data (Figure 2.7-5), they infer that strain

differences between the three step size settings are minor, indicating that the step size can be changed as long as the pixel dimensions of the smoothing area are constant.

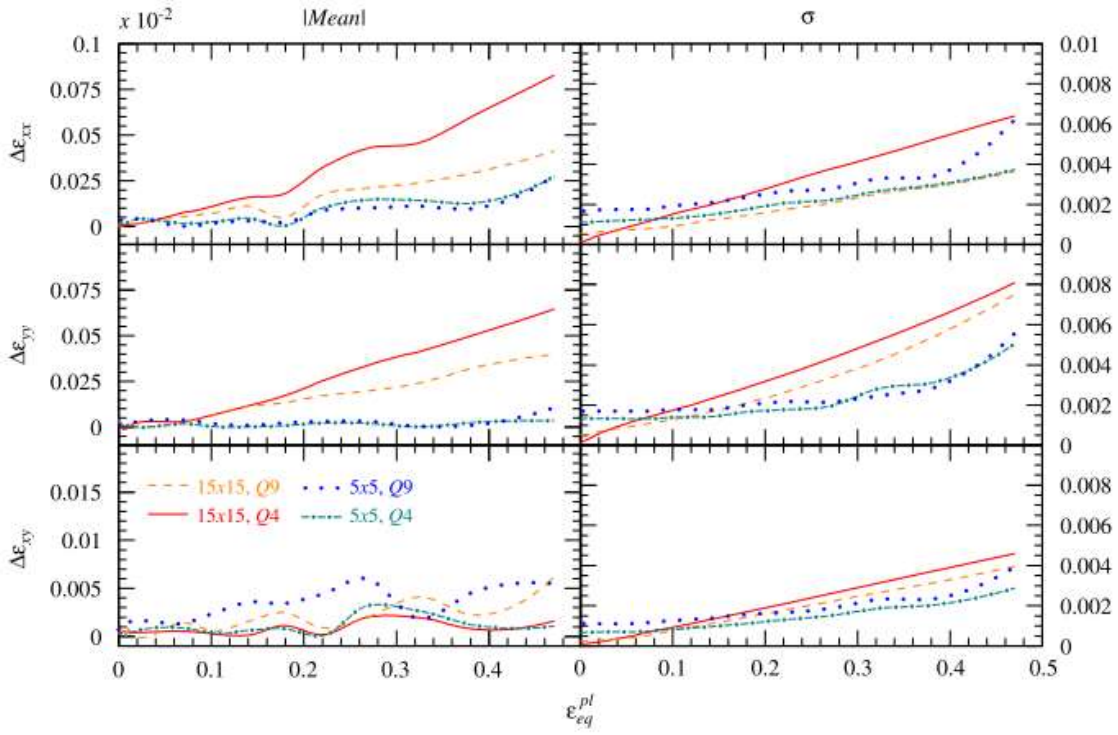

Figure 2.7-5 Effects on DIC strain by changing step size (but compensating with subset size, to keep the calculated smoothing area constant) (Lava et al. 2010). *The units for both the axes are dimensionless, i.e. strain.*

2.7.4 2D and 3D DIC

Deformations can be captured in two or three dimensions. As has been dealt with up to this point, 2D DIC measures deformations within a plane parallel to that of the image sensor. This is extended to out-of-plane (3D) deformations by including images of the same object from additional cameras to enable stereoscopic vision. 3D DIC however needs a calibration process to ascertain the positions of the image sensors relative to each other and the object of interest.

In their work on the effects of out-of-plane motion on 2D and 3D DIC measurements, (Sutton et al. 2008) translated a speckle-patterned surface fore and aft relative to three DIC setups: 2D DIC paired with an ordinary 55mm lens; 2D DIC with a telecentric lens; and 3D DIC using two cameras. They then measured the artificial strains generated with the translation, which should ideally be zero since no real strains were applied to the speckle-patterned substrate. The differences between the three chosen setups can be seen in Figure 2.7-6, Figure 2.7-7 and Figure 2.7-8, where order-of-magnitude differences in measured normal strains are noted (see scale on vertical axis). The most error-resilient setup to out-of-plane motion would be the 3D setup, with runner-up being 2D DIC using the telecentric lens. It is recommended in their work that if a standard lens in a 2D DIC setup is used, that the distance between the camera and the object be maximised within the optic capabilities of the lens to minimise the errors. This is however a last resort if out-of-plane measurements are expected, since the errors generated with this setup are exceedingly large.

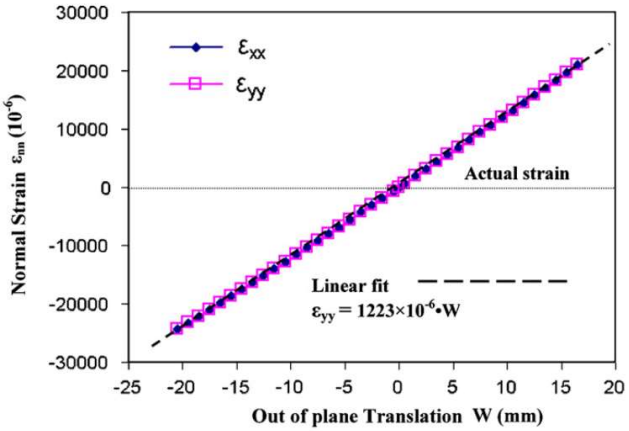

*Figure 2.7-6 2D DIC using a **standard** lens. Normal strains measured during out-of-plane translation. (Sutton et al. 2008)*

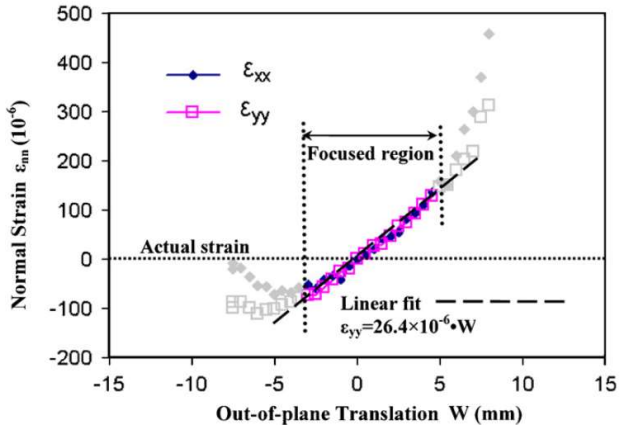

*Figure 2.7-7 2D DIC using a **telecentric** lens. Normal strains measured during out-of-plane translation. (Sutton et al. 2008)*

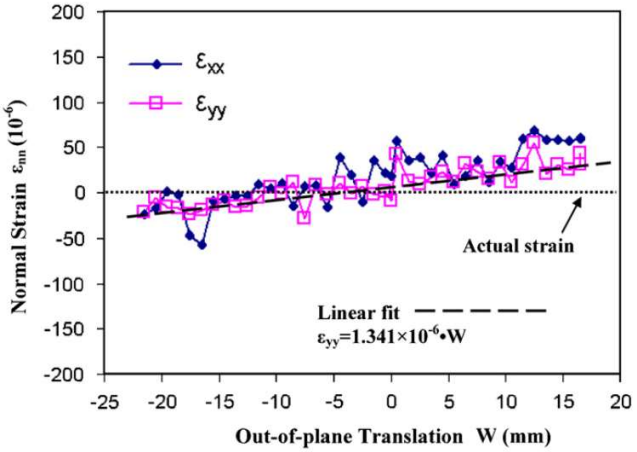

*Figure 2.7-8 **3D** DIC using a standard lens. Normal strains measured during out-of-plane translation. (Sutton et al. 2008)*

This work is corroborated with the later work of others. (Pan et al. 2009) recommends the use of a telecentric lens for 2D DIC setups to mitigate perspective errors and the consequent measurement of artificial strains. Additionally, Figure 2.7-9 (Left) shows a setup used by (Hoult et al. 2013) whereby the distance of a speckle-patterned specimen's surface to the camera (with a non-

telecentric lens) is changed by *dy*. As the specimen moves closer to the camera, the spacing between speckles will optically be perceived to get larger and further apart - perspective error. (Hoult et al. 2013) observed that the DIC software would comprehend this as a strain, even though the specimen has not undergone any physical deformation. These results are shown in Figure 2.7-9 (Right), where an increase in the translation (dy) of the specimen is seen to generate a larger artificial strain. This was repeated at several starting distances from the specimen (y), which showed that a starting point closer to the camera exacerbated the aforementioned phenomenon. (Hoult et al. 2013) concurred with (Pan et al. 2009) on the use of a telecentric lens to mitigate this phenomenon.

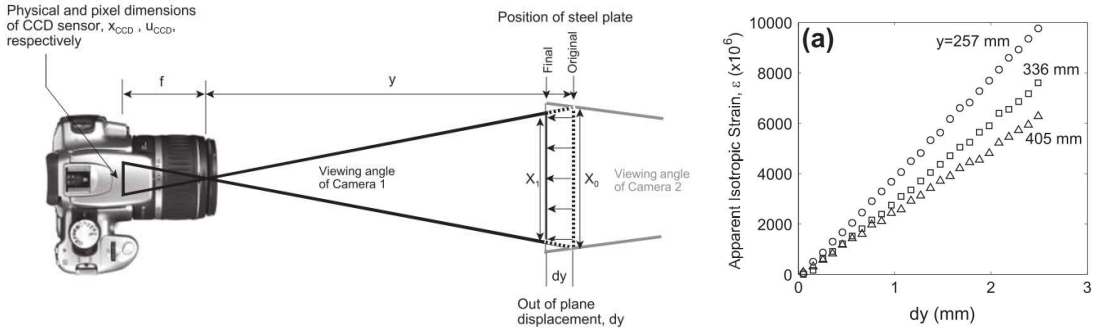

Figure 2.7-9 Left: Schematic of the experimental layout used by (Hoult et al. 2013)*. Right: Apparent strain resulting from moving the specimen further/closer from the image sensor.* (Hoult et al. 2013)

Qualitatively, the setup of 2D DIC is simpler as there is less equipment to set up and no spatial calibration process, automatically eliminating some potential sources of error and making it more mechanically robust. In their review on 2D DIC, (Pan et al. 2009) list advantages including simple experimental setup and specimen preparation, and low equipment requirements for field use.

2.7.5 Calculation of strain

The process of determining strain in DIC is explained with the aid of the schematic in Figure 2.7-10 generated by (Pan et al. 2010). The reference subset (of size N by N) in the reference image has a central pixel located at position x and y in the co-ordinate system with origin in the top left corner of the image. Subsequent to undergoing deformation, the position of the target subset is located within the deformed image and a vector is generated from the reference subset's centre to that of the target subset. This vector represents the deformation undergone. Numerical differentiation of this vector then yields the strain. This process is repeated with every subset to generate the strain field.

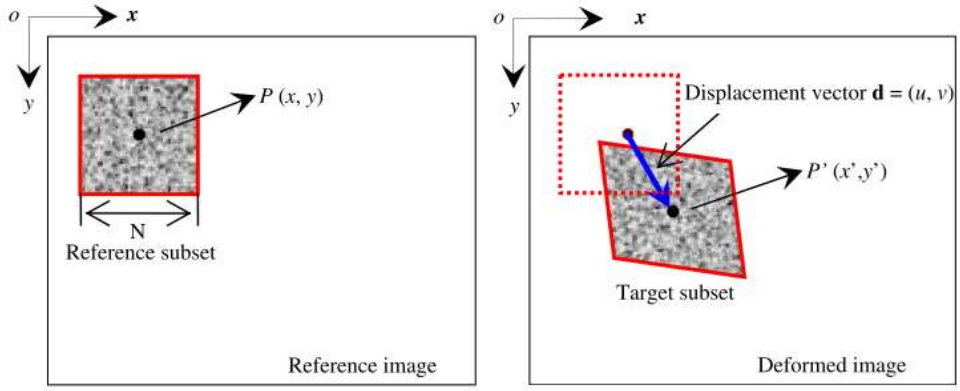

Figure 2.7-10 Left: Subset with the reference image. Right: New position of the subset within the deformed image at a later time. (Pan et al. 2010)

This Literature Review systematically looked at the major concepts that will be encountered in this work. Creep damage in the context of power stations was first looked at. Digital Image Correlation was then introduced and the hardware discussed. Thereafter, an investigation into speckle patterns and their import to strain accuracy were looked at. The section concluded with an in-depth look into the working mechanisms and important parameters of DIC.

3 Experimental Methodology

This chapter is broken up into several sections and the layout and workflow of these sections is summarised below. DIC hardware and speckle pattern application are first decided upon and justified. Candidate speckle patterns are analysed and characterised, and a decision on an adequate candidate made. This information yields an optimised DIC setup upon which the effects of DIC parameters on strain error can be investigated. The chapter is concluded with the methodology used to determine the effects of temperature on the accuracy of DIC, which is designed to gain insight into the feasibility of online DIC power plant measurements.

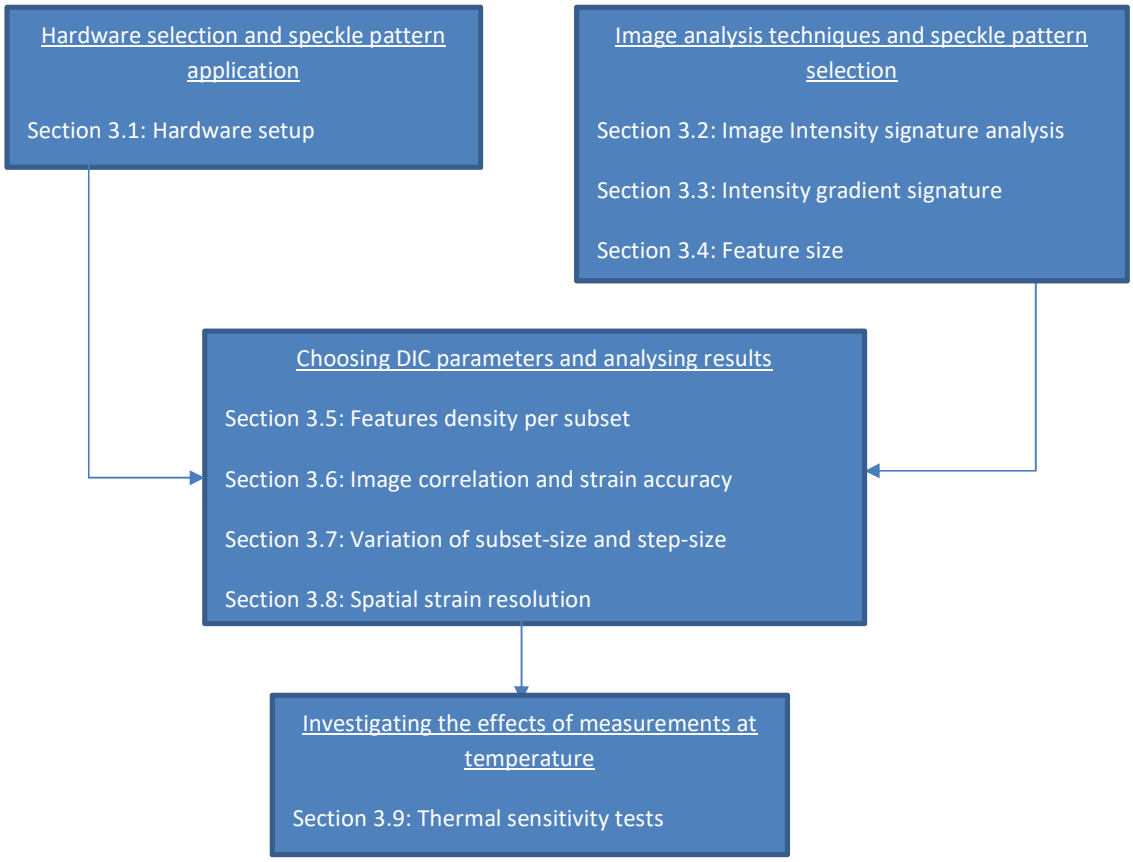

3.1 Hardware setup

This section looks into the selection and justification for the use of the camera, lens, data acquisition unit, specimens, and method used to create the speckle patterns. This section addresses Objective 2 of this work.

Given DIC's scale independence, the hardware setup needs to be optimised for the strains expected in pipework creep strain. The capacitive strain gauges used successfully within Eskom plant to monitor creep strain are capable of resolving strains between 5 and 20 με (van Zyl et al. 2005). This will be used as the benchmark for the strain performance testing of DIC.

A single camera, 2D DIC setup was decided upon, which is mechanically simpler than its 3D counterpart thus making it more robust for potential industrial field operation. The deformation of a pressurised pipe in the radial direction (i.e. out of plane relative to the image sensor) is of lesser

importance. Thus, regardless of 3D DIC being an order of magnitude less sensitive to out of plane motion (section 2.7.4), a 2D DIC setup suffices adequately for this application. Put differently, the greatest stresses, and hence strains, posed to a pressurised pipe are in the hoop and axial directions and these are the strains that this work is concerned with.

The camera used was the Imager E-Lite 5M, sold under the LaVision brand. It incorporates a 2/3" Sony ICX625 CCD sensor. CCD sensor technology provided the desired superior noise performance compared to the CMOS counterpart. The slower read-out speed of the CCD sensor is irrelevant as measuring creep strain does not require high frame rates. A CCD sensor's higher power consumption was irrelevant since it would not be powered by a battery. The sensor's specified resolution of 2456 × 2058 pixels (5 Megapixel), fitted into an active area of 8.5 mm× 7.1 mm (2/3"), results in a pixel size of 3.45 × 3.45 μm^2. The Imager E-Lite 5M has an integrated Analogue to Digital Converter specified with a bit depth of 12bits. The camera body is manufactured with a C-mount for interfacing with compatible lenses.

It was desired to focus on a FOV within a tensile specimen representative of the area in which the pipework HAZ, typically several millimetres in width, would fit. To this end, the Opto-Engineering TC23009 bi-telecentric lens was used, which yielded a FOV of 8.44 mm × 7.06 mm when coupled to a 2/3" image sensor. It was seen in section 2.7.4 that a telecentric lens is recommended to minimise artificial strains. The TC23009 is a prime lens, omitting the focussing mechanism which eliminated the need to re-establish the setting between tests and hence reduced potential variability. It also increases the robustness of the DIC system, having fewer moving components in comparison with a zoom lens. Its working f-stop number is specified as 11 which results in a narrow depth of field of 0.9 mm. The camera fitted with the telecentric lens can be seen in situ in Figure 3.1-1. The LED light arrays that were used to illuminate the specimens are also noted in the figure. The tensile specimen, tensile testing machine and strain gauge setup will be elaborated on in sections to follow.

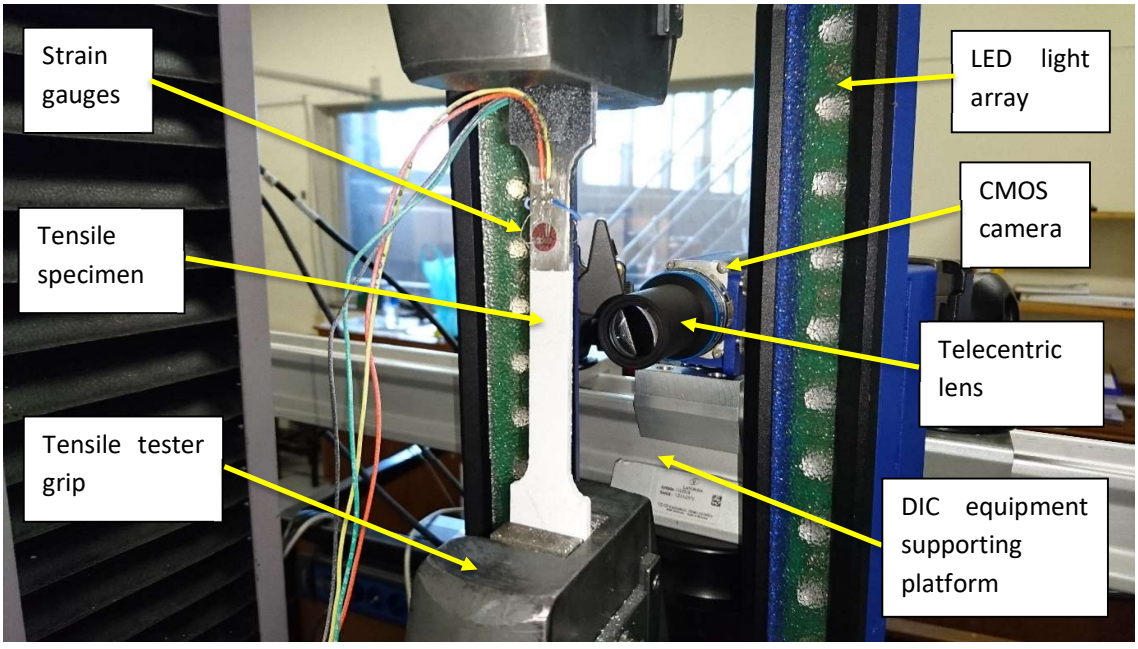

Figure 3.1-1 Equipment setup for capturing strains in the tensile specimens

Actuation of the hardware was done centrally via the LaVision Programmable Timing Unit (PTU). This facilitated the camera triggering, exposure time, LED light triggering, LED lighting duty cycle, etcetera. The PTU, in addition to the aforementioned pieces of hardware, were securely supported on a rail that mounted on an adjustable tripod. The control signals and data transfer to/from the PTU were done via USB connection to a computer running the LaVision proprietary software - DaVis version 8.3.1.

Barring the tests at temperature which will be detailed in section 3.9, all testing was done on laser-cut tensile dog-bone specimens. Given proper alignment within a tensile testing machine, dog-bone tensile specimens will undergo a uniform strain throughout their gauge area. This proves useful to compare the strain seen by DIC equipment in one area of the tensile specimen to strain gauges in another area close by. The dimensions of the tensile specimens are shown below in Figure 3.1-2. The geometry satisfies the requirements of ASTM E8/E8M – 15a: Standard Test Methods for Tension Testing of Metallic Materials. The specimens were made of Domex 355, a structural steel that it is well known in industry, has typical steel properties (a Young's Modulus of 210 GPa at room temperature and a Poisson's ratio of 0.3), and was readily available. The specimen's y axis is defined as being parallel to the specimen's axial direction. This frame of reference can be seen in Figure 3.1-2 and this convention used throughout this work.

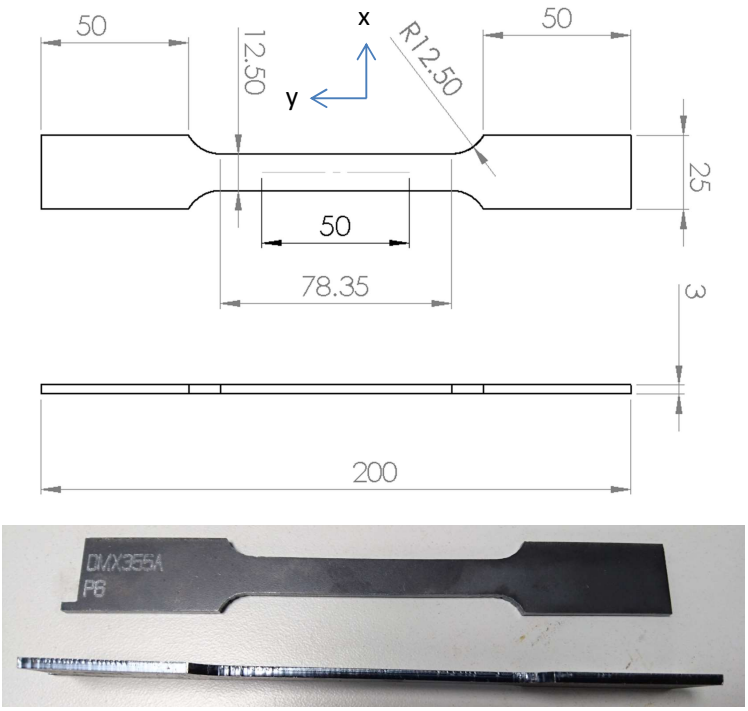

Figure 3.1-2 Dimensions of dog bone specimen laser cut from Domex 355 MC steel. Reference co-ordinate system also defined.

Several dozen speckle patterns were applied to the tensile specimen's gauge area either by way of an airbrush (TradeAir PAB1209) or an aerosol spray can. The paint used for the airbrush was acrylic PVA manufactured by Dulux in a *matt* derivative to minimize reflection from the LED lighting. Reflection in an image obscures the data behind it, compromising the DIC analysis in that region. The

aerosol spray can paint was a high temperature product manufactured by VHT. As was recommended in literature (Sutton, Orteu, and Schreier 2009), (Lionello and Cristofolini 2014) and (Crammond, Boyd, and Dulieu-Barton 2013), the speckle pattern should be isotropic, non-periodic, stochastic and highly contrasted. It was endeavoured to adherence to these recommendations as far as practical in the creation of the speckle patterns.

Black speckles (features) were applied atop a white base/background. This was done on the gauge area of the tensile specimens. Speckle pattern application parameters that were experimented with were: the degree of paint thinning; air pressure; stand-off distance from the specimen; and number of speckle coats applied. It was found that the white basecoat should be allowed to dry well before the black speckles are applied. Failing to do so yielded speckles whose edges blur into the wet white paint and the strong contrast desired between speckles and background was diminished. Of the several dozen speckle patterns created, eight were chosen that were seen to be significantly different from each other while still adhering to the aforementioned recommendations.

In a power station context, the speckle pattern applied to the weld surface would be required to endure high temperatures for durations in the order of months, at minimum. It is not part of the scope of this work to determine an application technique that would yield a speckle pattern robust enough to endure these conditions. It is assumed that ultimately a speckle pattern developed by an industry player, that is adequate for power station applications, will be used if DIC were to prove feasible for this use. This would be done either through licensing such that it can be applied in-house or contracting such that the hypothetical company applies the speckle pattern when and where needed. In order to be optimal, a speckle pattern supplied by the said industry player would also need to have similar characteristics to the ones recommended by literature and hence be similar to the ones used in this work.

These speckle-patterned tensile specimens were loaded into a tensile testing machine (MTS Criterion 44) and the DIC equipment set up around it as is demonstrated in Figure 3.1-1. Using the tensile tester to mount the specimens was superfluous support for the specimens that required only speckle analysis (no straining). This however facilitated a standard which promoted that parameters dependant on physical setup, such as field of view and focal distance, be more consistent and thus reducing variability between tests.

Before the strain accuracy of DIC could be established, there existed the need to do further analysis of the speckle patterns, over and above the qualitative visual checks. Doing so gives assurance in several domains. Firstly, assurance is had that the speckle pattern used adheres to what research recommends is optimal. Secondly, assurance is had that the imaging system is correctly set up to optimally capture the speckle pattern. Thirdly, the capability to identify a given speckle pattern, such that reference to it can be made, is unlocked and meaningful comparisons with other work, past and future, can be made.

Several tools were used to isolate speckle pattern attributes and, in concert, these attributes would then constitute the characterisation of the speckle pattern. In addition to the more qualitative attributes recommended by literature: isotropic, stochastic and highly contrasted; the attributes that were focussed on were: intensity, intensity gradients, feature size and features per subset. The manner in which each of these attributes was tested for is detailed in the following sections.

3.2 Image Intensity signature analysis

DIC correlation algorithms make use of pixel intensity data in the subsets to track the movement of the substrate which the speckle pattern is applied to. This section looked at analysing the intensity signature in the images of a given speckle pattern. This information was used for quality control of the captured images as well as characterisation. Over and/or underexposed pixels can be identified and the black speckle to white background composition of a speckle patterns characterised.

Prior to taking images of the speckle patterns, the integrity of the image sensor was ascertained by imaging a purely white page to inspect for any dead pixels that were not registering light. None were found and the camera was focussed on the gauge area of the tensile specimens and images of the individual speckle patterns captured. An example can be seen in Figure 3.2-1. The longer edge of the image sensor was always aligned with the y (axial) direction of the tensile specimen's gauge area.

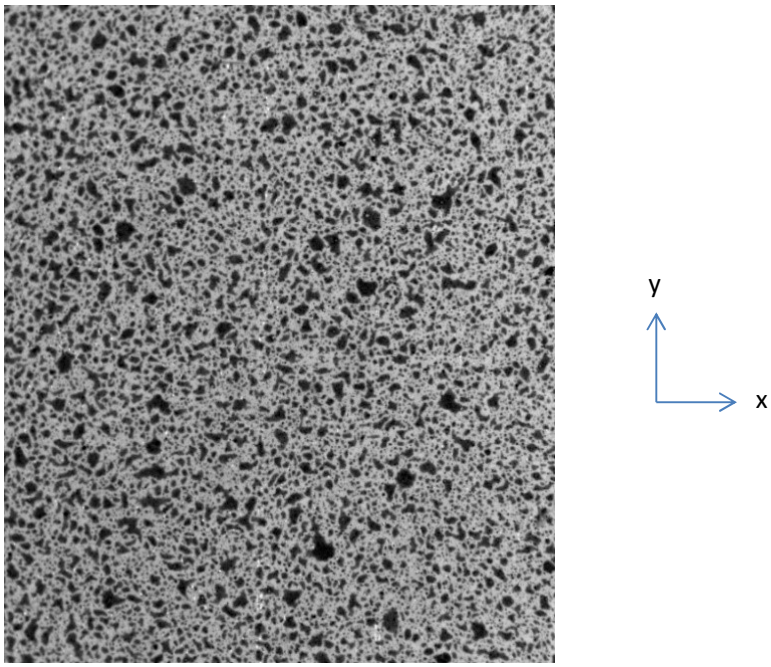

Figure 3.2-1 Example of speckle pattern imaged with the setup chosen in section 3.1.

Of the multitude of speckle patterns created in section 3.1, eight that adhered to the basic literature recommendation (again: isotropic, non-periodic, stochastic and highly contrasted) were chosen to be analysed and exported from DaVis in Tagged Image File (TIF) format. This *lossless compression* format was chosen to preserve details that other compression formats may lose. The file header tags also provided Meta data that facilitated the storage and management of the data in this work.

The images were opened in ImageJ 1.50i, an image processing and analysis application. It features open source, purpose-built functions and there exists a strong developer community which facilitated the availability of niche plugins and help resources. Programming of Macros is also featured within ImageJ, which was used extensively in later sections to do batch processing of image data. Once opened in ImageJ, each speckle pattern's intensity histogram was generated using the *Histogram* function, which additionally outputs key statistical data about the calculated distribution. The histogram along with its statistical data for the image noted in Figure 3.2-1 can be seen below in Figure 3.2-2.

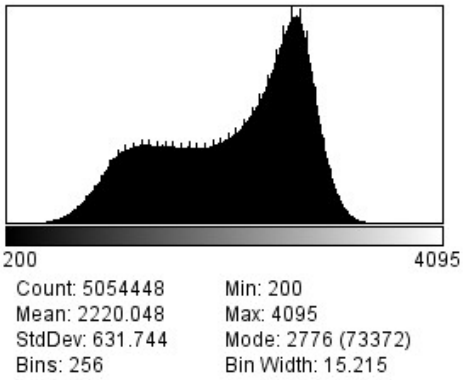

Figure 3.2-2 Histogram example generated from a speckle pattern image.

This section had as input the image of a given speckle pattern and by way of software processing output the histogram and statistical data. It was used to assess the setup of the DIC imaging system and the pixel intensity distribution of the chosen speckle patterns.

3.3 Intensity gradient signature

Intensity gradients were seen to affect many aspects of DIC and are thus here quantified. The same eight speckle patterns analysed in section 3.2 were analysed here - as well as for the remaining sections on speckle pattern characterisation. The intensity gradients were extracted from the images using modified MATLAB code originally written by Thorsten Becker[1]. MATLAB (version r2014a) was used because of its capabilities to eloquently process large matrices of image intensity data.

To illustrate the functioning of the code, two computer generated black speckles on a bright background are presented in Figure 3.3-1. The left speckle shows a sharp (high gradient) edge and the same speckle is blurred using a gaussian filter on the right.

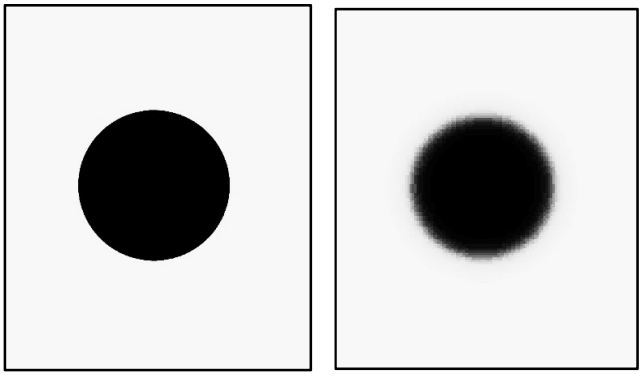

Figure 3.3-1 Computer generated speckle. Left: Sharply defined dark speckle on a white background. Right: The same speckle pattern but with the edges blurred using a Gaussian filter.

A loop reads the images into memory. The pixel intensity values were then numerically differentiated using the *gradient* function, whereby the central difference for a given pixel is calculated using the pixel intensity data surrounding it. Both the partial derivative in the image's

[1] Senior lecturer in the department of Mechanical and Mechatronic Engineering at Stellenbosch University. tbecker@sun.ac.za.

horizontal as well as vertical direction was calculated. Sudden changes from the white background to a black feature in a speckle pattern would yield larger intensity gradients.

Now if the aforementioned partial derivative in the horizontal direction were calculated across the middle of the (symmetrical) speckle, a positive gradient would be seen on the left edge and a negative on the right edge – since the change in intensity would be exactly equal in magnitude but opposite in sign moving from left to right. The same effect would be found when taking the partial derivative in the vertical direction. Thus, absolute values of the results from the partial differentiation were calculated to eliminate this irrelevant effect.

The two resulting matrices of derivatives (vertical and horizontal partial derivatives) were concatenated to increase the statistical significance of the data. This could be done because the speckle patterns were isotropic and hence there will be no preferential direction in terms of intensity gradient.

A histogram is then generated for this data, as is observed in Figure 3.3-2 for the two generated speckles in Figure 3.3-1. A large abscissa value indicates a high intensity gradient and thus a sharp edge on the speckle, as is noted in the histogram on the left (value of around 2050). Put differently, a sharp transition in a speckle pattern from pure white to pure black would yield a large intensity gradient and this would decrease in magnitude as the transition becomes less sharp. Since the distributions will tend to be heavily skewed for a real speckle pattern, more similar to what is seen in Figure 3.3-2 on the right, the median was used as the preferred measure of central tendency to characterise them. The medians for the two generated speckles were 2048 and 3.5 for the left and right histograms respectively, illustrating the large difference in sharpness between the two speckles.

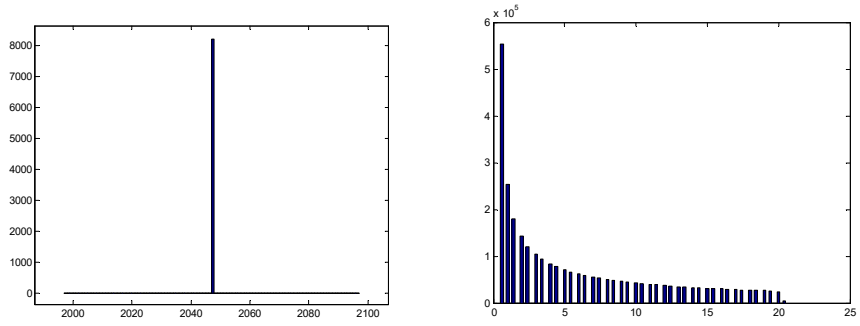

Figure 3.3-2 Histograms of intensity gradients for the computer-generated speckle.

This section showed how a speckle pattern image's intensity gradient was characterised, outputting a histogram from which statistical data can be pulled.

3.4 Feature size

Feature size will impact directly on the number of features that can fit into a given subset-size, and consequently affect the efficacy with which the correlation algorithm is able to track the movement of that subset. This in turn affects accuracy and thus this parameter has direct bearing on the main objectives of this work.

Elementary particle analysis was used to quantify the feature size, using ImageJ to do the processing. The steps in this processing is detailed here. A binary image, with the speckle pattern features delineated, was needed and several methods were trialled to achieve this end. The combination of processing steps (ImageJ functions) that yielded the most satisfactory results are illustrated in Figure 3.4-1 and were:

1. Make Binary
2. Despeckle
3. Watershed
4. Find Edges
5. Analyse Particles

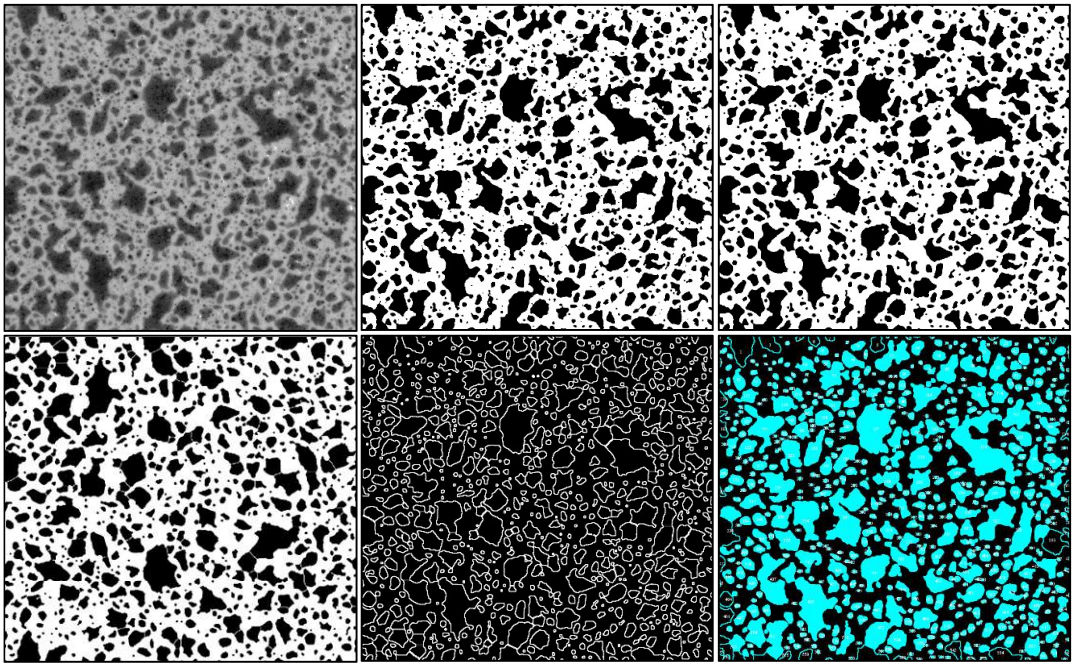

Figure 3.4-1 Image processing steps moving from top left to bottom right. 1 - Original Image, 2 - Make Binary, 3 - Despeckle 4 - Watershed, 5 - Find Edges, 6 - Analyse Particles

The *Make Binary* function was used as opposed to manually thresholding the image for the sake of consistency. That is, it was thought important to do this algorithmically as opposed to manually in order to maximise repeatability. The algorithm works by dividing up the image into *objects* and *background*. The function takes a test threshold and calculates the average of the pixels at (and below) the said threshold and that of the pixels above. These two values are then averaged and the threshold incremented. The process repeats until the threshold is larger than the composite average.

The *Despeckle* function was used to remove finer outliers. It is a median filter that replaces each pixel with the median value in its 3 × 3 neighbourhood. *Watershed* separated conglomerates of features that clumped together because of overlapping paint drops during the speckle-patterning process – this isolates individual speckles. *Find Edges* finally delineated the individual features. The *Analyse Particles* function was then used to count the number of pixels in each delineated feature. The details of the latter three functions are beyond the scope of this work and the reader is directed to the ImageJ documentation ("ImageJ User Guide" 2017) for further details.

This data was exported to MS Excel and the *Data Analysis* toolbox used for statistical analysis, where the median feature size was ascertained. An example of the distribution can be seen below in Figure 3.4-2.

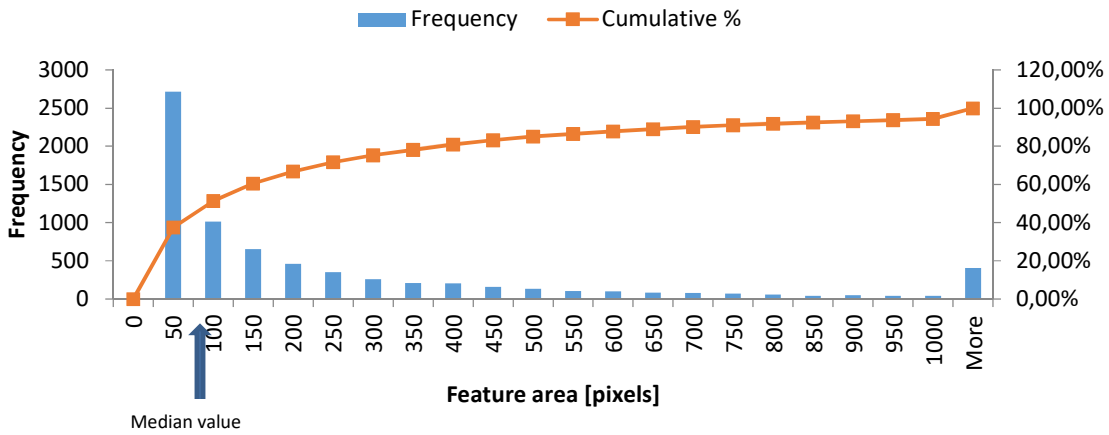

Figure 3.4-2 Histogram of the speckle area distribution

Immediately noticeable is that the feature size distribution is seen to be heavily skewed to the right - with a statistical Skewness value of 3.9 in the case of Figure 3.4-2. The vast majority of feature observations were only several pixels in size. Features larger than 1000 pixels in area make up a contribution less than 6% of the total number of features, as can be noted in the inflection at the end of the cumulative percentage plot. It was at first assumed that the distribution of randomly applied features would yield a normal distribution – which, as can be seen, was not the case here. This example was not an isolated case and therefore further investigation was deemed necessary.

It was subsequently hypothesised that the distribution might be skewed to the right because the pixel resolution was not high enough to adequately sample the smaller features – that is, the smaller features were being under sampled because the pixels were too large. Any feature smaller than a certain threshold would simply be registered as having a size of several pixels and hence the large count of observations at this end of the histogram. This hypothesis was subsequently tested.

If the aforementioned were the case, increasing the pixel resolution by imaging the speckle pattern under an optical microscope (Figure 3.4-3) would oversample even the smallest features, ensuring that there was no under sampling, and hence allow the hypothesis to be tested. The FOV that could be imaged under an optical microscope is much smaller than that captured by the original setup. Therefore, for statistical significance, microscope images of several neighbouring areas were captured and digitally stitched together, and this resulting image analysed.

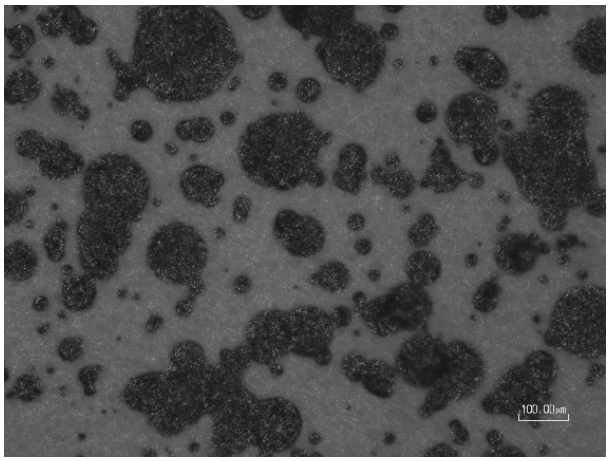

Figure 3.4-3 Single constituent image taken with an optical microscope, forming part of a larger stitched image for analysis. Scale bar is 100 µm.

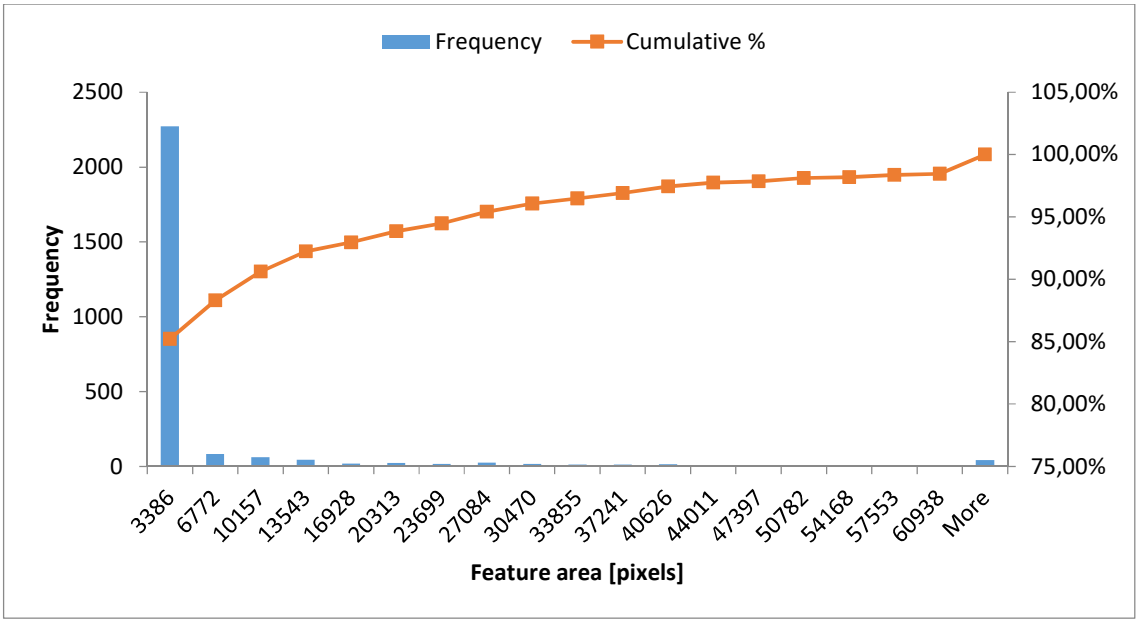

Figure 3.4-4 Histogram of data from the microscope acquired images

As can be noted in Figure 3.4-3, the magnification is sufficient to even discern details within each feature and so was deemed adequate. The results of the feature size analysis done to the stitched image can be seen in Figure 3.4-4. Here, a similar trend, albeit with fewer data points, as was observed in Figure 3.4-2 can be seen, disproving the hypothesis of smaller features being aliased and resulting in a disproportionate number of smaller features being registered. It is thus accepted that the nature of the distribution is to be skewed as oppose to normally distributed as was originally assumed. The shape of the distribution also agrees with the data from (Rajan, Rossol, and Zok 2012) seen in the literature review. All images from this point onwards are taken with the normal setup – i.e. not with a microscope.

The median was used as the measure of central tendency because of its resilience to skewed data as well as outliers. The median speckle area for the example speckle pattern, derived from the data

shown in Figure 3.4-2, was calculated to be 94 pixels, approximately shown by the arrow in the figure.

It is noted that this method of ascertaining the median feature size is limited to speckle patterns that have discrete, easily identifiable features. Seen in Figure 3.4-5 below are the unprocessed and processed images of a speckle pattern whose features, visually, are less easily discernible from each other. It is easily understandable that if the individual features are not easily discernible by eye, software processing will likely be less capable of finding the edges. Therefore, prior visual inspection of a speckle pattern to check the suitability for feature-size characterisation is vital.

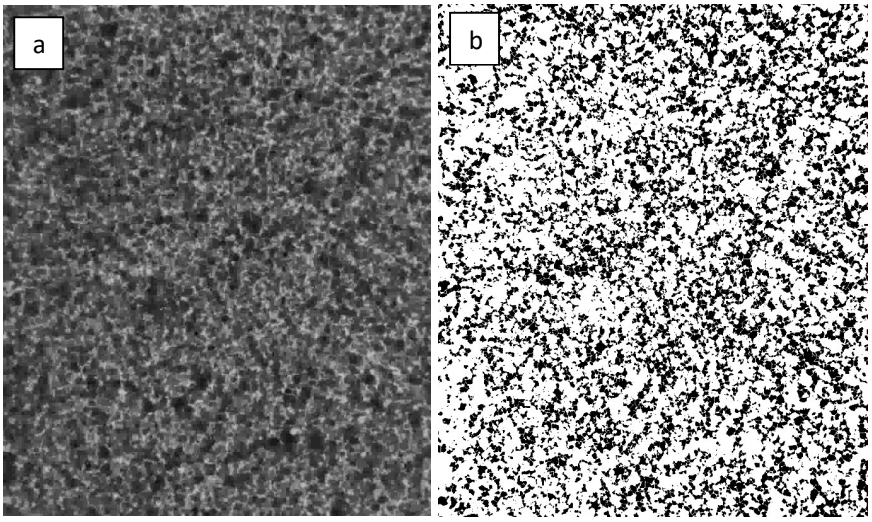

Figure 3.4-5 Less successful delineation and isolation of features. (a) unprocessed and (b) processed.

In this section, a tool was developed to quantify the size of speckle pattern features in support of objective 3. The output was the median sizes of features within a given speckle pattern. It is also shown that this method only works for speckle patterns whose features are clearly defined and visible. At this point, a decision was also made as to the speckle pattern that would be used for the testing in the next several sections.

3.5 Features density per subset

For a given image sensor with a specified pixel resolution, the number of features in a subset will not only depend on the previously looked at feature size, but also on the size of the subset chosen. That is, the larger the subset-size is, the more features will be encompassed for a given speckle pattern. This section is closely linked to speckle pattern characterisation, but also introduces the first steps in the decision-making process for subset-size and step-size selection, which will be developed in section 3.7. This data will be used to comment on the influence of feature density on the accuracy of DIC strain measurements.

The metric for subset-size in DaVis is the edge length (in pixels) of a square subset. It is always an odd number to ensure that there is an integer-valued central pixel, representing the position and subsequent movement of the subset in question. The number of features per subset was analysed by cropping out ten (for statistical significance) squares (identical in pixel size to the chosen subset-size) in the image. The said cropped out squares were spaced corner-to-corner in a diagonal fashion, starting from the top-left corner. This was done to obtain a representative sample across the speckle

pattern. An example of the areas from which the subsets were analysed can be seen in Figure 3.5-1, and the speckles within the sample subsets seen enlarged in Figure 3.5-2. Division of the conglomerated features as a result of the used ImageJ *Watershed* process are noted.

(Bing Pan et al. 2008) and (Rajan, Rossol, and Zok 2012) showed that a larger subset-size would yield a more accurate strain result and so it was thought prudent to start with such a large subset-size. A starting subset-size of 121×121 pixels was initially used as this was the largest subset-size allowable in the version of DaVis used when this work started. Subsequent to this decision, a later version of DaVis became available (8.3.1) which had a maximum subset-size of 255×255 pixels, and this was later made use of as will be seen. However, since significant data had already been captured with the 121×121 pixels subset-size, this was used as an initial size in a large portion of the subsequent testing as it was also approximately (and conveniently) mid-range of the software update's subset-size capabilities.

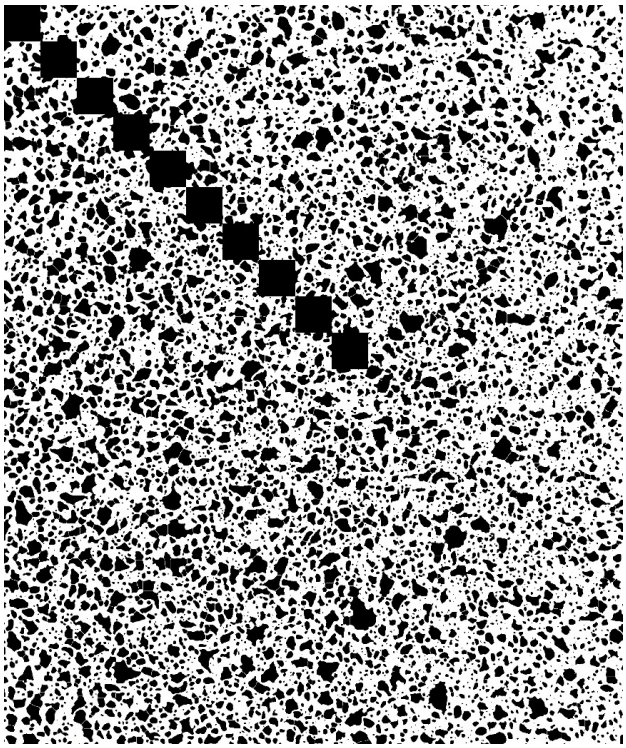

Figure 3.5-1 SP 1 showing areas from which subset samples were taken

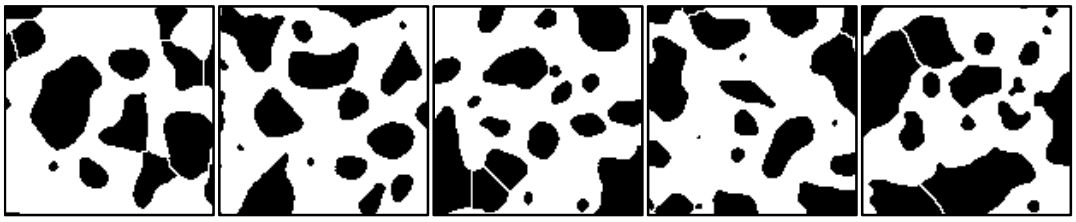

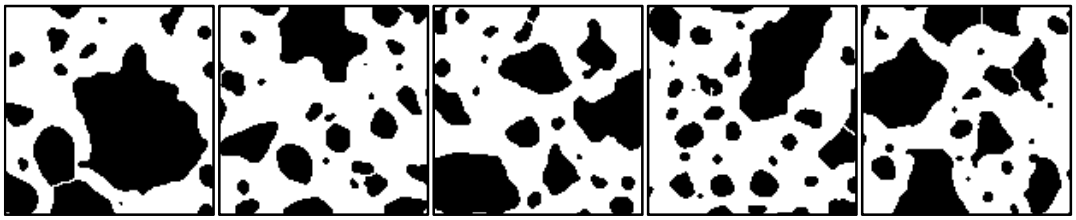

Figure 3.5-2 Cropped subset of the processed image

The number of features, present within the cropped image squares (subsets), was counted with the ImageJ *Analyse Particles* function, and the mean and standard deviation of the ten observations calculated.

It was also of interest to investigate the variability between specimens (inter-specimen). This data would give insight into the variation that might be expected when applying a speckle pattern onto several components in a power station. It is desirable to have consistency between speckle patterns to reap maximum benefit from the setup (cameras, lenses, etc.) optimisation done. In other words, excessive variability in a speckle pattern would nullify the optimisation of hardware and software parameters chosen.

This testing was accomplished by performing the above described procedure on ten individual speckle patterned tensile specimens. As far as practical, the manual spraying was done with the same stand-off distance and same number of paint coats for each specimen. The extensive repetitive ImageJ processing was achieved by coding a custom macro to automate as much of the procedure as possible. This technique, as was with feature size, is only applicable to speckle patterns whose features are easily identifiable.

The testing in this section up to this point was however all for a subset-size of 121×121 pixels. In support of Objective 5 in section 3.7, the subset-size was varied as the independent variable. A subset sizing scheme that changed the subset *area* (and hence information quantity available to the correlation algorithm) was used. The largest subset-size that was allowable by the DaVis 8.3.1 was 255×255 pixels (65 025 pixels). This range (in terms of area) was divided up approximately linearly in increments of 5 000 pixels and rounded off to the closest odd integer (Table 3.5-1). It is noted that the 255×255 pixels and 31×31 pixels subsets diverge from the aforementioned linear scheme and were included to test the extremes of subset-size range.

The sampling of the subsets was updated to encompass a diagonal stretching the width of the image as oppose to the fixed ten-sample regime that was used previously. This was done to maximise data points for each subset-size used. Figure 3.5-3 demonstrates the increasing number of features encompassed in a subset as its size increases.

Subset-size [pixel × pixel]	Equivalent subset area [pixel^2]
255×255	65025
235×235	55225
223×223	49729
213×213	45369
199×199	39601

187×187	34969
173×173	29929
159×159	25281
141×141	19881
123×123	15129
99×99	9801
71×71	5041
31×31	961

Table 3.5-1 Subset sizing scheme with equivalent area.

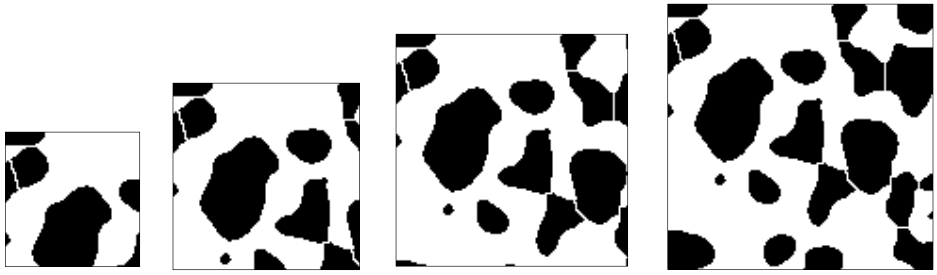

Figure 3.5-3 Features within subsets (top left of the image) of approximately linear increasing area. From left to right: 71×71 pixels, 99×99 pixels, 123×123 pixels and 141×141 pixels.

In this section, the results from the feature density information provided a foundation for understanding the DIC accuracy data which is looked into next.

3.6 Image correlation and strain accuracy

The previous sections set the foundations for the rest of this work. In this section, the strain error that can be expected from DIC for a given subset-size is looked into. This partially addresses Objective 5 of this work.

Strain gauges were adhered to the tensile specimen that had the chosen speckle pattern applied. The strain gauges used were the KFG-2-120-D16-11 - a resistance wire type with the linear expansion coefficient optimised for steel. They are manufactured by Kyowa and constitute biaxial, 0°/90° stacked rosettes, each with a length of 2 mm and a width of 1.2 mm. The Gage Factor was nominally 2.09 with a resistance of 120 Ω. This packaged rosette was oriented on the tensile specimen such that one of the grids aligned with the y axis of the tensile specimen and therefore the other grid oriented with the x axis. Two of these rosettes were used, one on either side of the tensile specimen in a mirror fashion, such that their grids were aligned. The strain gauge leads were wired to maximise the sensitivity in the axial direction, as is detailed in the National Instruments™ white paper on measuring with strain gauges (“Measuring Strain with Strain Gages” 2016). A bridge factor of 2.6 for the full Wheatstone bridge was used, as recommended by HBM (the manufacturer of the QuantumX MX840 amplifier used) in their technical resources (Hoffmann 2001).

The strain gauges were positioned within the tensile specimen’s gauge area to mitigate errors due to end effects where the tensile specimen widens to the grip area. Bonding of the strain gauges was done according to Kyowa specifications. This included the recommended specimen surface preparation and the use of Kyowa branded gauge cement - specified as CC-33A for the KFG type stain gauges. Alignment of the strain gauges was done by measuring the tensile specimen centres with a Vernier calliper and marking them with a fine blade. An option to minimise misalignment

errors would have been to use 3 rosette strain gauges and then, using Mohr's circle, work out the principal strains as was done by (Hoult et al. 2013). However, the increased sensitivity offered by the prior strain gauge wiring scheme is of higher priority. The strain gauges adhered to the specimen can be seen in-situ in Figure 3.1-1. The tensile specimen would only be strained to several hundred microstrain and hence there was little concern about any de-bonding of the gauge from the specimen. Applying only elastic deformation to the tensile specimen also allowed the same specimen to be used several times. The aforementioned strain gauge amplifier was used both to excite and read data from the Wheatstone bridge configuration. Interface with the amplifier was done via the proprietary QuantumX software that facilitated the setting up of the key parameters (bridge factor, gauge factor, etcetera).

Load was applied to the tensile specimen by way of a tensile testing machine (MTS Criterion 44). It is of an electromechanical design equipped with a swappable load cell. Although readings from the load cell were not used when testing DIC error, they were used to validated the strain gauges as will be shown in the next paragraph. A load range of 0 to 2500N was calculated to be needed for the strains to be tested (Table 3.6-1). Thus the 30 kN load cell supplied with the tensile testing machine was used as the lower available load cell was rated at 1kN and would thus be over loaded. The calibration certificate (SHQ-56868 C, in the appendix) stipulated a calculated uncertainty of ±0.26% of reading. The data from the load cell was output to a PC via internal circuitry integrated into the MTS tensile tester itself. The Original Equipment Manufacturer (OEM) specified tensile grips were used for gripping of the tensile specimens (seen in-situ in Figure 3.1-1). Control was done by way of a handheld remote with both coarse and fine control.

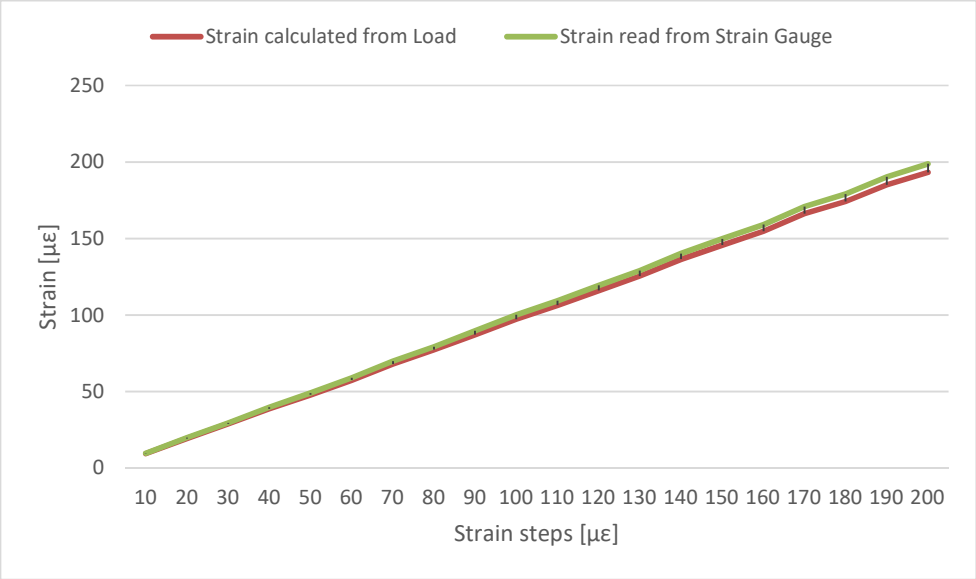

Figure 3.6-1 Validation of strain gauge setup

It was important to validate the strain gauge readouts to ensure that no systematic error had been made in the setup (wiring, selection and inputting of key parameters). The validation was done by calculating the theoretical strain expected and comparing it to the strain gauge readouts. The specimen dimensions were measured with a vernier calliper, and the load applied to the specimen obtained from the calibrated load cell. The results are shown in Figure 3.6-1, where only a marginal

deviation at larger strains is seen between the two data sets. It is emphasised that the calculated strain value is not expected to be more accurate than that of the strain gauge readings because of sources of error such as machining tolerances of the tensile specimen, and unquantifiable misalignment of components in the tensile tester setup. Nonetheless, this would suffice to validate that there was no systematic error in the setup of the strain gauges.

Once loaded into the tensile testing machine, a preload of 100 με was applied to the tensile specimen to remove slack from the system. This step was incorporated subsequent to significant rigid body movement being noticed between sequential DIC images when no preload was applied. At the said 100 με preload, a reference image was captured. The tensile specimen was then manually loaded in subsequent increments of 10 με (nominal) - the lower limit of what the fine-control on the tensile tester was able to repeatedly deliver. An image was captured at each increment. A wide range of strains was desired to maximise the chances of capturing any DIC measurement artefacts. The capacitive strain gauges commonly used within Eskom were seen to be capable of resolving strains between 5 and 20 με. With this in mind, an order of magnitude lager than this upper limit was deemed sufficient (i.e. 200 με). This testing regime is summarised in Table 3.6-1.

	Strain gauge readings	**Nominal strain readings expected from DIC calculations**	**Image type [image number]**
Preload	100 με	0 με	Reference Image [1]
Strain increments	10 με	10 με	Target images [2 to 21]
Final strain	300 με	200 με	Final image [21]

Table 3.6-1 DIC accuracy testing regime

Next the correlation between the images was done in DaVis, encompassing the entire image area and thus maximising available pixel data (i.e. no masking was used). The subset-size was set to the standard 121×121 pixels used previously. This subset-size was used as a baseline and the effects of varying this parameter investigated next in section 3.7. Step-size was set at the maximum recommended by DaVis for this subset-size (60 pixels).

The resulting data was exported as the native .VC7 files that are generated by DaVis and include the image correlation fields and deformation fields amongst other data. A script was used to format the data into MATLAB r2014a data structures for further processing. MATLAB was chosen to do most of the post-processing because it is natively equipped with most of the required mathematical functions; has the programmatic looping abilities to undertake the repetitive aspects of the processing; and is capable of processing exceedingly large matrices of data. The code used was based on that written by Matthew Molteno[2] and Richard Huchzermeyer[3].

Figure 3.6-2 shows the correlation coefficient field calculated arbitrarily for image 21, which corresponds to a nominal applied strain of 200 με (preload). The ranges of the x and y axes are dictated by the number of data points calculated by DaVis, which are directly dependant on the

[2] mattmolteno@sun.ac.za. Postgraduate researcher, Materials Engineering Group, department of Mechanical and Mechatronic Engineering at Stellenbosch University.
[3] rhuchzermeyer@sun.ac.za. Postgraduate researcher, Materials Engineering Group, department of Mechanical and Mechatronic Engineering at Stellenbosch University.

choice of subset-size and step-size. Given this current parameter selection, 35 data points in the x-direction and 41 in the y-direction are generated. The correlation fields were checked to ensure that a high degree of image matching occurred, an average correlation value of 0.9958 for this example.

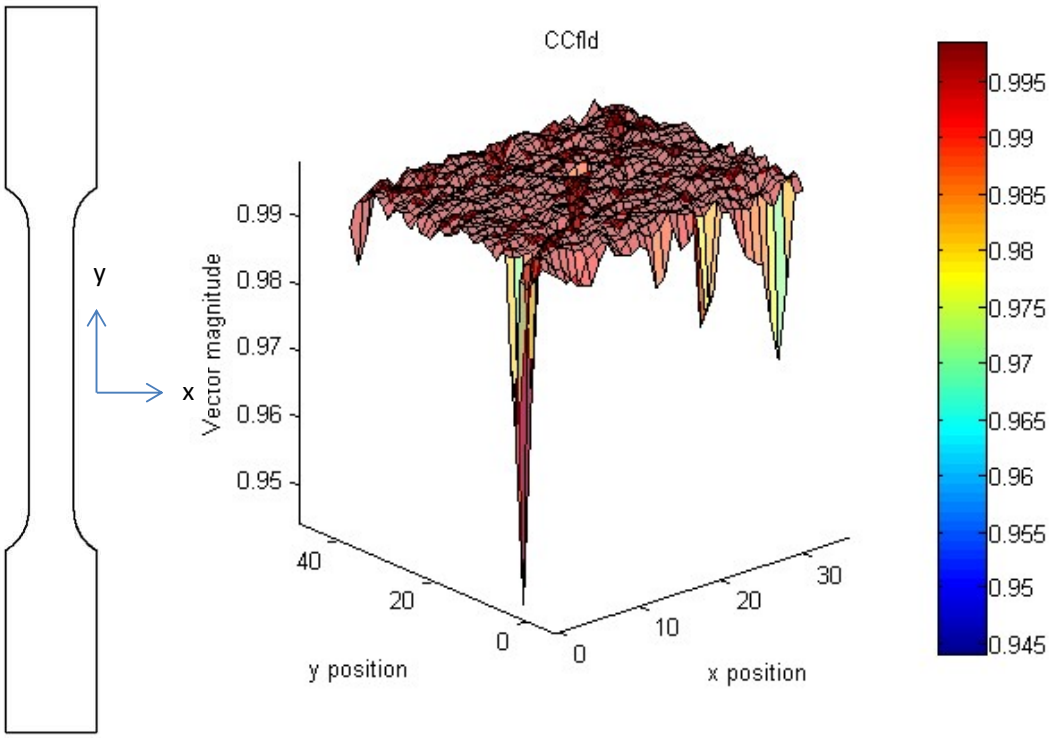

Figure 3.6-2 Correlation coefficient field for image 21.

The fields were also checked qualitatively for any obvious anomalies. Outlying data is evident at the x edges of the field (i.e. top and bottom of the image). This is due to the edge features that are being tracked partially disappearing off the edge of the FOV as the tensile sample elongates. This edge artefact was also reported on by (Marco Rossi and Pierron 2012) and again in 2015 (M. Rossi et al. 2015). As will be seen in Figure 3.6-4, these artefacts carry through to the calculated strain fields. In this work, homogeneous strain fields are expected from a standard tensile specimen and thus averaging of the strain data (that will normalise the edge noise) is possible. This could not be done with heterogeneous strain fields.

DaVis outputs the DIC deformation data in x and y component vectors, and the resultant vector deformation field can be calculated in MATLAB – shown for image 21 in Figure 3.6-3. The deformation units are in pixels and (as has been noted prior) by using images of a calibration plate, conversion of the deformation units from pixels to millimetres is possible. However, since this work is concerned with strain, which is dimensionless, it was unnecessary to perform this extra conversion. The edge artefacts are seen to manifest in Figure 3.6-3 as large gradient changes on the edges. The field in Figure 3.6-3 was flipped about its midline in the x direction. This was done to match the co-ordinate origin of DaVis (originally located at the top left of the image) to that of MATLAB (located bottom left of the field). Physically this would be equivalent to flipping the camera upside-down and imaging from the back of the speckle pattern (through the tensile specimen).

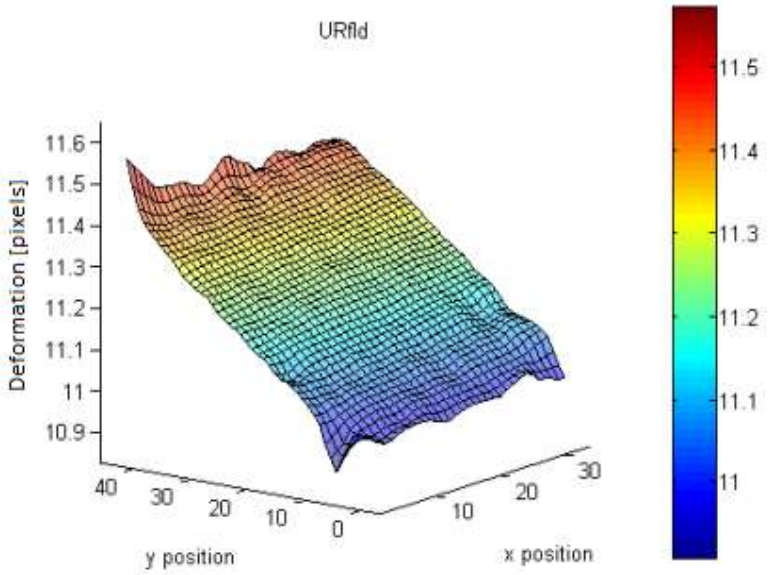

Figure 3.6-3 Resultant deformation field of tensile specimen for image 21.

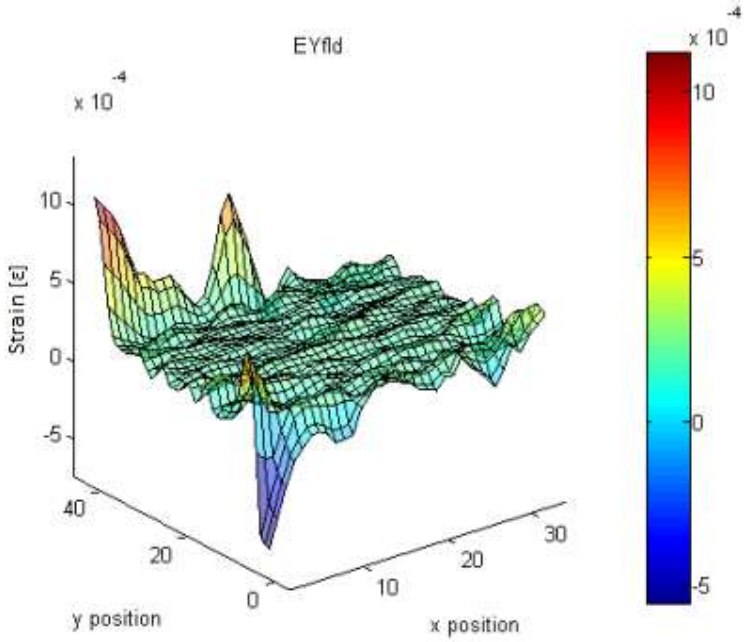

Figure 3.6-4 Strain [ε] field in the y direction for field 21.

The net effect in Figure 3.6-3 is that the largest deformations are seen at the top of the field (larger y values) instead of the bottom where the *moving* grip of the tensile testing machine was clapped onto the tensile specimen and was elongating it. Omitting this transformation would yield negative strains in subsequent strain calculations, where they should be positive. This transformation is done throughout all subsequent fields.

Next the deformation fields were numerically partially differentiated in the x, y and shear directions using the central differencing method, resulting in three strain fields. The reader is guided to see the

online MATLAB gradient function documentation for details on the mechanics of the numerical differentiation used. Figure 3.6-4 above is an example of the strain component in the y direction.

It was practically difficult to ensure precise alignment of the camera sensor's y axis with that of the tensile specimen, much more so than aligning the tensile specimen within the OEM grips. The assumption is made that the tensile specimen is aligned within the tensile testing machine and thus, for practical purposes, the major *principal* strain would be in line with the specimen's y axis. Now by calculating and working with the major principal strain field from the DIC data (as oppose to using the y strain as seen in Figure 3.6-4), the orientation of the sensor becomes irrelevant. i.e. the tensile specimen's major principal strain (assumed to be aligned with the specimen's y axis) is compared to the major principal strain derived from the DIC data (whose magnitude will be the same regardless of sensor orientation). The tensile testing machine is assumed to be installed level and the camera is levelled with a spirit level, thus the tilt between the camera and the specimen is assumed to be negligible. The principal strains are readily calculated from the three component strain fields (x, y, shear) by applying elementary principal strain transformations in matrix form with MATLAB. This aligning transformation was done for all subsequent strain fields.

The principal strain vectors from the strain field can be consolidated into a frequency plot as is shown in Figure 3.6-5, and the average and standard deviation calculated.

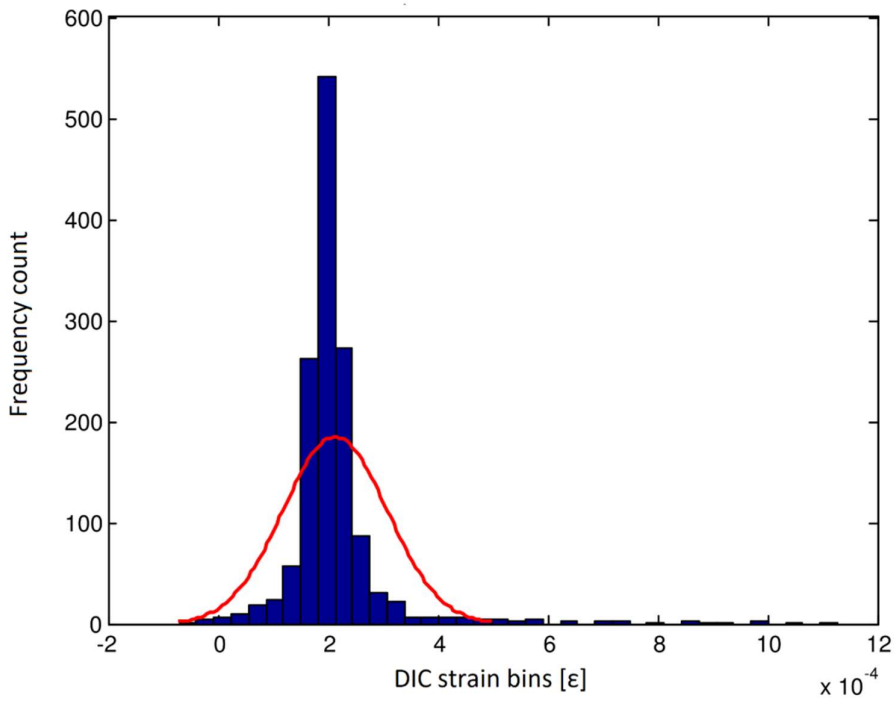

Figure 3.6-5 Histogram of first principal strains, the average of which was used to compare to the strain gauge readings

This averaging of the data is reasonable because of the homogeneous nature of the strain field. The average will be used as the reported value representing the DIC strain that the tensile specimen underwent at a given load step.

This value is used to compare against the strain gauge read-outs to obtain the strain error, and thus the DIC accuracy determined. The error is termed the absolute strain error because the magnitude of the value is taken to omit any confusion with negative values. The standard deviation is an indication of the precision of the measurement. A tighter spread about the mean would quantify a more precise measurement and vice-versa. These statistics were calculated for all the applied strains.

The methodology set out in this section establishes baseline DIC accuracy (i.e. strain error). This work sets the foundation upon which investigations on the effects of varying the major DIC parameters as well as the effects of temperature on accuracy can be undertaken - as required by Objectives 5 and 6.

3.7 Variation of subset-size and step-size

This section builds onto the previous. A methodology to investigate the influence of subset-size and step-size (the two major DIC parameters that can be user-chosen) on the DIC strain error is undertaken. This output addresses Objective 5.

Step-size is looked at first and a first-principles understanding of how strain is calculated is needed. The mechanics underpinning the effects of a change in step-size on the calculated strain is best described by a specific simplified example. Note that DaVis does not use the following equations (instead uses numerical differentiation of deformation vectors), but the analogy is accurate. Also, a single vector is used hereunder for illustrative purposes but the same concept will apply to each vector in a DIC field. Consider the two scenarios depicted schematically in Figure 3.7-1, where the same tensile specimen undergoes the same strain, but which is measured slightly differently.

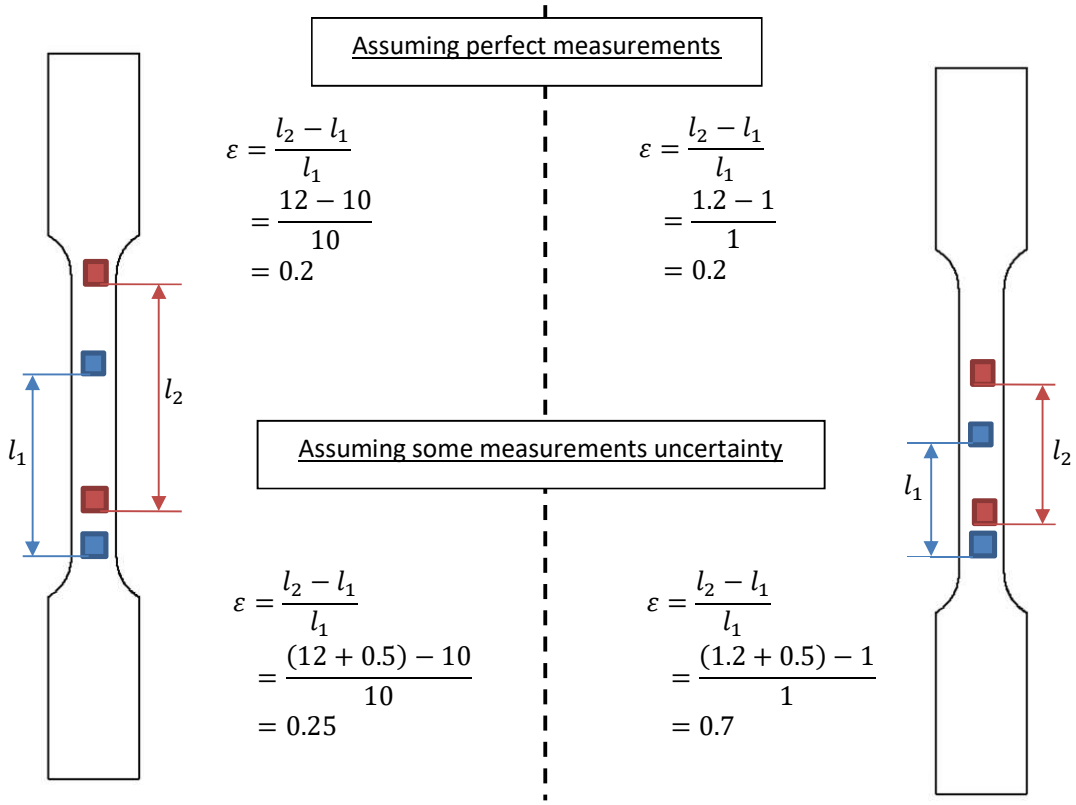

Figure 3.7-1 Example showing the effects of measurement uncertainty on strain calculations for two distinct step sizes.

On the left, the step-size (l_1) between otherwise identical subsets is much larger, than that on the right. Theoretically the strain is the same as is shown by calculating the strain of arbitrary values of l_1 and l_2 (the right had values made an order of magnitude smaller than those on the left). However, as an identical (arbitrary) amount of measurement uncertainty is introduced to both left and right scenarios, the error in the calculated strain *seems* to increase markedly for a smaller step-size. Note: uncertainty was only added to l_2 for the sake of simplicity, both l_1 and l_2 would have uncertainty. This is an artefact of the way strain is calculated and not of the DIC system itself. That is, the accuracy with which DIC tracks subsets has not changed, the accuracy of the measurements simply seems to improve (decrease) with larger step-sizes because of the nature of the underlying mathematics.

Notwithstanding the above, step-size was still included in the investigation to check for any unanticipated trends in the data. It was prudent at this stage to develop a sizing scheme that considered both the step-size and subset-size. Subset sizing was already developed and justified in section 3.5, and so this foundation was augmented onto. The challenge with a step-sizing scheme was that there exists a plethora of choices for any given subset-size. There also exists a maximum step-size recommended by DaVis for a given subset-size, which is ((subset-side-length)-1) ÷ 2. This latter constraint meant that if the maximum recommended step-size value for a larger subset-size was used as a constant, it may be outside of the recommended maximum bound when used for a smaller subset-size. This challenge was resolved by defining a variable step-size that is a fraction (proportion) of the subset-side-length. This ensured the use of the full range of step-sizes available for any given subset-size. The maximum recommended step-size was used as a starting point and then smaller factions applied, namely: one-third, one-fourth, and one-fifth of subset-side-length.

Therefore, for each subset-size, four step-sizes were calculated – of which the pixel values are shown below in Table 3.7-1, rounded off to the nearest convenient integer.

		Step-Size (fraction of subset side length)			
		1/5	1/4	1/3	Max. recommended
Subset-Size	255×255 pixels	51	64	85	127
	235×235 pixels	47	59	78	117
	223×223 pixels	45	56	74	111
	213×213 pixels	43	53	71	106
	199×199 pixels	40	50	66	99
	187×187 pixels	37	47	62	93
	173×173 pixels	35	43	58	86
	159×159 pixels	32	40	53	79
	141×141 pixels	28	35	47	70
	123×123 pixels	25	31	41	61
	99×99 pixels	20	25	33	49
	71×71 pixels	14	18	24	35
	31×31 pixels	6	8	10	15

Table 3.7-1 Pixel values for the various step-sizes considered for each subset-size.

Batch processing tools within DaVis were made use of to correlate the twenty-one images captured in the previous section using the 52 subset/step-size combinations seen above, and then processed in MATLAB as before. This yielded the strain errors as a function of step-size, subset-sizes, and applied strain.

To analyse the relationship between the variables, one was held constant and the other three plotted on three axes. This was executed in Excel for ease of use, structured such that the processed data from MATLAB could be copy-pasted into Excel and 3-axis plots automatically generated for all the data with a chosen variable held constant.

This aforementioned procedure was repeatedly undertaken to investigate the following:

- Determine the subset-size and step-size that would yield the lowest strain error, and quote what this lowest strain error is.
- Investigate whether the noise floor could be improved by taking multiple images at each strain step and averaging them together. This was implemented by capturing and averaging ten images at every applied strain step.
- It was of interest to investigate the variability in strain accuracy if the test was repeated at a different area of the same tensile specimen.
- Also, how does this compare to a different speckle pattern? The aerosol spray can will be used to apply the heat resistant paint for the thermal sensitivity tests. It was thus prudent to investigate the effect of changing the speckle pattern to that. The results from this piece will provide the baseline strain error to which the thermal sensitivity tests can be benchmarked. It will also determine whether comparisons can be drawn between the results in this section and that of the thermal sensitivity tests.

The strain errors determined in this section provided a measure of the performance of DIC in a laboratory setting, accounting for changes in step-size, subset-size and applied strain, thus addressing objective 5.

3.8 Spatial strain resolution

Larger subset-sizes result in lower strain errors (higher accuracy) - which is desirable. This was reported in the literature in this work as well as noted in the results of the preceding section (reported in the next chapter). However, large subset-sizes will smooth out higher strain gradients (Lecompte et al. 2006) that occur within them, and hence a trade-off is created. This warranted investigation into the trade-off between accuracy (strain error) and strain resolution in pursuit of further addressing objective 5.

A method for generating strain gradients that could be measured by DIC was needed and fracture mechanics was turned to for this. The strain gradients leading up to a crack tip in a material become very large as the crack propagates - with the exact solution becoming infinite (singularity) at the crack tip itself. This can be seen in Figure 3.8-1, where the stress (σ_{yy}) increases exponentially with reducing distance from the crack (r). This schematic however represents the stress in a single plane, where a two-dimensional stress field is in fact generated on the surface of the material through which the crack is propagating. A corresponding strain field can also be generated and is shown in Figure 3.8-2, where the warmest colours closest to the crack tip decay rapidly to cooler colours with increasing radial distance from the crack tip.

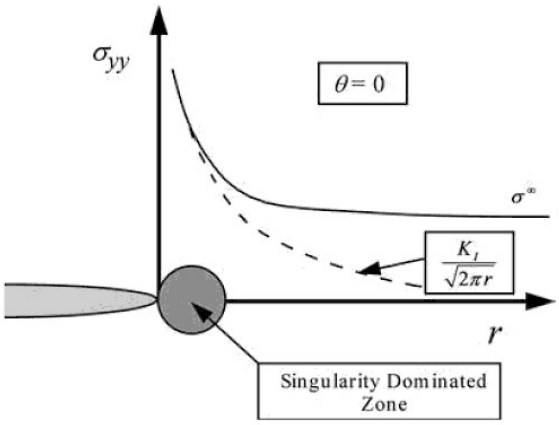

Figure 3.8-1 Stress as a function of distance from the crack front (Anderson 2005)

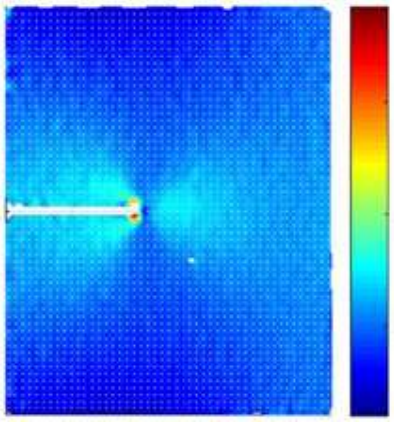

Figure 3.8-2 Strain field around the crack of a Mode I loaded elongated compact tension specimen (Huchzermeyer 2017)

As the crack is forced open and propagates further into the material, the field's gradient in the vicinity of the crack will become steeper as the stresses/strains increase in that region. The aforementioned stress field can be described analytically as discrete points on a polar co-ordinate system:

$$\sigma_{ij}(r,\theta) = \frac{K_I}{\sqrt{2\pi r}}[\widetilde{M}_{ij}^{(n)}(\theta)] \quad (1)$$

Where

- (r, θ) is the position on the polar plot being considered, centred at the crack tip.
- K_I=$A_1\sqrt{2\pi}$ is the stress intensity factor for Mode I loading.
- n is the number of terms that are to be used.
- $\widetilde{M}$ is a function defined for the principal direction.
- $i,j = \{1,2,3\}$ refer to the principal directions for the displacements around the crack tip.

Each incremental loading of the crack generates a unique analytical field with increasing gradients that can be compared to the fields generated with DIC images of the crack. The comparison thus offers insight into the performance of DIC measurements with differing strain gradients. The stress intensity factor K_I can be used as proxy quantification for the strain gradient, as larger K_I correlates to a stress/strain field with a steeper gradient leading up to the crack tip.

The data for such a crack was generated by (Huchzermeyer 2017) who measured mechanical properties using DIC, and this data was used in this work with permission. (Huchzermeyer 2017) used compact tension specimens made out of Perspex that had an aerosol spray can speckle patterns applied to them in the same manner that was used for the tensile specimens in section 3.1. The compact tension specimens were loaded in a tensile testing machine and imaged with the same LaVision equipment used in this work (albeit using a larger telecentric lens). The setup can be seen below in Figure 3.8-3.

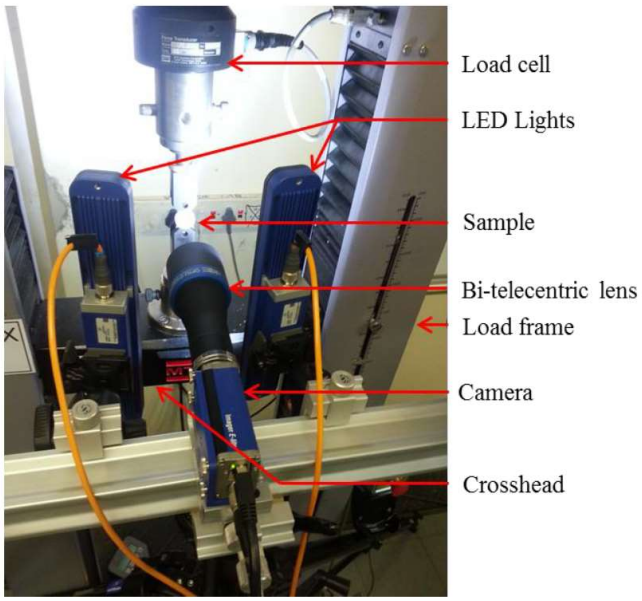

Figure 3.8-3 Setup used by (Huchzermeyer 2017) *to do DIC analysis of propagating cracks in compact tension specimens*

Of the data obtained, about every fifth image (from image 60 up until 111) was used since this work was not interested in the incipient cracking nor the final fracture. These were processed in DaVis, at all the subset-sizes and step-sizes chosen previously in Table 3.7-1. MATLAB code written by (Huchzermeyer 2017) output the analytical values that uniquely described the field. These data points were generated such that their location superimposed over the data generated by the DIC correlation process. This code was adapted to process the data for the 52 subset-size/step-size combinations used in this work. By comparing the strains in the analytical field to that generated by DIC, on a point-by-point basis, an error between any two corresponding points can be calculated. These errors can then be averaged for all the points considered in the fields, to yield a single representative value of error for any given K_I (which represents strain gradient). As the field develops through each increasing load step and strain gradients increase, the evolution of the error can be monitored.

It was found that very few data points would be generated when large subset-sizes and step-sizes were used because of the small pixel area of the region of interest ahead of the propagating crack tip. Too few data points compromise the statistical integrity of the results, and hence the step-size was ultimately minimised to one-fifth of the subset-size, and the largest subset-size was excluded from the final results. The results were plotted in a similar format as had been used in the preceding section, showing the relationship between error, subset-size and KI.

In a DIC strain measuring application, an accuracy surpassing a certain threshold is necessary. However, the trade-off between high accuracy and strain resolution is unclear. This section detailed a method to shed some light on this trade-off.

3.9 Thermal sensitivity tests

Of concern for the use of DIC for online measurements is the effect that the heated pipework may have on the accuracy. DIC is strongly dependant on the quality of the images acquired. A hot surface will heat up the air in its vicinity, changing its refractive index, and possibly affecting image quality.

The change in refractive index manifests itself optically as a heat haze, often observable above a road surface on a hot day. High energy pipework in a power plant operates at several hundred degrees and thus the possibility of heat haze and/or thermal radiation interfering with the image quality (and hence DIC measurements) is plausible. This section investigates the magnitude of the error introduced to DIC measurements by these phenomena. This information gives insight into whether power plant DIC measurements can be done online (while the power plant is running) or on outage (plant shut down and cooled for maintenance).

A heating rig (Figure 3.9-1) was designed to model the convection and radiation conditions expected at a section of power plant pipework known to be vulnerable to creep-strain damage. At Lethabo Power Station, there have been several creep-strain related replacements of pipework sections leading into the High-Pressure Turbines. The section of pipe, known as a Steam Penetration, is also representative of an area where DIC could potentially be used due to its accessibility. Eskom has previously installed capacitive strain gauges on this section of pipework at another station (Matimba) with the same turbine design.

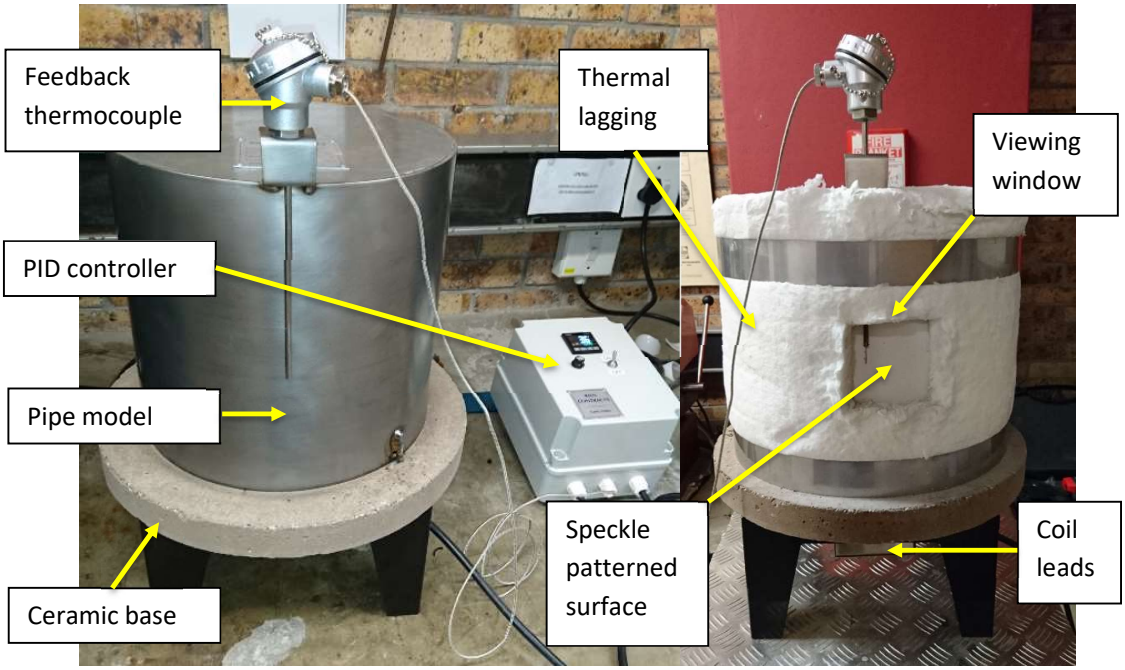

Figure 3.9-1 Left: heating rig without insulation, Right: insulation installed with access to pipe cut out (viewing window)

The temperature capabilities of the rig were chosen based on the Lethabo steam operating temperatures of 535 °C at full-load conditions. It was however thought prudent to have the capability of testing up to the temperatures of Eskom's later generation supercritical power plants (Medupi and Kusile) operating with live steam temperatures of 564 °C and reheat steam temperatures of 572 °C. It is to be noted that these temperatures are measures of the steam temperature and not of the pipework itself. The assumption was made that the surface temperature of the pipework is the same as the steam flowing through it. This is based on the fact that base load power plants, as coal plants within Eskom are usually designated, run at steady-state for extended periods. The heat from the steam would thus have sufficient time to soak through the pipe wall-

thickness to the surface. The insulating cladding and lagging would also assist in retarding the dissipation of heat from the surface to atmosphere, maintaining its temperature.

A 76 mm stepped ceramic base was cast, allowing a stainless-steel tube to sit around the step. Positioned in the centre of the tube is a brick pillar 230mm tall, outside dimensions +/- 200 mm², rounded on the 4 corners. The pillar was grooved to accept a Nichrome element rated at 12.5 A, 2.2 kW. On top of the pillar, a 70 mm ceramic fibre biscuit with outside dimensions to suit the inside diameter of the pipe was installed. The biscuit was bolted through the pillar to the cast base and in doing so, clamped the three components together. A rolled tube of 316 L stainless steel 4 mm plate was placed over the pillar assembly and bolted to the cast base. The element was terminated below the cast base into an electrical box. The base was elevated on a 200 mm high stand to allow space for the electrical terminations. A K-type thermocouple was fitted to the outside of the rolled tube. Both the element and thermocouple were terminated into a control panel, incorporating a separate PID controller, switched with a solid-state relay. The power circuit was connected to a 15 A circuit breaker for electrical protection. Insulating lagging was wrapped around the outer diameter as would be found on plant, and a window cut out where the camera was focussed on the pipe surface. The cut out was made 10 cm × 10 cm which is significantly larger than the 8.44 mm × 7.06 mm FOV that the telecentric lens yielded. This was done so as to mitigate interference from edge effects - the temperature of the pipework under the insulation would be at a higher temperature than the exposed pipework, creating a thermal gradient.

The speckle pattern within the viewing window was applied using Flameproof™ spray-can high temperature paint manufactured by VHT. This is the same paint alluded to in Section 3.1, and used for one of the candidate speckle patterns that was analysed. This was also done in an effort to minimise the speckle pattern differences between the data generated in the tensile specimen testing and this heating rig testing in order to facilitate comparisons between results where appropriate. This paint, designed for use in exhaust systems, is rated to withstand temperatures of 704 °C, and up to 1093 °C for shorter periods as per the Material Safety Data Sheet. The surface of the pipe was cleaned and roughened with 100 grit sandpaper to facilitate the adhesion of the paint to the surface and mitigate the cracking that was noted in some of the speckle patterns applied in section 3.1. The final speckle-patterned surface with the feedback thermocouple can be seen in Figure 3.9-2.

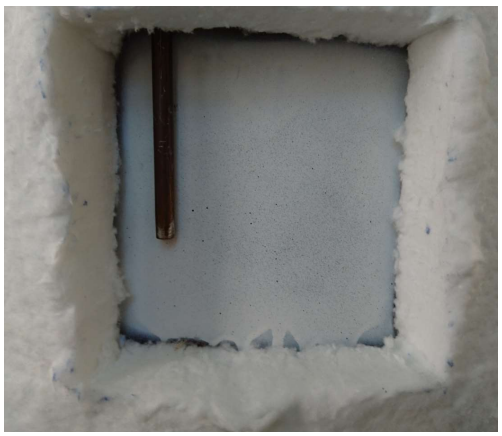

Figure 3.9-2 Speckle pattern applied within viewing window. The temperature controller feedback thermocouple can also be seen, positioned close to the testing area.

The focal length of the telecentric lens was only 62.2 mm, and this posed the risk of heat from the rig damaging the telecentric lens and camera. To mitigate this, a two-step approach was implemented. To reduce convective heat transferring excessive energy to the lens directly, a pane of heat resistant glass was placed between the heating rig and the camera. The glass was Robax; a product manufactured by Schott capable of withstanding temperatures of 680 °C. At its limits, it is specified as being capable of withstanding 760 °C for durations less than 100h. The additional advantage of using this glass pane was that a quasi-seal was created between it and the lagging insulation, isolating the pipe surface from air currents in the vicinity. This mitigated the effects of external breezes, which are difficult to account for, disrupting the pipe surface convective air flows and/or temperature.

The concern with protecting the camera in this manner was that errors may be introduced to the DIC optics. Glass will not transmit all of the light that goes through it, since some light will reflect off of the first surface that it enters, some will get absorbed in the glass itself, and then a second reflection will occur as the light hits the other side of the pane of glass before it exits. The transmission efficiency of Robax glass is shown below in Figure 3.9-3. The spectral range of the Imager E-lite 5M camera is specified as 400 nm to 850 nm which is somewhat to the lower transmission side of the glass but still well above 80 %.

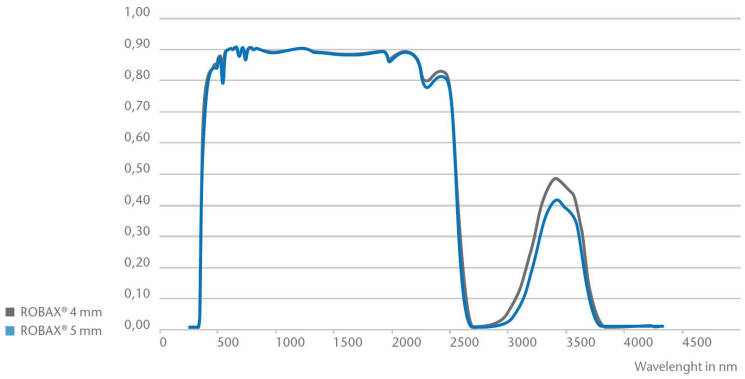

Figure 3.9-3 Light transmission percentage of ROBAX® glass

Damage from radiative heat transfer also needed to be mitigated. A rigid, tin foil wrapped camera cover was constructed such and placed over the camera lens between tests. This obviated the need to move the camera away while the heating rig transitioned to its next temperature increment, mitigating possible errors due to repositioning. The camera temperature was monitored for major excursions via the inbuilt function in the DaVis software.

Images of the surface were taken at several temperature increments, as per Table 3.9-1. They were captured when the heating rig was at steady state (rig allowed to expand fully), marginally above the temperature setpoint (when the PID controller de-energised the heating coil). The latter part was done so as to mitigate the risk of the powerful heating coils changing the rig's surface temperature too rapidly and inadvertently introducing expansion. At each temperature step, sixty images were taken in six bursts (ten images per burst). This was found to be a conservative period of time in which the heating coils were guaranteed to remain de-energised (as monitored from the controller). The ten images resulting from each burst were then averaged out to mitigate possible image sensor noise stemming from the electronics running at elevated temperatures.

Temperature [°C]
100
200
300
400
500
530
535
540
560
564
570
575

Table 3.9-1 Increments for the testing of DIC at temperature.

The DIC strains between the resulting six images at each temperature step were calculated using a subset-size of 255 × 255 pixels to maximise accuracy. High strain gradients are neither expected in this setup, nor desired to be resolved and so this large step-size (127 pixels) is justified. The average of the DIC strains calculated for each temperature step was then plotted. This average is theoretically zero since no expansion/contraction should be present during the capturing of the images, and thus deviation from zero strain is attributed to effects stemming from the surface thermal effects. The validation of zero actual strain from expansion/contraction is looked into later.

It can be seen in Table 3.9-1 that the temperature increments were reduced around 535 °C. This is the steam penetration pipework's (on which this heating rig was modelled) operating temperature. It was of interest to get more granular data around this temperature to monitor for any anomalies with regards to DIC strain measurements. In a power plant operating context, control of the operating temperature is done by way of PID control of several systems, inevitably resulting in minor temperature fluctuations and hence influences on potential DIC measurements. Finer increments were also used at Supercritical plant's (Medupi/Kusile) reheat and live steam temperatures.

As was alluded to, it was important to validate that the DIC strain measurements obtained were not in fact legitimate expansion/contraction of the heating rig. The rig was taken up to 585 °C and a sequence of 100 images taken at a rate of 5 images per second (i.e. period of 0.2 s). 100 images were sufficient to span the entire length of time that the coils were de-energised. 585 °C was chosen because maximum heat transfer rates (and thus expansion/contraction rates) would be observed at this maximum rig temperature relative to atmospheric temperature (Newton's law of cooling). Strains were then calculated for this image set and if there was expansion/contraction, a trend would be seen in the data as opposed to stochastic data if the calculated strains are attributed to the stochastic thermal effects of heat haze. To take this a step further, moving averages of the data were calculated in an effort to drawn out any underlying trends. A two, ten and twenty image moving average was calculated.

This section investigated the complexity that would be encountered if DIC were to be done online. The temperature of the surface will inevitably cause a heat haze as the refractive index of the air changes, and it is of import to quantify what effects this will have on the baseline DIC strain errors that were established earlier under ideal laboratory conditions at room temperature.

4 Results and Discussion

This chapter presents the results recorded from the experimentation. To facilitate reading of this work, the discussion of these results is done simultaneously and are ultimately tied to the objectives. The layout is shown below and follows that of the previous chapter closely. It is divided into three broad segments. Firstly, an image analysis of the speckle patterns is performed, upon which images that can be used in the subsequent work are identified. Secondly, the achievable strain accuracy of DIC is delved into, investigating the effects of various aspects and parameters. Finally, the effects of measuring pipework at temperature are quantified and recommendations made on the applicability of DIC for online use.

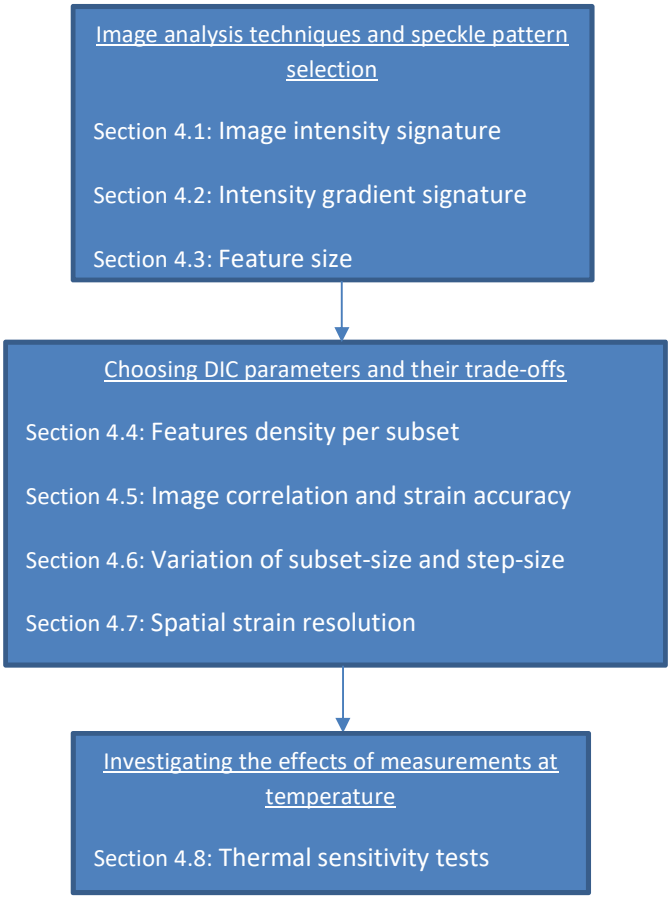

4.1 Image intensity signature

Starting on the qualitative front, the eight candidate speckle patterns (Figure 4.1-1 and Figure 4.1-2) are visually seen to follow the recommendations set out in literature, namely:

1. They do not have a preferential direction - they are isotropic.
2. No repeating pattern is noticeable, and where the features are discernible from each other, they are noted to be random and unique. They are stochastic and homogeneous.
3. There is a high contrast between the light and dark regions for the most part.

Note that there is no magnification of images, and this is the case for the rest of the work. Each of these speckle patterns considered were compliant with the recommendations to differing degrees, which facilitates the testing of the sensitivity of the characterisation techniques that follow.

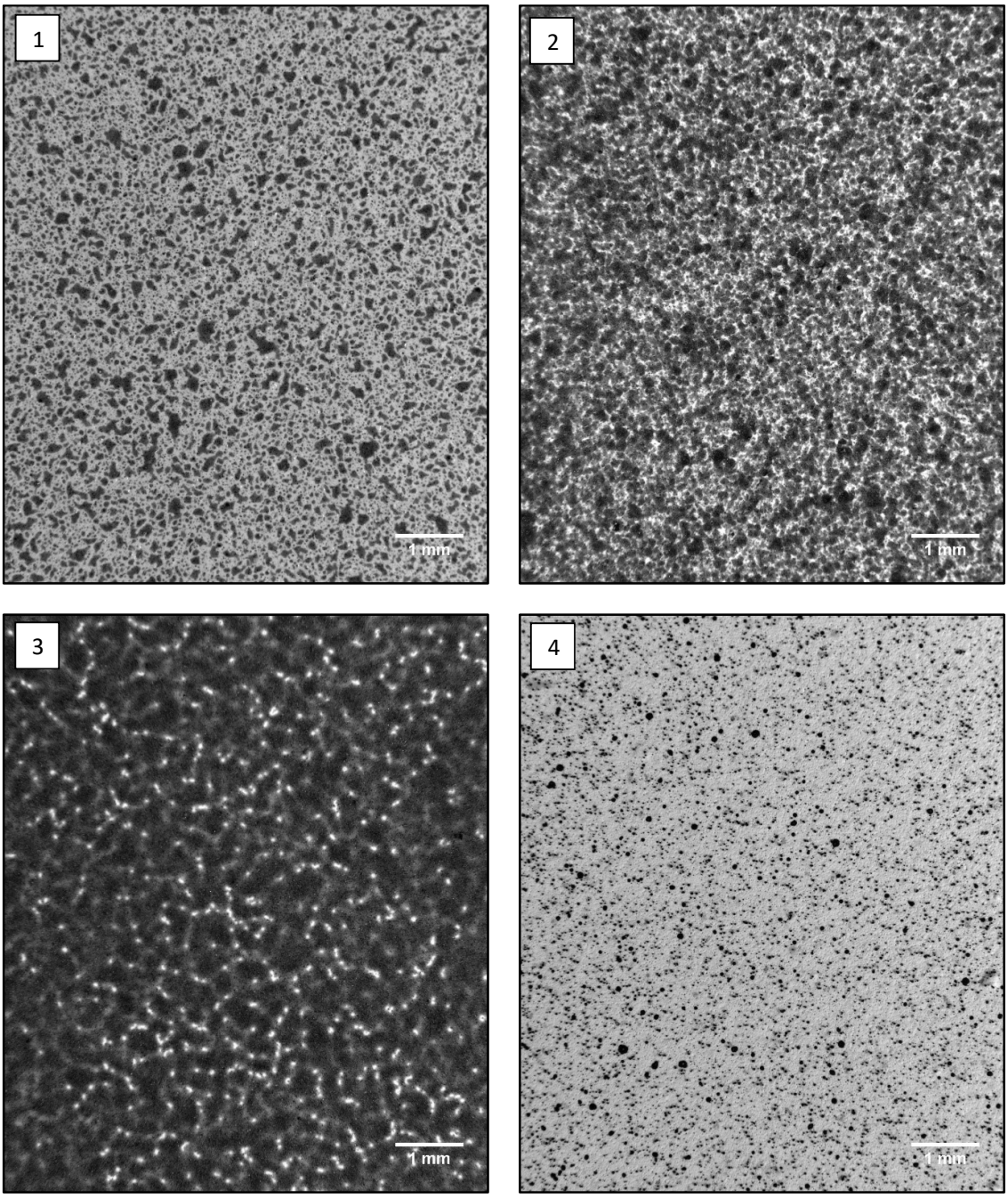

Figure 4.1-1 the first four of the speckle patterns chosen for analysis. Their application method and bit depth were as follows: (1) Airbrush 12 bit (2) Airbrush 12 bit (3) Airbrush 12 bit (4) Spray-can 12 bit. Normal magnification.

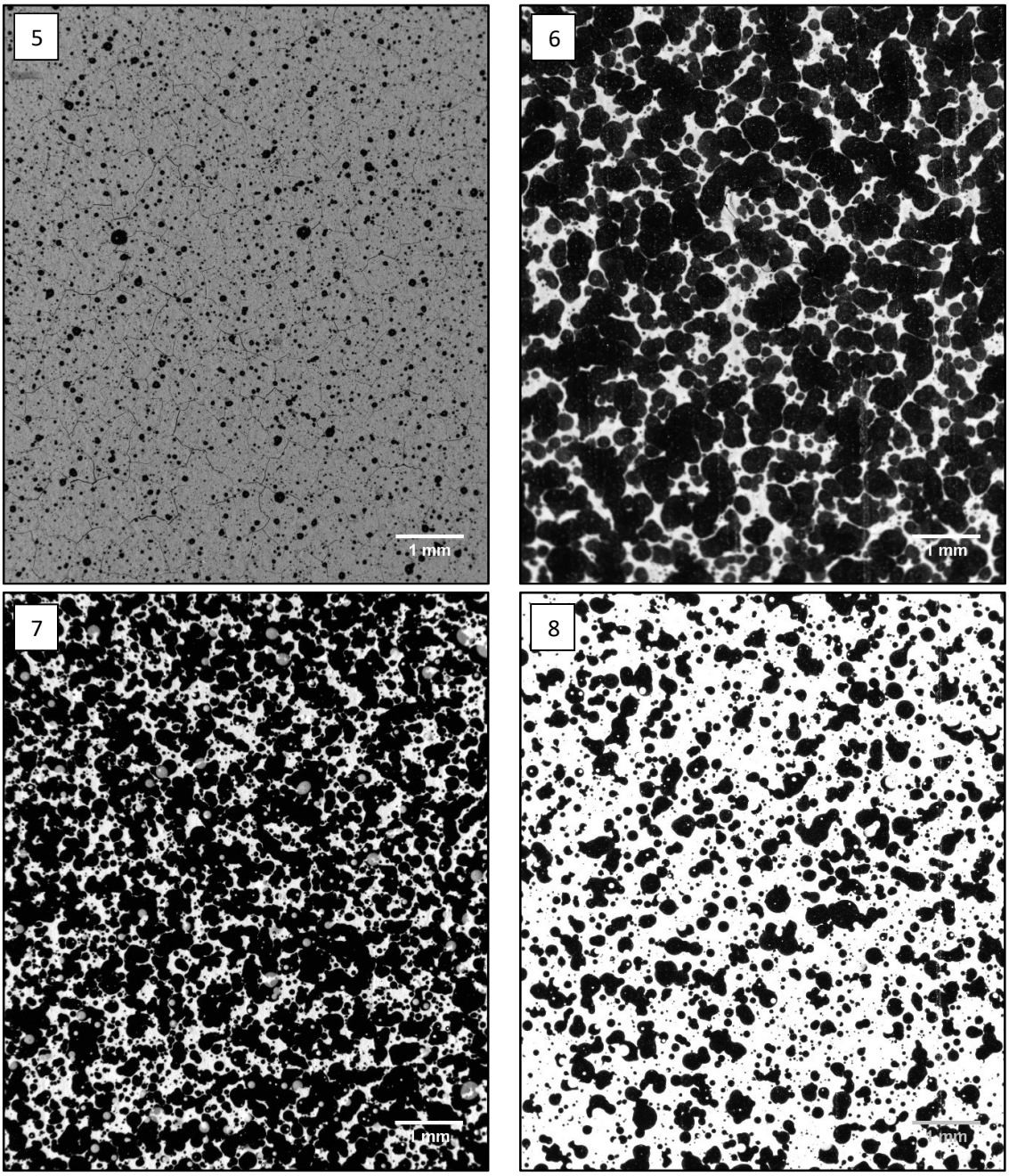

Figure 4.1-2 the remaining four out of the eight speckle patterns chosen for analysis. Their application method and bit depth were as follows: (5) Spray-can 12-bit (6) Spray-can 12-bit (7) Spray-can 8-bit (8) Spray-can 8-bit.

The image intensity is the first attribute that will be examined. This tool will give assurance of the quality of the image as well as give a characterisation of the speckle patterns.

Shown in Figure 4.1-3 are the resulting intensity histograms, numerically corresponding to the images of the aforementioned eight speckle patterns. Looking first at the image of speckle pattern (SP) 1, created using an airbrush and setting the image sensor to a bit depth of 12 bits, the distinction between black speckles and the white background is visually easily identifiable. It is observed that there is a larger proportion of white background relative to the dark features. This is

echoed in the corresponding histogram where a large peak of higher intensities is noted, i.e. there exists a large population of brighter pixels (white background) within the image. The darkest of the pixels register an intensity of 200 (on a range of 0-4095 given the 12-bit resolution), indicating that the lighting, aperture, ISO and exposure settings facilitate an adequate signal from all the pixels. The range of the distribution is calculated to exploit 95% of the camera sensor's capabilities, maximising its use. Also observed in the histogram is that negligibly few pixels are registered on the brightest end of the range. This means that there are few saturated pixels that may bleed electrons into their neighbours (introduce noise) and which are incapable of registering possible brighter data (potential loss of information). The total pixel count (5 054 448) ascertained from the histogram count also validates the sensor's pixel count specification of 2058×2456 pixels. All these aforementioned observations collectively contribute to the morphology of the histogram which thus characterises this image, encompassing its SP and parameters that influence its brightness. Considering all of the above, lighting and camera setup were deemed adequate, assuring image quality and conveniently providing initial speckle pattern characterisation, which supports Objectives 3b and 3c.

SP2 was also applied with an airbrush, but several more speckle coats were applied. Visually, this is perceived as a denser SP with the distinction between background and features less pronounced than that of SP1. A notable difference is also seen in its histogram distribution, where the morphology is observed to be more unimodal than that of SP1. This morphological difference suggests that visual differences in the SPs (and system settings) can be adequately perceived by the said histograms and more evidence of this will be seen in subsequent SPs. SP2 also uses a larger range of the image sensor's bit depth, starting at a darker value of 150. However, the pixels are noted to have saturated at the bright end, as is evidenced by the column of data in the histogram at the 4095 intensity bin. It is to be noted that this could have been corrected for in the setup (as has been done in other speckle patterns in this set) but has been left as such to test the capabilities of these characterising tools. Lighting, aperture, ISO, and/or exposure would therefore need to be adjusted to regain the cut-off high intensity data if this setup were to be used in final testing. The over-saturated pixels also run the risk of bleeding electrons into their neighbours, introducing noise into the data. This SP with its current setting was therefore not used and is included here (as with some of the other SPs) to demonstrate the utility of the analysis tools in support of Objective 3.

SP3 was also airbrushed, using similar lighting, but with sufficient paint coats applied so as to make individual features in the SP indiscernible. The histogram response is noted to have distribution morphology closer to that of SP2 than of SP1 (but still notably different), echoing the progressive change in the three speckle patterns. It is observed that SP3's distribution is not only unimodal but also narrower, and is shifted to the darker end of the intensity range. This is reasonable considering the greater proportion of dark speckles (and hence dark pixels) from the denser speckle pattern.

In SP4, the SP application method changed to aerosol spray can. Visually, the features are noted to be more uniformly circular and more sparsely distributed than the preceding airbrushed specimens. This is congruent with the larger proportion of brighter pixel data noted in the histogram. From this histogram, SP4 is observed to be more similar to SP1 than to SP2 or SP3 in terms of background-to-feature proportions. The distribution is unimodal and shifted to the right (again more similar to SP1) with a marginally larger range of intensities than has been seen in preceding SPs.

The image shown in this work for SP5 has been contrast adjusted so that the features are clear to the reader. However, as can be inferred from the left shifted intensity range of the histogram (note the maximum on the scale of 3191), this image was relatively dark.

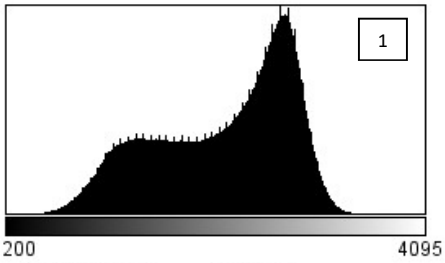

Count: 5054448 Min: 200
Mean: 2220.048 Max: 4095
StdDev: 631.744 Mode: 2776 (73372)
Bins: 256 Bin Width: 15.215

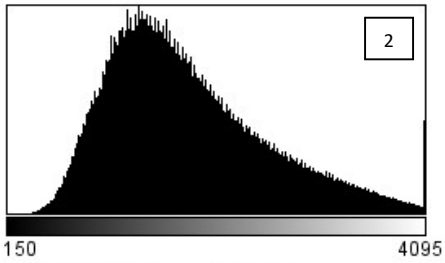

Count: 5054448 Min: 150
Mean: 1854.974 Max: 4095
StdDev: 746.663 Mode: 4095 (52138)
Bins: 256 Bin Width: 15.410

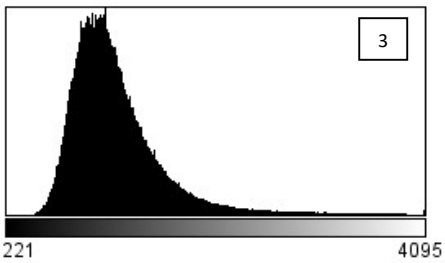

Count: 5054448 Min: 221
Mean: 1263.543 Max: 4095
StdDev: 496.516 Mode: 964 (104217)
Bins: 256 Bin Width: 15.133

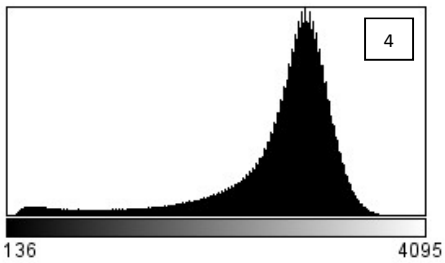

Count: 5054448 Min: 136
Mean: 2700.611 Max: 4095
StdDev: 616.187 Mode: 2956 (115911)
Bins: 256 Bin Width: 15.465

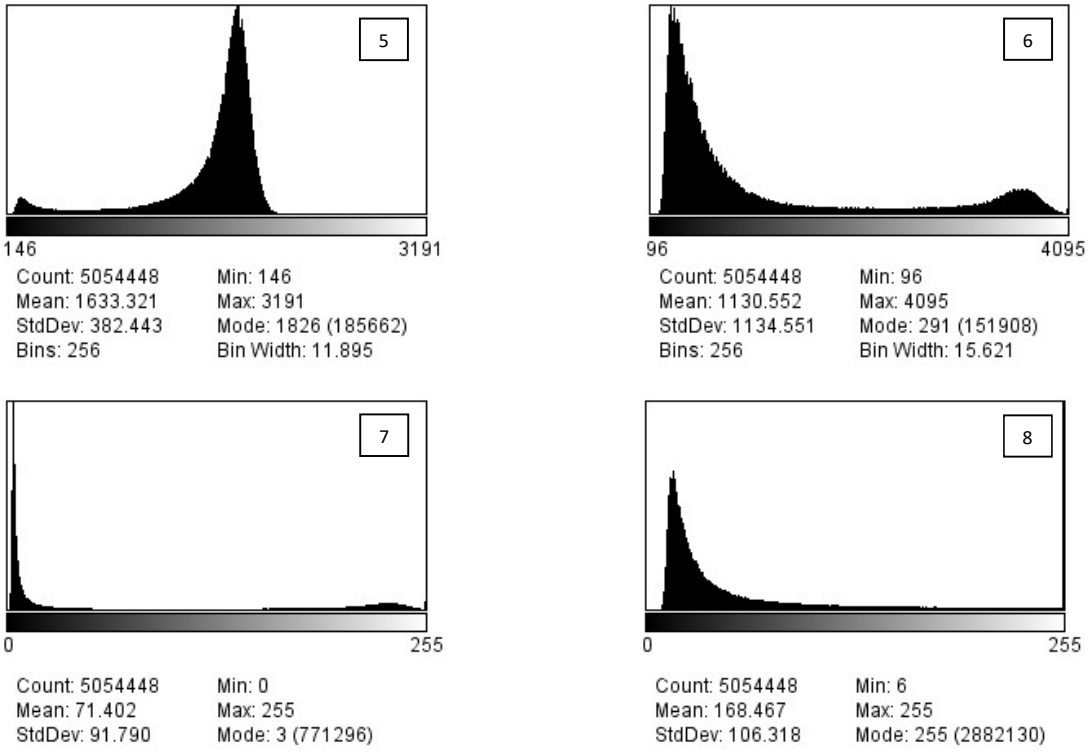

Figure 4.1-3 Histograms of the pixel intensity distributions for the eight speckle patterns investigated.

Adjustments to the system parameters would be needed so as to maximise/optimise the useable intensity range of the image sensor, generating richer and more granular data. This SP image is the antithesis of SP2 in terms of brightness of the pixel data. The feature's shapes and population size look similar to that observed in SP4, reflected in the similar morphology of the distribution for SP4 and 5. Fine cracks are visible in SP5 which are not evident in the other SPs, likely from non-ideal adhesion of the paint to the substrate, and likely to spall over time. This underscores the importance of careful application and quality control of SPs, substantiating the importance of quality control outlined in Objective 3.

SP6 was also applied with an aerosol spray can but at a much shorter stand-off distance from the substrate surface, which resulted in features that visibly appear larger relative to SP5. As per the intensity range of its corresponding histogram, lighting conditions were returned to an optimal setting to maximise the use of the image sensor without significant saturation at either end of the intensity spectrum. However, as with SP3, a greater proportion of the sensor's area was covered with the dark features and is echoed in the histogram's data concentrating at the darker end of the intensity spectrum. The histogram morphology is seen to almost be mirrored about a vertical axis relative to SP5, showing the extreme differences in relative proportions of bright and dark pixels (i.e. feature density) between the two. These above observations again demonstrate the histogram's good response to differing SPs and parameter settings.

SP7 and 8 investigated the effects of using a lower bit depth (8 bit). These two SPs differed significantly from each other in terms of feature density, but the feature size and morphology are noted to be similar. The histograms respond with distribution morphology not too dissimilar to those

seen in preceding SPs, but obviously spread over a smaller range (0-255). This setting therefore yields a lower resolution of data for the correlation algorithm to uniquely identify subsets and track their movement, even though pixel count remains unchanged (5054448 pixels) from the preceding SP images. The predominantly dark SP7 image is ascertained to be on the dark end of the histogram spectrum (15% of the available pixels registering at an intensity of 3), and is contrasted with SP8 which is heavily saturated on the bright side (57% of the available pixels registering at 255). This again underscores the use of intensity histograms as a quality control and the importance of adjusting parameters to optimally use the capabilities of the image sensor, not exceeding its limitations. The ZNSSD correlation algorithm used by DaVis is capable of accounting for offsets in intensity values to a degree; it cannot however compensate for loss of information if the sensor is saturated at either end of its light sensing capabilities.

This section showed that intensity histograms can be used as one of the constituent attributes used in characterising a SP. The qualitative differences in the distributions show that the technique is sensitive to different speckle patterns taken under different conditions. It is not claimed that, solely, this signature can uniquely characterise a SP, as changes in ambient lighting and other parameters mentioned will have an effect on the intensity histogram. However, this is one constituent characterisation, which will be complimented with the other attributes that are detailed in subsequent sections. On the quality front, it was shown that the intensity histograms give assurance that the hardware is functioning correctly and the setup is optimised. It is a tool that gives immediate feedback to the user on the quality of the captured image, which is crucial for subsequent DIC processing and analysis. These above observations speak to Objective 3 of this work.

In the next section, this characterisation framework is taken a step further where the intensity gradient is looked at.

4.2 Intensity gradient signature

Progressing with the characterisation, which addresses Objective 3, the intensity gradient signatures are looked at next. The intensity gradient distributions for the eight SP images are shown below in Figure 4.2-1. The distributions are all seen to have the same morphology, showing a right-tailed skewness which is describable by standard statistical measures, that in turn facilitates quantitative comparison between the SP images. This morphology is as a result of the nature of the software process that the images were subjected to, and thus all results will have the same morphology. These intensity gradient signatures therefore give a more quantitative approach to the characterisation than that observed in the intensity histograms of section 4.1. The median, as opposed to other measures of central tendency, is unaffected by the skewed nature of the distributions, and a summary of the speckle pattern medians is shown in Table 4.2-1

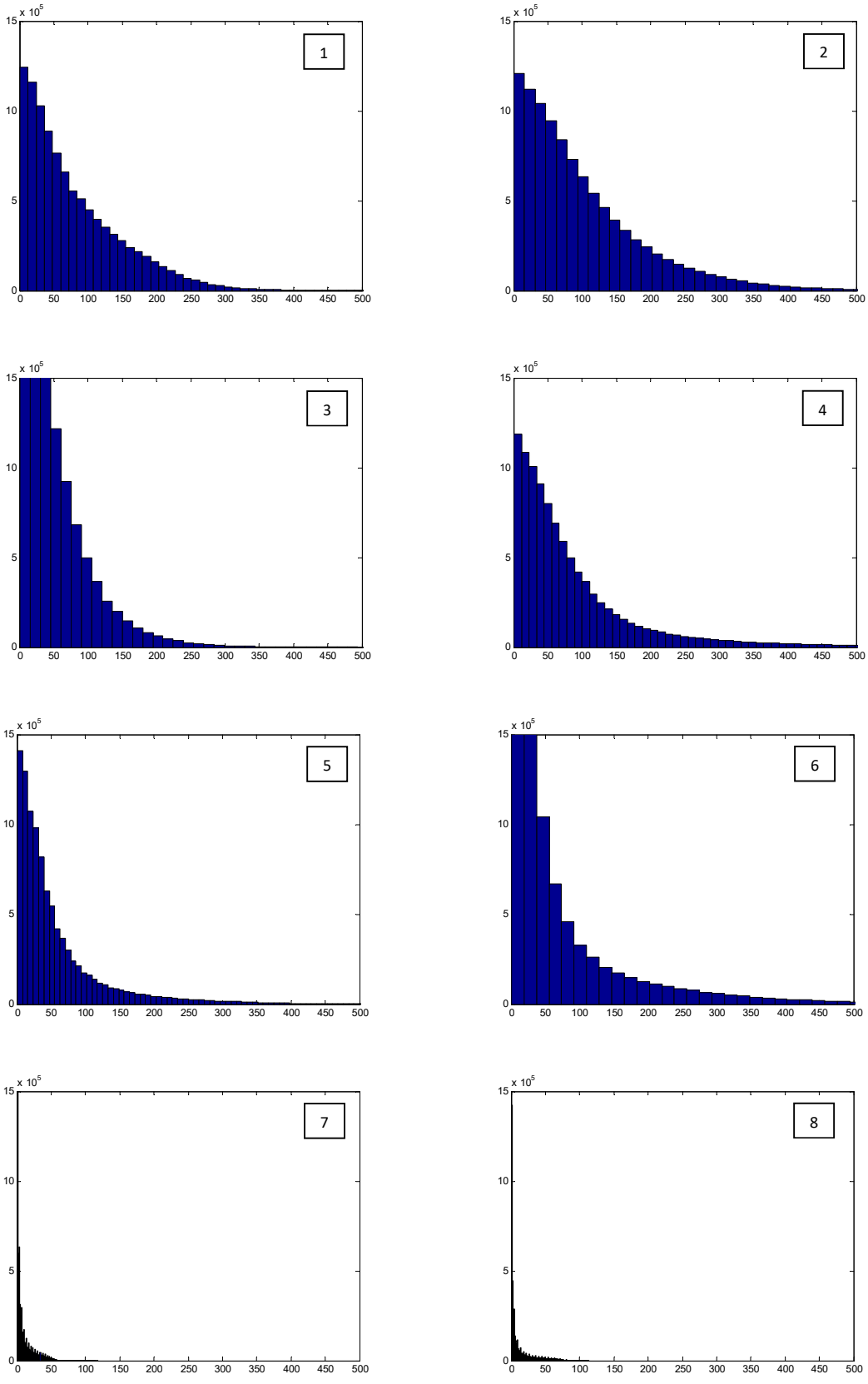

Figure 4.2-1 Intensity gradient distributions for the eight speckle patterns analysed.

Speckle #	1	2	3	4	5	6	7	8
Median intensity value	59,5	76,0	42,0	56,5	34,0	28,5	2,0	3,5

Table 4.2-1 Summary of intensity gradient histogram statistics for the eight chosen speckle patterns

A larger median intensity gradient indicates a steeper change from the lighter background to the darker features. This steeper change is indicative of the SP features having better sharpness and/or higher contrast, the latter which reduces correlation error (Reu et al. 2009). The range of the data in Table 4.2-1 spans from 2 to 76. To put this into context, a value of around 2000 would be expected for a very sharp computer-generated speckle transitioning from a white background to a black speckle, as was elaborated on in the Experimental Methodology.

The images with the top three steepest gradients, in decreasing order, are SP2, SP1 and SP4, with values of 76.0, 59.5 and 56.5 respectively. Referring back to Figure 4.1-1, SP1 and SP4 are noted to be visually similar in terms of feature sharpness and contrast, and this is reflected in their similar intensity gradient median signatures. SP1 and SP4 are again seen to be good candidates for further use in this work. SP7 and SP8 were the worst performers, calculating to 2.0 and 3.5 respectively.

This section showed that the median intensity medians have an appreciable response to the eight different SP images analysed. Using this fingerprint in conjunction with the intensity histograms progressively contributes to the accuracy with which a given speckle pattern can be described and characterised. This analysis tool also gives an indication of how well a correlation algorithm will track the features, with a higher contrast/sharpness being desirable. Additionally, any other analysis that makes use of image intensity gradient as one of its building blocks will benefit from using this tool as an initial quality check. These aforementioned virtues of the tool support Objective 3. This cumulative improvement in characterising precision will next be taken further with the analysis of feature size.

4.3 Feature size

The results of the median feature size within the eight candidate SPs are discussed in this section. Table 4.3-1 shows this data and also incorporates a summary of the data looked at in the previous two sections for convenience.

The feature size is noted to range from 55 pixels to 152 pixels. This is notably larger than the feature size factor of 3-5 times the size of a pixel suggested by (Lionello and Cristofolini 2014), or the characteristic sampling length between 3 and 6 pixels suggested by (Sutton, Orteu, and Schreier 2009). The features in the all the SPs are oversampled. It proved impractical to apply smaller features by using the airbrush or aerosol spray can – the limits of these application techniques had been reached. Optically zooming-out was not an option either since telecentric lenses with this functionality are not readily available. Increasing the stand-off distance was also not feasible because of the narrow depth of field of telecentric lenses (6 mm for the lens used in this work). A sensor with fewer pixels (lower resolution) could have been acquired, however sensors are generally manufactured in standard sizes and adjusting the pixels-per-feature parameter for different speckle patterns by swopping-out image sensors was deemed impractical. It was therefore decided that the oversampling was acceptable (and more preferable than under-sampling), with the inherent trade-off of having to use larger subsets to capture several features within it. Also, subset-size and its relation to accuracy were looked at in depth in sections to follow, and so the implications of this trade-off were adequately quantified.

Speckle Pattern #	Qualitative assessment	Intensity histogram morphology	Median intensity gradient	Median feature size [# of pixels]
1	Acceptable	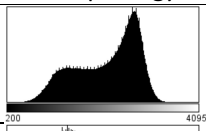	59,5	94
2	Acceptable	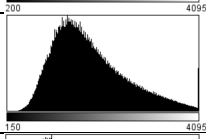	76,0	NA
3	Acceptable	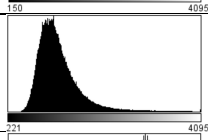	42,0	NA
4	Acceptable	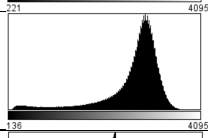	56,5	79
5	Acceptable	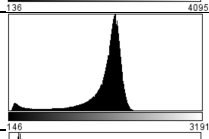	34,0	58
6	Acceptable	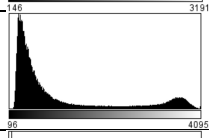	28,5	55
7	Acceptable	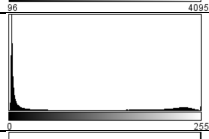	2,0	131
8	Acceptable	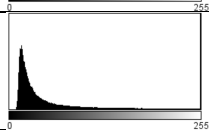	3,5	152

Table 4.3-1 Summary of quantitative attributes for the eight speckle patterns investigated

SP2 and 3 are not suitable to have their feature sizes digitally extracted, as a visual check of the indistinguishable features in Figure 4.1-1 will confirm. This highlights the importance of quality control of the speckle patterns after application and prior to imaging. SP1 and SP4 are visually seen to have features of roughly similar sizes (SP1 marginally larger than SP4), and this is echoed in the similar median feature sizes of 94 pixels and 79 pixels respectively. The same can be said of SP7 and SP8, who have significantly different feature densities but similar feature sizes, with SP8 showing slightly larger features (152 pixels) than SP7 (131 pixels).

Looking only at Table 4.3-1, SP5 and SP6 would imply almost identical feature sizes, yet inspection of the speckle patterns themselves (Figure 4.1-2) reveals this to be very incorrect. The SP5 image is observed to have features smaller than SP4, and this is reflected in the median feature size – 58 pixels and 79 pixels respectively. However, the clumped-up features of SP6 make distinguishing them difficult by eye and thus more so by software, leading to bogus results. This again underscores the limitations of software analysis and the importance of visual quality control and initial scrutinising of the speckle patterns before further processing.

From this data, SP1 and SP4 were deemed suitable for use in this work. SP1 was predominantly used in the next several sections and SP4 with its high temperature paint used for the DIC thermal sensitivity tests. Qualitatively they comply with recommendations made by literature. They are isotropic without a preferential direction; they are both stochastic and homogeneous, with no noticeable repeating pattern; and the features are random, unique and clearly discernible from each other. The white background is distinguishable from the dark features, adhering to the recommendation of high contrast. Subsequent to ensuring correct exposure by way of monitoring the extremes of the intensity histograms, the distribution for these two speckle patterns is seen to make use of a large portion of the sensor's range, maximising data for the correlation algorithm. The feature sizes were larger than that recommended by literature but argued to be acceptable when considering the practicalities of obtaining lower sampling per speckle. This therefore satisfies Objective 3, assuring that the speckle pattern for the most part adheres to what research recommends; assuring that the imaging system is set up correctly; and generating a unique fingerprint of the speckle pattern.

4.4 Features density per subset

The features-per-subset parameter has direct implications on the availability of data in each subset for the correlation algorithm to track. It is of interest to quantify this parameter to investigate the link between it and the DIC strain accuracy for different subset sizes detailed in Section 4.6.

First, for interest, the variability in feature density per subset is looked at in order to establish what kind of consistency between speckle-patterned specimens can be expected. The average number of features for the ten speckle-patterned specimens (the ones that were individually imaged as per the experimental procedure) is summarised in Table 4.4-1. The standard deviation for this data is noted to be small (2 features), indicating consistency between speckle-patterned specimens. This is desirable, reducing the sources of variability if acquiring DIC measurements from different samples. Also, the speckle pattern application technique ultimately used in a power plant context is likely to be more sophisticated than the simple airbrush technique used here, and thus consistency between speckle patterns applied to different components is likely to be more consistent than that noted in this data. The feature size is also included in Table 4.4-1, and averaging this data results in a feature size of 71 pixels. SP1 was observed to have a feature size of 94 pixels which is somewhat outside of a single standard deviation of this data but well within the data's range.

Specimen	Average # of features	Median feature size [pixels]
1	29	52
2	29	63
3	24	103
4	29	53
5	28	63
6	28	73
7	28	60
8	27	57
9	29	96
10	26	87

Average	28	71
Std. Dev.	2	18

Table 4.4-1 Summary of the characteristic parameters for the ten specimens

Next, the influence of subset size is examined. Figure 4.4-1 below shows the average number of features that fit within a subset versus the size of the subset in terms of pixel area (e.g. subset-size of 31 pixel × 31 pixel = 961 pixel^2). It is observed that an increase in subset area linearly correlates to more features within it. This is intuitive since a bigger subset will encompass more features. The significance is that a bigger subset will have more information with which to perform the correlation process. This will increase the accuracy with which the deformation of the substrate can be mapped, and ultimately the accuracy of the DIC strain measurements.

Of note is that the standard deviation also increases as subset size increase, as is seen by the error bars. This is attributed to the larger number of combinations and permutations of feature arrangements that become possible as the subset size increases. The implication, in terms of DIC, is that the accuracy with which a given subset can be tracked will vary to that of another subset because the information contained in the said subsets varies – and this scenario is exacerbated as the subset size increases. There are of course many subsets in a DIC measurement and a statistical measure needs to be used to ensure the bulk of the subsets are well correlated. This was checked in this work by monitoring the correlation coefficients, as will be shown in section 4.5.

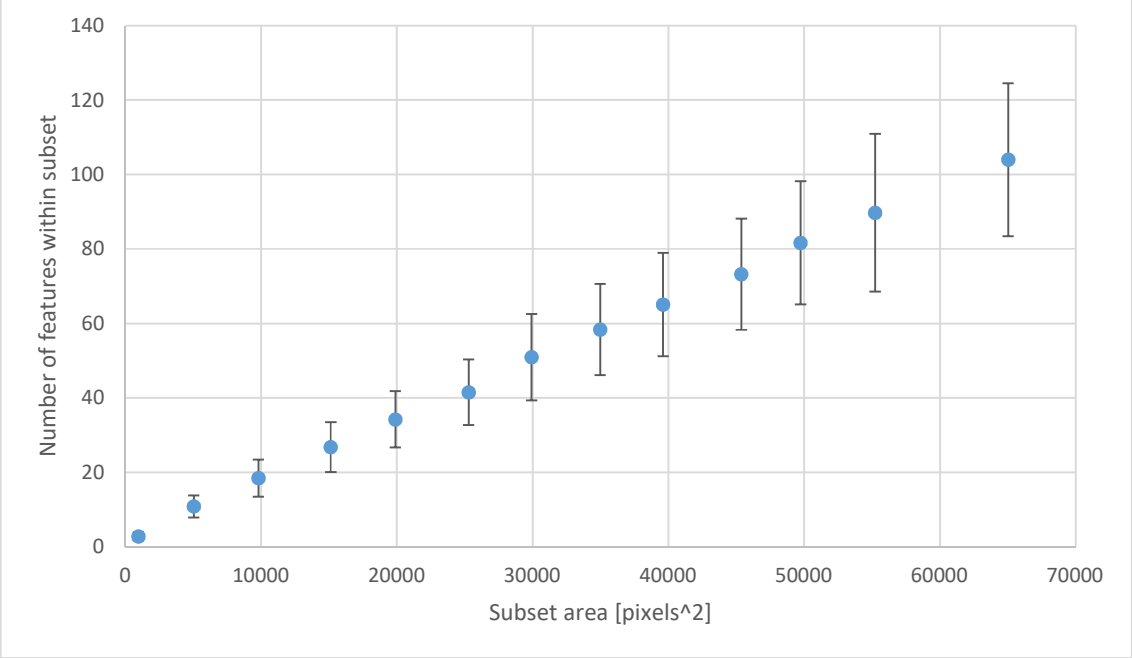

Figure 4.4-1 Number of features within a subset versus the pixel area of that subset. Error bars represent standard deviation of the data.

In this section it was shown that the features-per-subset parameter can be used as an additional characterisation of the speckle pattern. It was noted that there was good consistency between the specimens speckle-patterned with the same technique. The quantity of features was seen to increase as the subset-size increases, offering more information for the correlation algorithm to

work with. The data in this section supports Objective 3 and quantifies some fundamental DIC mechanics from which to understand the results obtained in section 4.6, where the effects of varying subset-size on DIC accuracy are explored.

4.5 Image correlation and strain accuracy

This section delves into ascertaining the accuracy that can be achieved with DIC in a laboratory setting using the baseline DIC parameters set out in the Experimental Methodology, and these are compared with literature. This forms the foundation for the work that is broadened upon in Section 4.6.

Figure 4.5-1 plots the average correlation coefficient values for the individual target images (i.e. images capturing the applied strain up to 200 με) for SP1. To reiterate, this data was captured using the chosen baseline parameters of a 121×121 pixels for the subset-size and a step-size of 60 pixels, and image 0 was used as the reference image. It is observed that average correlation coefficient trends downward with greater applied strain. This is due to the subsets becoming less recognisable to the correlation algorithm as they become more deformed. Put alternatively, the reference and target subsets are at their least similar when the tensile specimen (and hence speckle pattern) is at its most deformed, thus hindering the correlation algorithms ability to recognise them. Notwithstanding this, the quality of the correlation throughout the applied strain range is good, with all the correlations being well over 0.95. This quality check confirms that the data is suitable for further processing, addressing to Objective 3.

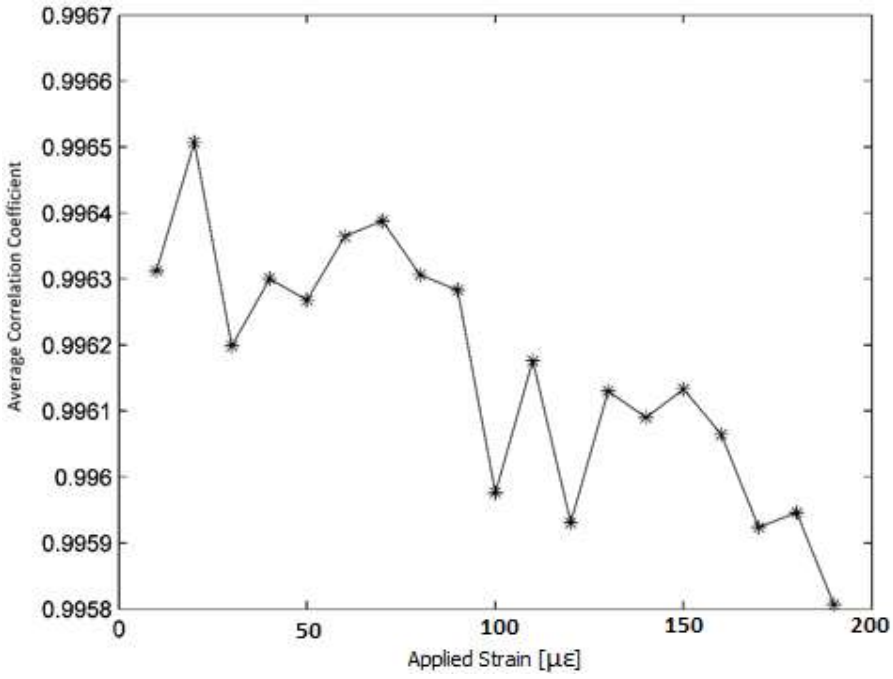

Figure 4.5-1 Average correlation coefficient calculated for each target image

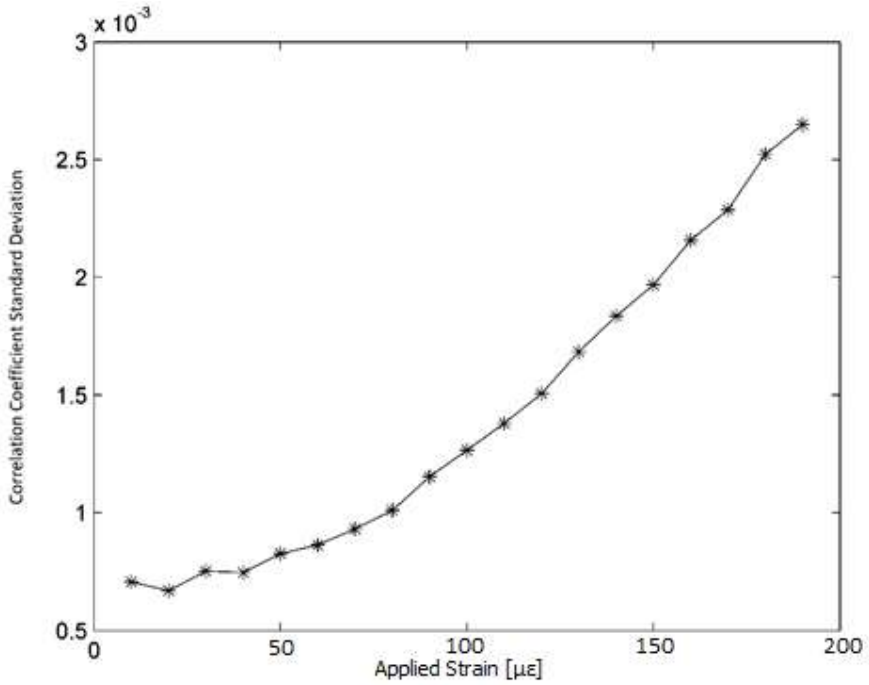

Figure 4.5-2 Standard deviation of the correlation coefficients calculated for each target image

Standard deviation is affected by the same mechanism stated above. The greater the deformation of the specimen, the less certainty that the correlation algorithm has about the final position of the target subset, leading to greater variability – i.e. standard deviation. This is reflected by the increasing trend depicted in Figure 4.5-2 for the same image set seen in Figure 4.5-1. The ramifications of the aforementioned decrease in average correlation coefficient (and increase in its standard deviation) on the DIC accuracy are elaborated upon in the discussion around Figure 4.5-4.

The error between the strain gauge and the DIC strain is subsequently studied. Figure 4.5-3 shows the strain readings for the strain gauge superimposed with that calculated by DIC (averaged) for the entire range of applied strains. Linear trend lines are added to the data and are observed to be in close agreement. This is quantified further by calculating the absolute difference between these two data sets at each applied strain and superimposing these results in Figure 4.5-3 as well. For more clarity, this resulting data set is zoomed into in Figure 4.5-4. In this latter figure, some noise in the data is evident and expected as this experimentation is testing the limits of the capabilities of DIC. The largest strain error is seen to be 14 με, with a subtle upward trend, notable in the calculated linear trendline, as applied strain increases. This trend speaks to the decrease in average correlation coefficient and increase in standard deviation noted in Figure 4.5-1 and Figure 4.5-2 respectively. To elaborate, as the correlation coefficients and standard deviations deteriorate, the strain error will tend to increase as the correlation algorithm's ability to accurately track (increasingly deformed) subsets deteriorates. From this initial data, it can tentatively be said that the DIC strain accuracy with respect to the strain gauge is well under 20 με for the given system.

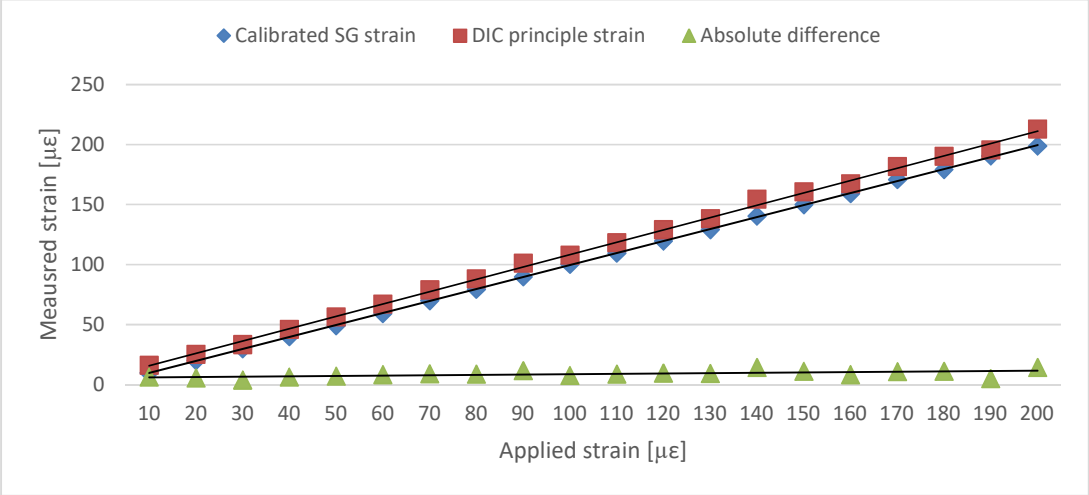

Figure 4.5-3 Absolute difference between SG readings and DIC principal strain

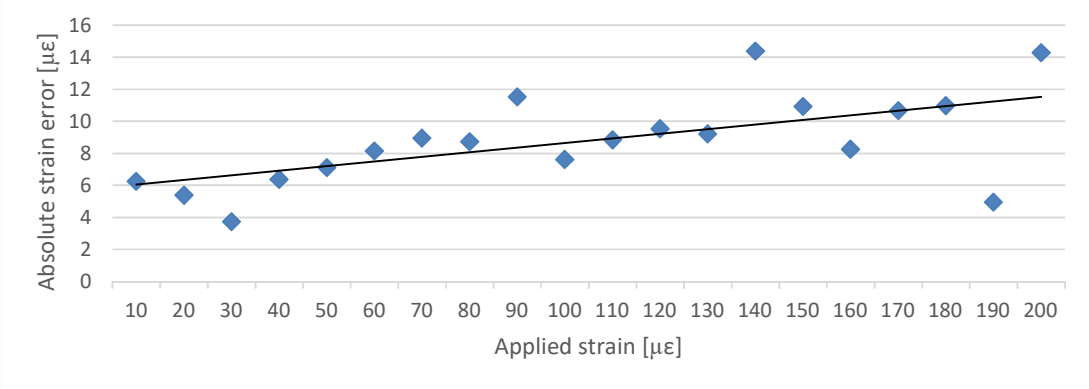

Figure 4.5-4 Zoom in on absolute difference

This aforementioned data is consistent with similar work done by (Hoult et al. 2013), as is evidenced by Figure 4.5-5. Here a tensile specimen was imaged from both sides (in an attempt to correct for out of plane errors) and the DIC strains calculated. These were compared to that output by a strain gauge that was also attached to the tensile specimen. The difference in strain (strain error) results are shown for the vertical (ε_v) and horizontal (ε_h) directions, for both sides of the specimen. ε_v on both sides of the specimen is noted to compare favourably with the data seen in Figure 4.5-4.

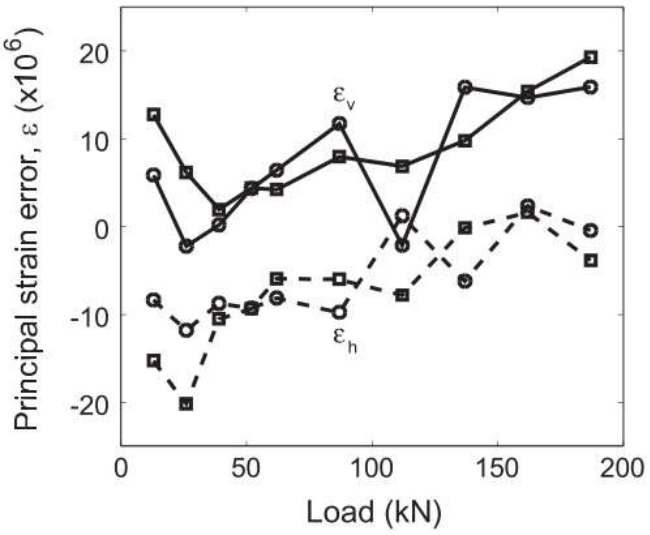

Figure 4.5-5 Strain error in the vertical and horizontal directions on both sides of a tensile specimen (Hoult et al. 2013)

The precision of the DIC strain measurements as quantified by the standard deviations (recall discussion around Figure 3.6-5) are looked at in Figure 4.5-6.

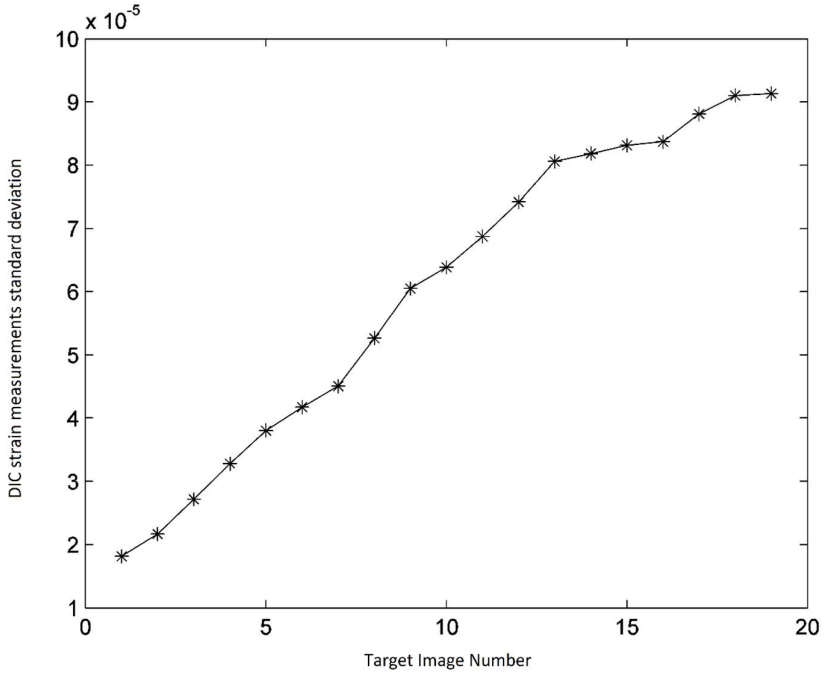

Figure 4.5-6 First principal strain standard deviations for the image set

It demonstrates that the standard deviation of the strain measurements increases with the target image (i.e. increasing applied strain). This increase is indicative of a deterioration in the measurement precision towards the latter images. Precision is therefore also subject to the effects of a deterioration in average correlation coefficient and its standard deviation elaborated on in Figure 4.5-1 and Figure 4.5-2 respectively. The significance of this gradual deterioration of accuracy and precision with increasing applied strain, as it relates to pipework creep strain, is that the user

need be cognisant of the phenomenon when measuring larger strains, and a decision be made on what magnitude of strain error is considered acceptable.

This section worked to establish a baseline DIC accuracy with the chosen setup. It was determined that a strain error of under 20 με is possible for applied strains up to 200 με. This data is consistent with similar tests found in literature. It was found that the average correlation coefficient decreased, while its standard deviation increased, with applied strain. This was argued to be because of deterioration of the correlation algorithm's ability to match subsets as they become more deformed. This also manifested itself in the accuracy (strain error) and the measurement precision (measurement standard deviation), and this need be taken into account when measuring larger strains in a power plant context.

4.6 Variation of subset-size and step-size

This section builds on Section 4.5 and explores the effects of varying the major correlation algorithm parameters – namely subset-size and step size.

Figure 4.6-1 shows the absolute strain error (calculated as per 3.6) as a function of applied strain, as was seen in Section 4.5, Figure 4.5-4. Here though, the subset-size was held constant at 31×31 pixels (the smallest in the chosen range), and the plots for all four of the step-size proportions are shown. Examining first the 6-pixel step-size (corresponding to a step-size proportion of one-fifth of the subset-size), it is evident that the strain errors increase with an increase in the applied strain. This trend is congruent with the data observed in Figure 4.5-4 in the preceding section and is common to all the step-sizes (and subset-sizes as will be seen), albeit to differing degrees. For example, the 15-pixel step-size (one-half of subset-size) trend in Figure 4.6-1 is noted to show this trend to a minimal degree.

Looking at Figure 4.6-1, it is immediately noticeable that the four step-sizes show significantly different strain errors. At the largest applied strain, the strain errors measured using the 6-pixel step-size is around five times greater than that measured using the 15-pixel step-size. However, as was finely detailed in the Section 3.7, this is an artefact of the way that strain is mathematically calculated, coupled with the influence of the measurement precision of the distance between subsets. A change in step-size does not have a physical influence on the accuracy of the measurement. A smaller step-size will be more prone to this artefact and this is clearly observed when comparing the four step-size proportions for all the subset-sizes, seen in Figure 4.6-2, where the 31×31 pixels (used to maximise the range of subset sizes) data is off the chart and would dwarf the rest of the data if included. Thus, to minimise this artefact, the largest DaVis recommended step-size for each subset-size was used going forward. This will however cause a trade off with spatial strain resolution and this will be examined in Section 4.7.

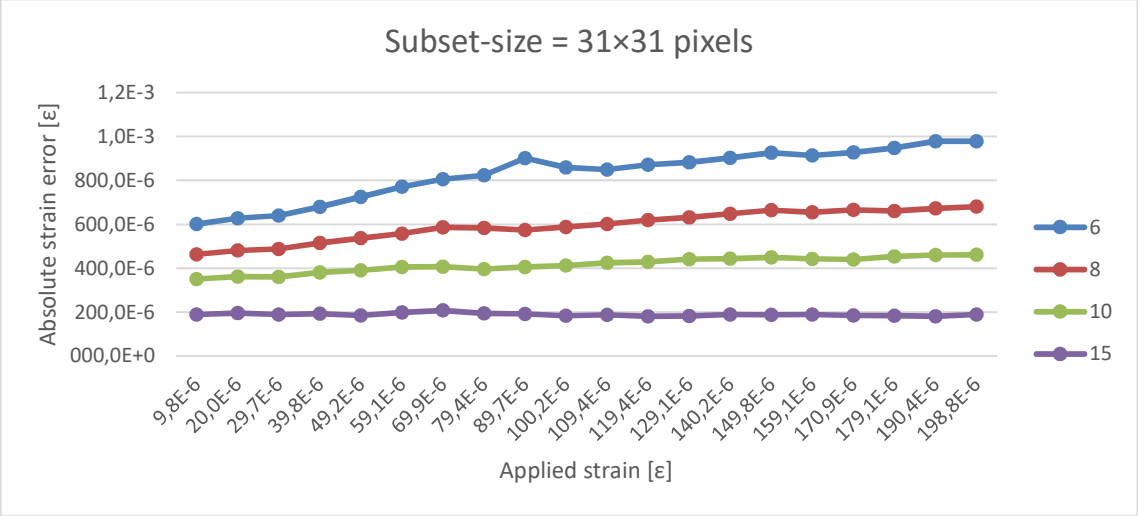

Figure 4.6-1 Absolute strain error as a function of applied strain, for all four step-size ratios chosen. The subset-size was kept constant at 31×31 pixels.

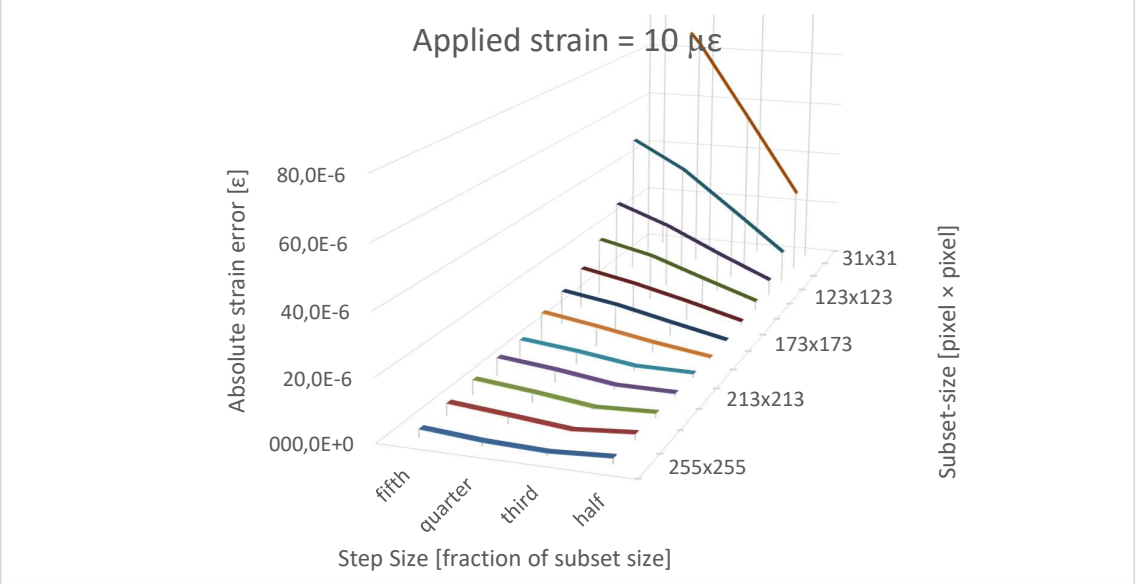

Figure 4.6-2 Using the largest DaVis recommended step-size for a given subset-size minimises the strain calculation artefact. Data calculated at the smallest applied strain of 10 με.

Figure 4.6-3 explores the result of repeating the exercise done in Figure 4.6-1, but using the maximum step-sizes for each subset-size and including the data for all of the subset-sizes tested. A decrease in strain error is seen as the subset-size increases from the rear of the plot to the fore. This supports the findings of (Lecompte et al. 2006), (Pan et al. 2008), (Pan, Lu, and Xie 2010) and (Rajan, Rossol, and Zok 2012). This decrease in strain error is precipitous moving from the smaller subset-sizes, and the ability to discern any detail for the larger subset's plots is impaired in Figure 4.6-3. Thus, the smaller subset-sizes were excluded from the plot in Figure 4.6-4. Here the decrease in strain error with an increase in subset-size is still evident but significantly more gradual. It is inferred that further increase to the subset-size (if the DaVis software allowed) would yield diminishing

returns with regard to decreasing strain error. Measurement noise also becomes much more evident at this zoomed scale as the limits of DIC using this setup are reached.

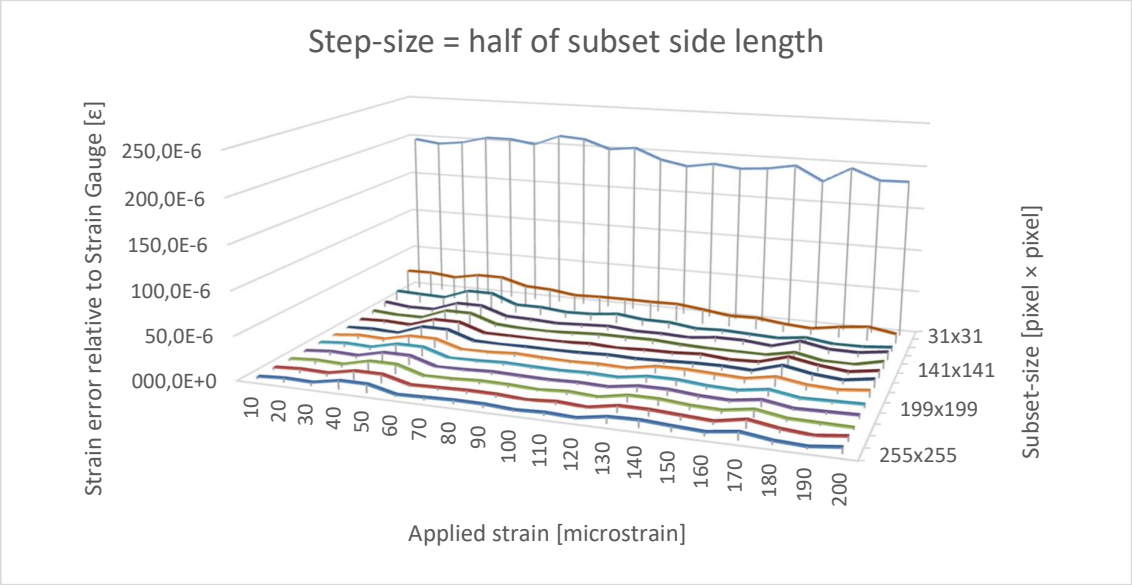

Figure 4.6-3 Strain error for all the subset-sizes. Keeping step-size at one-half of the subset side length.

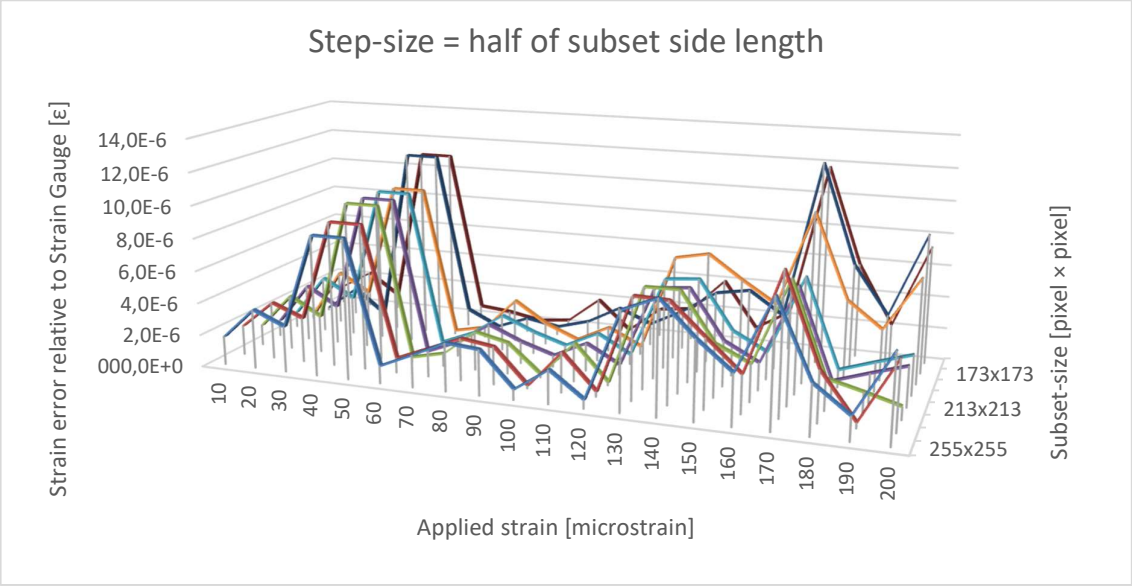

Figure 4.6-4 Keeping step-size at one-half of the subset side length but with the smaller subset-sizes excluded to be able to discern details at the bigger subsets.

The greater accuracy when using bigger subsets is in part attributed to the larger number of features per subset as was seen in Section 4.4, Figure 4.4-1. This larger quantity of information (including more pixels to work with) allows the correlation algorithm to more accurately track the movement of the subsets. Thus, for this setup, that is geared towards measuring strain at a power plant pipe weld, a subset-size larger than around 199 × 199 pixels with a step-size proportion of one-half of subset side length will yield a strain error of around 10 με for applied strains up to 200 με. This is favourably comparable with the capacitive strain gauges used successfully within Eskom plant to

monitor creep strain, which are capable of resolving strains between 5 and 20 με as was noted in the literature (van Zyl et al. 2005). This addresses Objective 5 of this work. It must however be remembered that these tests were performed with homogenous strains under laboratory conditions, and on-site creep will be of a heterogeneous nature under more demanding conditions. Thus this aforementioned accuracy is deemed to be the upper limit of DIC with the given setup and on site measurements can be expected to have somewhat lesser accuracy.

Next the results from testing whether image averaging could improve the noise floor are presented in Figure 4.6-5. Comparing the vertical axis' scaling and the morphology of the plots to Figure 4.6-4, it can be seen that there is marginal change in terms of strain error. The data suggests that there is little benefit in capturing several images per measurement to minimise strain error in this setup. On the practical front, the volume of data when storing large image files becomes substantial (100 GB of data throughout the course of this work), and thus image averaging on several hundred welds where DIC technology may be suitable would generate very large data sets. This would need to be weighed up against the marginal benefits to noise reduction.

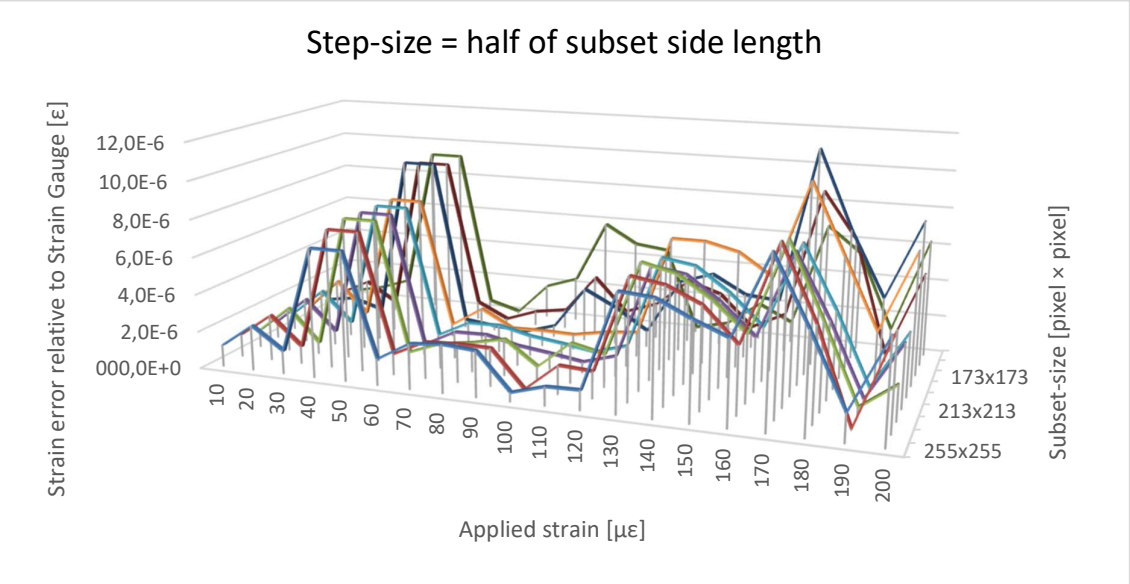

Figure 4.6-5 Averaging of 10 images at each stain step.

Shown in Figure 4.6-6 are the results of repeating the above tests at a different area within the same speckle pattern. Morphological differences in the plots are notable for each subset-size, but no significant differences in strain error is discerned - they are for the most part below 10 με, as was the case before. This data suggests low variability in terms of strain error that is measured at different areas of the speckle pattern. For the application of DIC technology within a power plant context, this result matters to the extent that images may be taken at marginally different areas within a speckle-patterned pipe without significantly affecting results.

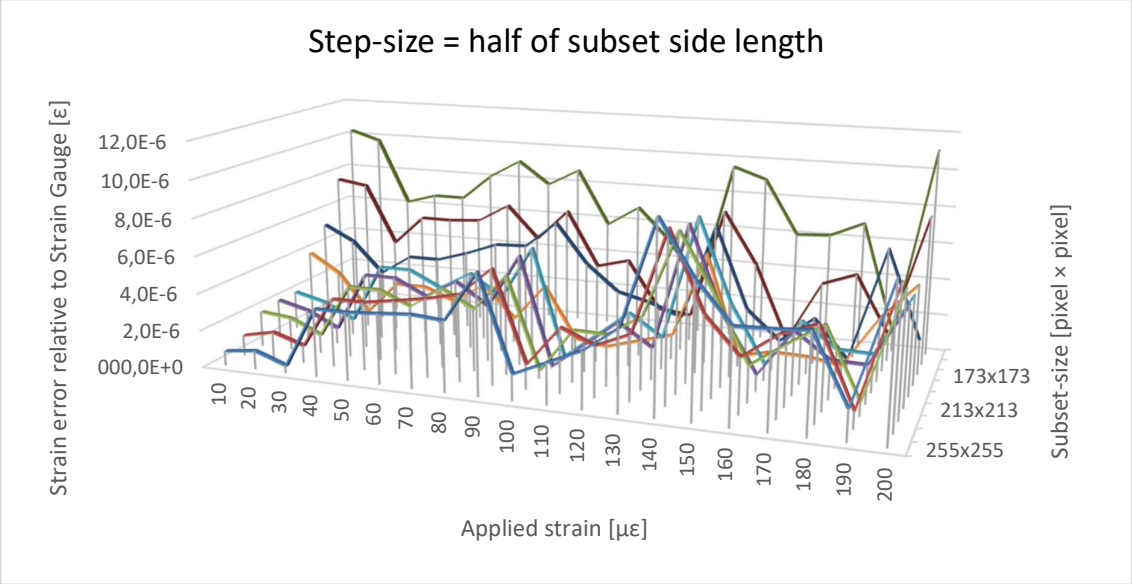

Figure 4.6-6 Repeat of previous test but at a different location in the tensile specimen. Step-size of one-half of the subset-size length but with the smaller subset-sizes excluded to be able to discern details at the bigger subset-sizes.

Finally, a comparison is done between the SP1 and SP4 that were selected. Figure 4.6-7 shows the results from the SP4 that was applied using the aerosol spray can (heat resistant paint). It is seen that in room temperature applications, strain errors of under 10 με are achievable at the larger end of the subset-size range. The DaVis correlation algorithm was robust enough to handle the marginal differences between SP1 and SP4 (intensity signatures, intensity gradient signatures and feature sizes) that were characterised earlier in this work.

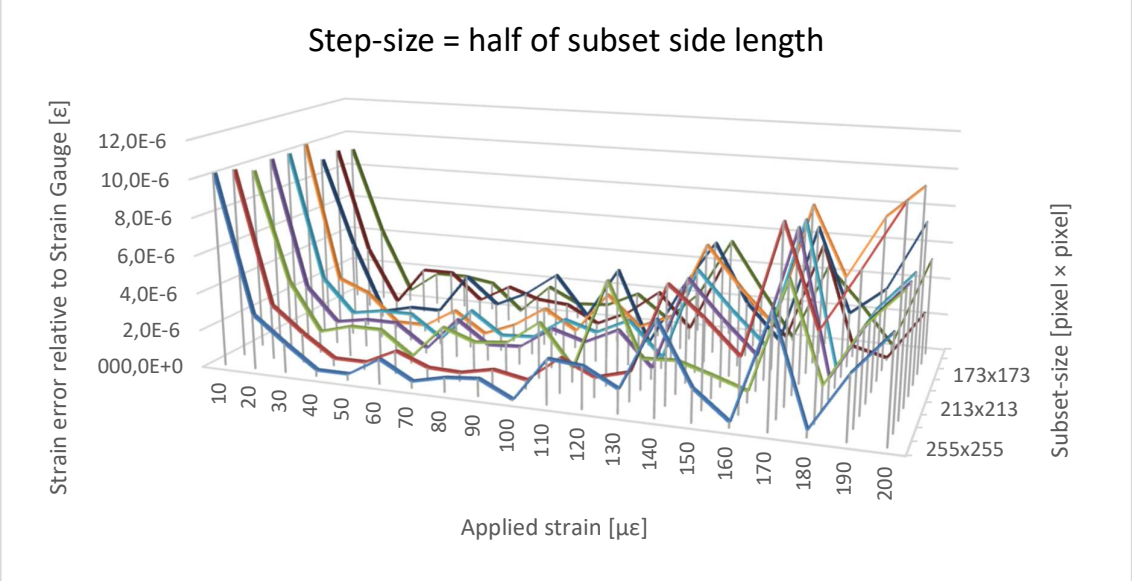

Figure 4.6-7 Changing the speckle pattern to SP 4 (high temperature spray-can paint). Step-size of one-half of the subset-size length but with the smaller subset-sizes excluded to be able to discern details at the bigger subsets.

The foregoing work showed that the strain error generally decreases as the subset-size increases. This tends to plateau at the noise floor after an initial sudden decrease. A maximum accuracy of

around 10 με is achievable with both SP1 and SP4 with the chosen hardware setup. The methodology used in this section is capable of practically ascertaining the measurement accuracy of any chosen speckle pattern, applied on a tensile specimen upon which a given hardware setup can effectively focus. It is envisioned that this could potentially be used as a part of a qualification process for DIC equipment and speckle patterns marketed by suppliers.

4.7 Spatial strain resolution

The foregoing data suggests that maximising subset-size will maximise accuracy. However, large subsets will smooth out strain gradient data that is within the subset. The effects of increasing subset-size on strain resolution are presented below.

In Figure 4.7-1 the vertical axis shows the average error between the strain data points on the analytical field and that generated by the DIC measurements of the CT specimen. The reader is reminded that the step-size was chosen to be one-fifth of the subset side length. The horizontal axis shows the increasing subset-size, with the largest subset-size omitted since it generated too few data points to warrant inclusion. The depth axis shows the stress intensity factor (the proxy parameter for strain gradient) calculated at the indicated image numbers.

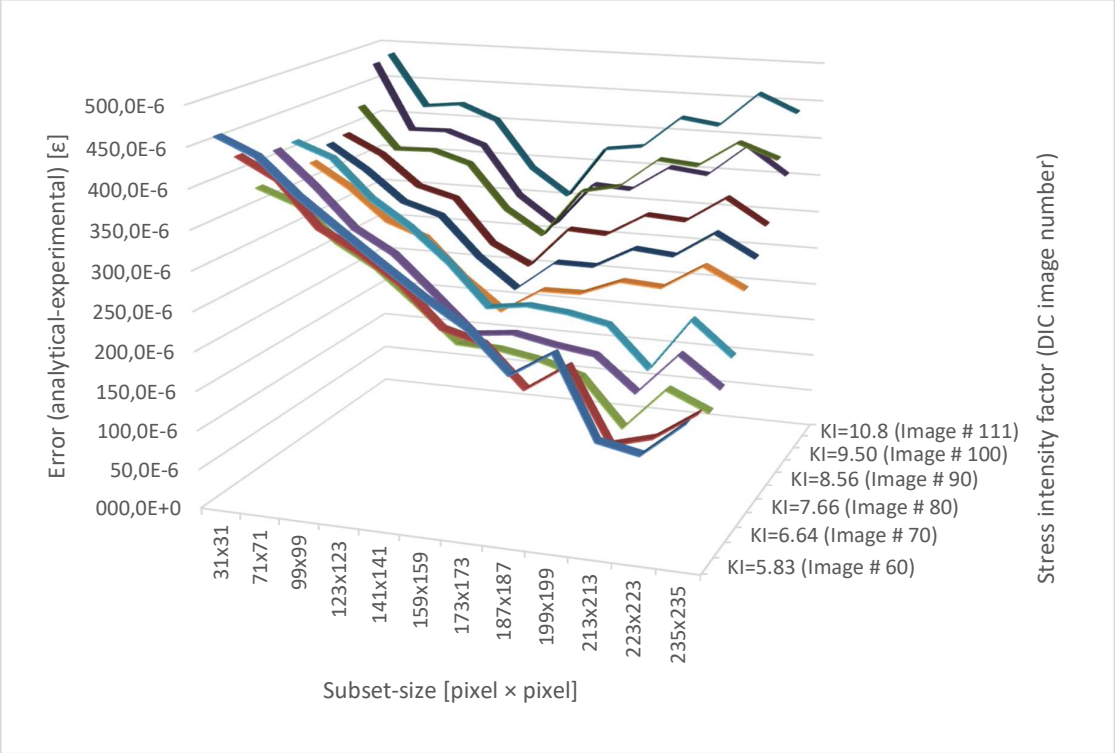

Figure 4.7-1 Trade-off between subset-size and strain resolution.

It is noted that for the flatter strain gradients (lower KI values), the error tends to generally decrease proportionally with an increase in subset-size. However, as the strain gradient increases in the latter images of the sequence (steeper strain gradients), an inflection point is reached at which strain error begins to increase again. This is noted to occur at around a subset-size of 141 × 141 pixel for a KI of 8.56. This subset-size cannot be related directly to the data generated from the tensile specimens tested in this work because there are several differences between the two tests, including

homogeneous versus heterogeneous deformation and different substrate materials. However, the trend seen in Figure 4.7-1 gives valuable insight into the trade off between accuracy and spatial resolution with increasing subset-size. The data suggests that for a given DIC setup measuring high strain gradients, there exists a subset-size at which strain error is minimised. A good compromise would therefore be to use the subset-size corresponding to the inflection point (if there is one for the expected strain gradient to be measured). This work focussed on pipework weld HAZ, but were DIC used for other power plant applications, similar datasets would be useful in subset-size choice depending on strain gradient expected. If low strain gradients are expected (e.g. a pipework hanger), resolution is not as important and bigger subsets would be used to maximise accuracy. However, in high strain gradient fields such as detailed HAZ analysis, it would be wise to use a smaller subset-size that maximises the resolution while giving moderate accuracy.

This section provided insight into the trade-off between accuracy and strain resolution as a result of subset-size choices. It showed that the biggest subset sizes which were earlier seen to maximise accuracy have a penalty in terms of strain resolution when measuring higher strain gradients.

4.8 Thermal sensitivity tests

In this section, the effects of temperature on strain accuracy were studied to determine whether DIC is suitable for online power plant measurement or limited to acquiring measurements when the plant is shut down and the pipework cooled. The accuracies determined in the prior section provided the context from which comparison were drawn.

Notwithstanding the several precautions taken in the Experimental Methodology to mitigate expansion/contraction during the quasi steady state intervals when measurements were being acquired, a validation was nonetheless required. The DIC strains measured for the 100 sequential images acquired are shown in Figure 4.8-1. The reader is reminded that the subset-size and step-size were 255×255 pixels and 127 pixels respectively. The entire sequence of image capturing took a period one order of magnitude longer than that of the ten-image bursts used for Figure 4.8-4 (the final data). Therefore, if any transient expansion/contraction effects were to have occurred, it would have been noticed in the 100-image sequence more prominently than in the final ten-image sequences.

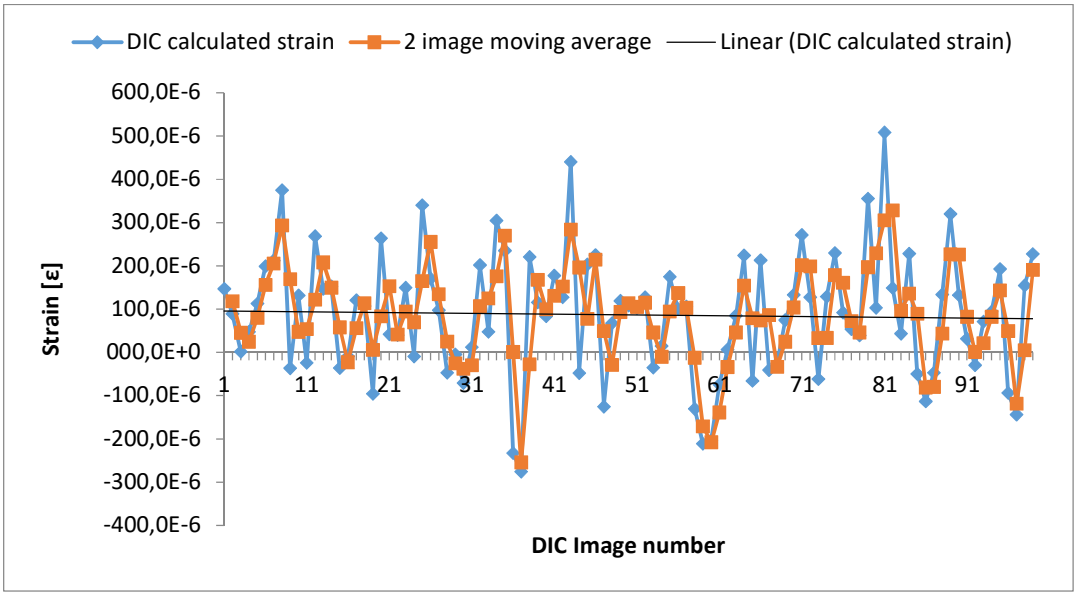

Figure 4.8-1 100 image DIC calculated strain, also showing a linear trendline fitted to the data as well as a two-image moving average.

Immediately noticeable is that the data is not scattered about 0 με as would be expected, but rather hovers above this. The linear trendline for this dataset included in Figure 4.8-1 shows that the data in fact hovers close to 100 με. This was later attributed to error introduced when measuring at elevated temperature as will be elaborated on in the discussion around Figure 4.8-4. Notwithstanding this, the trendline is noted to be virtually horizontal and hence changes in strain are negligible. Over a duration 20 seconds (0.2 s per image), an order of magnitude longer than the what the following tests were run at, there is no upward/downward trend in strain within the limitations of measurement noise. If expansion/contraction were to be registered in this time interval, a salient gradient would be evident. It is also to be remembered that this dataset was acquired at the most extreme temperature of 585 °C to elicit the most detrimental effects, and thus datasets acquired at lower temperatures would be even less vulnerable to these aforementioned strain effects.

Moving averages of the data were taken to look for any obvious trend within the noise. Figure 4.8-1 includes the dataset generated using a two-image moving average. This is however observed not to have any significant noise attenuation relative to the original data and thus a longer moving average was needed. In Figure 4.8-2, a ten-image moving average was calculated (which is also the averaging performed for each of the six bursts that were ultimately used to generate Figure 4.8-4). This averaging is seen to substantially reduce the noise in the data relative to Figure 4.8-1. Somewhat of a trough is noted at around image 64 and the trend then picks up again. This cannot be attributed to expansion since the heating coil was de-energised (i.e. no energy input to the system) throughout this dataset. This anomaly is presumed to be due to some disturbance in the flow of the hot air surrounding the pipe surface, affecting the refractive index. Figure 4.8-3 depicts an extreme of the image averaging – calculated for every twenty images. It is noted that the noise is again reduced somewhat, however there are diminishing returns when compared to Figure 4.8-2.

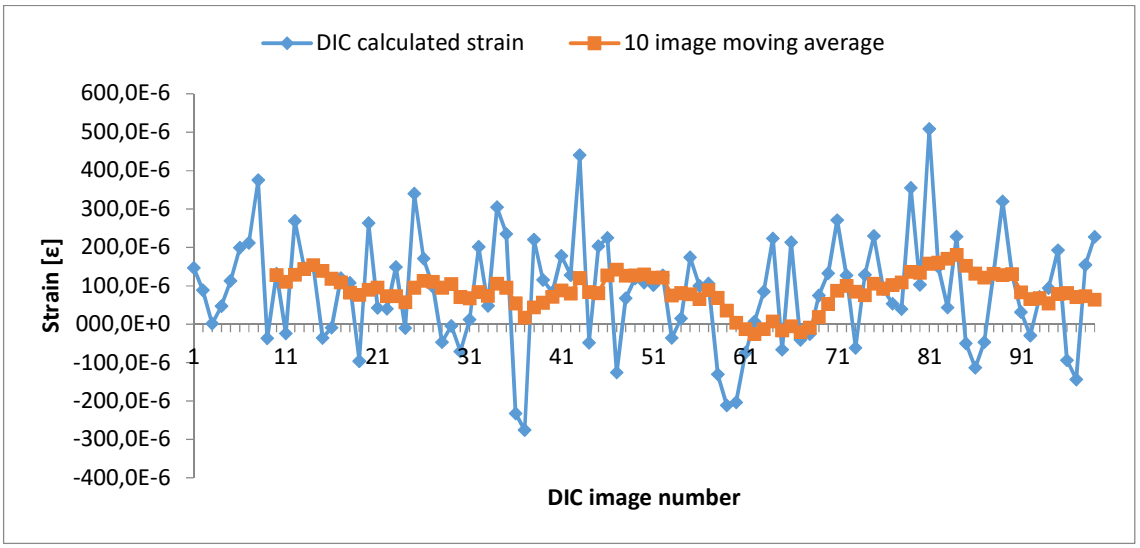

Figure 4.8-2 100 image DIC calculated strain dataset with a ten-image moving average superimposed.

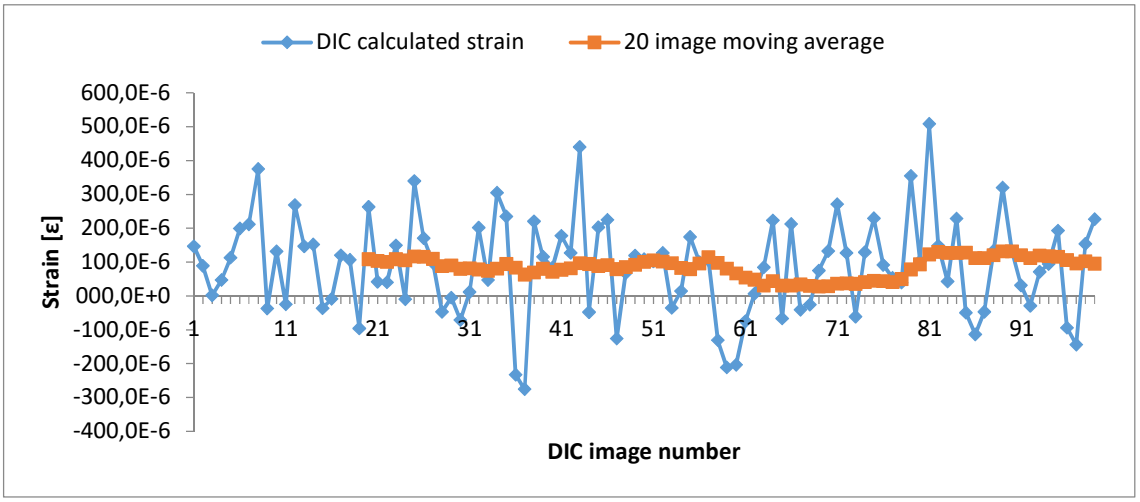

Figure 4.8-3 100 image DIC calculated strain dataset with a twenty-image moving average superimposed.

Finally, the effects of temperature on the accuracy are looked at, and Figure 4.8-4 shows the DIC calculated strains as a function of pipe surface temperature. The measured strains (strain errors) are observed to increase with the increasing temperature, having an order of magnitude difference within the range of temperatures tested. To put this into context, the strain errors observed in Figure 4.6-7 (the accuracy tests using the spray-can speckle pattern) had a noise floor in the region of 10 με, which is comparable to the 8 με error calculated at 100 °C in Figure 4.8-4. This suggests that at up to 100 °C, the DIC system maintains its baseline accuracy.

However, at Lethabo power station operating temperatures of 535 °C (upon which this heating rig was modelled) the error increased to 95 με. This deteriorates further for supercritical plant conditions, measuring in an error of over 145 με. Notable at highest tested temperatures is that the standard deviation of the data generally encompasses the 100 με observed in the trendline of Figure 4.8-1, and thus this offset from the expected 0 με is indeed attributed to the noise introduced by measuring at higher temperatures. Strain errors of the magnitude observed at the aforementioned

higher temperatures would obscure smaller measured strains, i.e. large creep strains would be needed to tip the signal-to-noise ratio past an adequate threshold (that Eskom would need to decide upon). The implications for online measurements are that the periods between measurements would likely need to be extensive for the creep strain to accumulate sufficiently to achieve the said signal-to-noise threshold. In the interim between these measurements, online DIC measurements may be useful to monitor trends in the strain data but more research would be needed in this regard.

The standard deviation (error bars) of the six sample points taken at each temperature increment is also observed to increase as the temperature increases. It is hypothesised that this is due to the changing refractive index of the air between the pipe surface and the camera. The increasing turbulence in the air surrounding the pipe surface (i.e. greater natural convection currents) marginally changes where the imaging system perceives the speckles to be due to the refraction of light off of the pipe surface, and hence causes variability in the strain that the DIC system calculates. Further experimental observation would be needed to substantiate this hypothesis, however regardless of the understanding of underlying mechanisms, this data suffices for this work to conclude that measurement at temperature has a significant detrimental effect on DIC accuracy and precision. Thus, from a temperature perspective, DIC is more suitable for offline measurements in a power plant context.

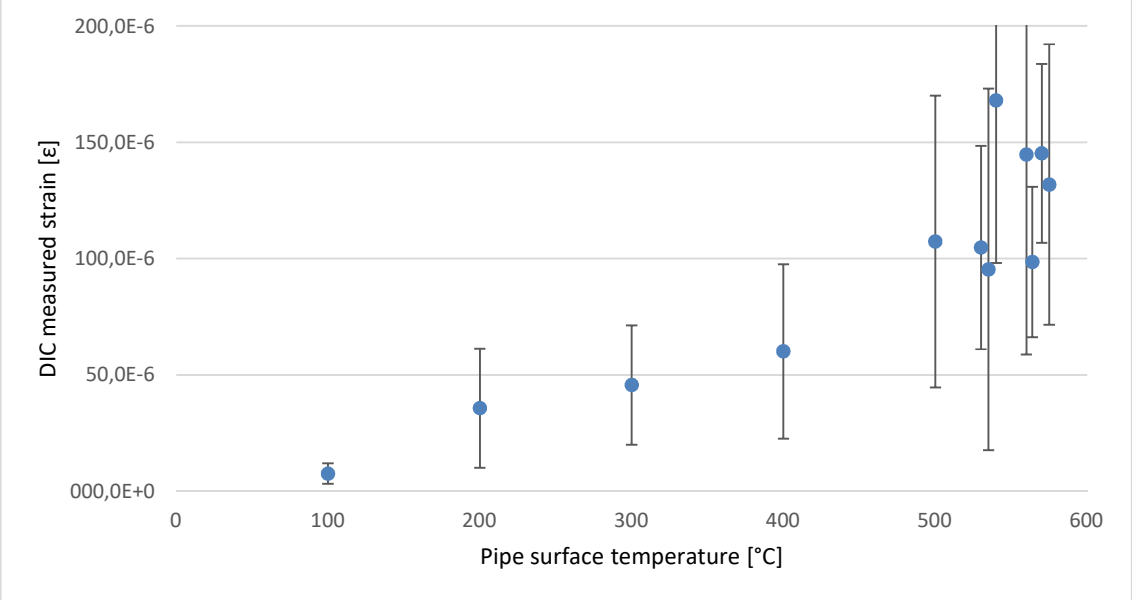

Figure 4.8-4 Error measured with increasing temperature

Other operational experience that was noted in this experimentation is that telecentric lenses would be at risk to damage when used at temperature on a power plant. Because of the physics of the optics, for a given field of view, telecentric lenses have a set focal length and a narrow depth-of-field in which the image is in focus. The lens therefore has to be placed very close (62.2 mm in this case) to the surface in order to narrow in on the HAZ of the weld. A longer focal length (to maximise distance from the hot surface) would necessitate the next biggest telecentric lens that is commercially available, which would invariably have a larger field of view. Measures like heat resistant glass can be used to mitigate the convective effects of the heat from the pipe, however the

radiative effects would still be present. It is to be remember that the decision to use a telecentric lens follows recommendations by literature to maximise accuracy when using a single camera (2D) setup. 3D DIC setups could also be used, since they account for out of plane deformation and thus are not limited to using telecentric lenses. However, this raises a new set of concerns such as repeatable mounting of the cameras and questions of calibration, and thus more research would be needed in this regard.

In this section, the effects of DIC measurements taken at temperature on pipework that simulated that found on-site was looked into. The data suggests that online DIC measurement is prone to significant strain errors. Operational risks in terms of protecting the equipment were also identified. Thus from an accuracy and precision perspective as well as an operational one, this research suggests that offline DIC measurements are more practical.

5 Summary and Conclusion

This work started with a review of published literature and theoretical work pertaining to creep-strain in power plants, and its measurements thereof. Digital Image Correlation (DIC), an image-based strain measuring technology, was identified as a tool which could not only compliment current creep measuring tools, but also address several of their shortcomings. This work thus embarked on determining the measurement accuracy that could be achieved, and the feasibility of the technology in a power plant context. In particular, this work focused its scope on an area representative of the width that the pipework weld's Heat Affected Zone (HAZ) would occupy. The HAZ is to be the weakest part in a pipework weldment and thus the most important area for measurement. Further study of the main elements comprising DIC and the parameters affecting its accuracy were therefore examined to make a decision on an optimised setup.

Armed with the above insights, a 2D DIC system in a configuration optimised for creep strain measurement of the aforementioned hypothetical HAZ area was specified. This incorporated a single camera with a 5 Megapixel CCD image sensor, coupled to a telecentric lens with a Field Of View (FOV) of 8.44 mm × 7.06 mm. All the hardware was controlled via a central unit connected to a computer that was running DaVis – a proprietary DIC software package. Several speckle patterns were applied to the gauge area of standard tensile specimens with an airbrush and an aerosol spray-can. Of these, eight that adhered to qualitative recommendations made in literature were selected for further analysis.

These eight speckle patterns were analysed using a toolbox of techniques, namely: intensity histograms; intensity gradients; feature size and speckle pattern density per subset. These tools collectively gave insight into the following:

- Adherence of the individual speckle patterns to recommendations made in literature
- Quality control of the imaging system setup
- Characterisation of the speckle patterns

These tools proved effective with the large range of speckle patterns presented to them, showing high sensitivity to differences. Notwithstanding this, it was found that not all of the tools were suitable for use with all of the speckle patterns, and initial discretion and screening is vital. Of the eight speckle patterns, one using the airbrush and a second using the aerosol spray-can were deemed suitable for further use in this work. The spray-can speckle pattern was used for comparative purposes, and later in the work the technique would be used in high temperature tests. Strain gauges were adhered to the tensile specimen in a configuration optimised for sensitivity to strain in the specimen's axial direction. These readings were used as the reference from which the DIC strain error would be quantified. The tensile specimen was subsequently strained within a tensile testing machine to values congruent with the strain resolution capabilities of the capacitive strain gauges that are used in power plant creep strain measurements. The deformations were captured and analysed with DIC, using a mid-range step-size and subset-size of 121×121 pixels and 60 pixels respectively.

Analysis of the intermediate steps and data prior to obtaining the final strain readings was done. It was noted that there was an adverse trend in the correlation coefficient's values and standard

deviation as applied strain increased, indicating deteriorating precision at larger strains. The values were however all satisfactorily above 0.95. Artefacts at the edge of the strain vector fields were clearly seen - artefacts from the correlation process. These, were dealt with by averaging of strain field data, which was reasonable due to the homogenous nature of the field in a tensile specimen gauge area. The analysis of heterogeneous strain fields is recommended for future work. Ultimately, a strain error well under 20 με was achievable and this result resonated with other work found in literature. This laid the foundation on which the effects of variation in step-size and subset-size on the strain error could be investigated.

On the step-size front, a testing matrix of dynamic step-sizes that were a function of subset-size was developed. As expected, measuring artefacts (that are related to the way strain is calculated) manifested themselves in the data. This artefact is minimised when using larger step-sizes and this strategy was adopted. Thus, the maximum step-size recommended by DaVis (for a given subset-size) was used, having the trade-off of sacrificing the quantity of data points in the vector fields.

Previously published work showed that an increase in subset-size has an effect on strain error and this was indeed noted in this work. The use of a larger subset-size reduced the strain error, precipitously so at the smallest subset-sizes used. This reduction in strain error however tended to plateau at the larger subset-sizes, yielding diminishing returns. Using the larger subset-sizes, the strain errors measured were under 10 με for applied strains up to 200 με, and this was concluded to be the limit of the current set-up. The strain resolution that the capacitive strain gauges are able to discern was reported to be between 5 με and 20 με and thus DIC is noted to be comparable to capacitive strain gauges in this regard. The caveat is that these measurements are done under controlled conditions and are of homogeneous strain fields, and thus in-situ measurements on a power plant would likely show greater strain error.

Several more data sets were captured to investigate other aspects of the DIC strain error measurements. Image averaging was done over ten images per applied strain step to increase the signal-to-noise ratio, and is concluded to have marginal, if any, effects in this setup. The strain error measurements were repeated at a different location within the gauge area and this did not result in any notable difference in the minimum strain errors as compared to results from the original area. Lastly, repeating the analysis on an aerosol spray-can speckle pattern did not adversely affect the strain error results significantly. It is thus concluded that the DIC system is robust enough to handle some variability.

Maximising the DIC parameters for accuracy, however, has the trade-off of a lower spatial resolution which will smooth-out high strain gradients. DIC data from the evolving strain gradient ahead of a propagating crack front was analysed to understand the trade-off. It was seen that for high strain gradients the strain error decreases with an increase in subset-size up to a threshold, upon which an inflection point ensues and strain error subsequently increases. It is thus concluded that the DIC user should be cognisant of the type of measurement that the technology will be used for. If high accuracy is the primary concern, then larger subset-sizes are recommended, keeping in mind the diminishing returns. However, if the intricacies of high strain gradient regions are to be investigated, a reduction in subset-size may be required to be able to discern those details.

The effects of temperature on DIC measurements was considered. Online (at temperature) measurements were concluded to introduce significant errors and thus serious attention should be

given to these effects if online measurements are still to be pursued. The error at power plant operating temperature was noted to be around 95 με which is over 9 times that established for the technology earlier in the work. Additionally, there is the risk of heat damage to equipment if telecentric lenses are to be used due to their short, fixed, focal lengths and shallow depth of field.

This work ends off with some suggestions of future work that may be pursued to answer questions that have arisen in the course of this investigation but were not core to the objectives laid out at the onset.

6 Future Work and Recommendations

The next logical refinement in this work on the road-map to full in-situ testing at a power plant would be to investigate the accuracy that DIC yields when measuring heterogeneous strains. This would ideally be accomplished on representative pipework models. Eskom is in possession of thick component creep testing equipment at their Research and Testing facility in Rosherville, Gauteng. This equipment essentially comprises of thick-walled pipework that is sealed at both ends and is pressurised by gas to induce straining of the material, simulating what would be experienced on plant. The equipment is out of commission and would need to be returned to a working state. This experimentation is considered dangerous because of the very large energies involved in pressurising the pipework and so expert assistance is recommended. The methodologies used in this work would remain essentially unchanged and direct comparison to this work would in large part be possible.

Of next priority would be to better understand the mechanisms causing the large strain errors when DIC measurements are done at high temperature. Online measurement has advantages including being able to do continuous monitoring on pipework which is deemed to be high risk. Examples of such cases are when new pipework is not readily available during a shutdown to replace creep-damaged sections. Management needs to do a risk assessment and make a decision on whether the plant can be put back online or not. Online monitoring of such pipework gives additional data to quantify the extent of the risk. Thermographic studies of the hot pipework model used in this work are suggested to gain insight into the natural convection currents that are established at high temperature. Testing of mitigating strategies such as placing the speckle pattern under a vacuum to establish what benefits to accuracy may be gained are also reasonable tests to carry out.

The combination of the two aforementioned suggestions is also a possible area of research. The same thick component testing facility that was cited above is capable of elevating the temperature of the thick-walled pipework within a furnace. This would be the closest simulation to in-situ power plant testing. Two major challenges however exist with this. Firstly, the furnace would need to be modified to allow the cameras to look into it. Secondly, a telecentric lens would not be able to be used as the distance from the furnace exterior to the pipework surface would exceed the stand off distance of most commercially available telecentric lenses. 3D DIC would need to be explored in this application.

A final area of research into which power plant DIC could be extended would be to explore its feasibility in applications other than monitoring the straining of the weld HAZ. DIC being scale independent opens scope to monitor phenomenon such as surface crack propagation on components like turbine valve casings. This strays somewhat from the core of this work but extends the possibilities of taking advantage of DIC's full field measuring capabilities.

7 Bibliography

Anderson, T.L. 2005. *Fracture Mechanics: Fundamentals and Applications*. Third Edit. CRC Press LLC.

Bing, Pan, Xie Hui-min, Xu Bo-qin, and Dai Fu-long. 2006. "Performance of Sub-Pixel Registration Algorithms in Digital Image Correlation." *Measurement Science and Technology* 17 (6): 1615–21. doi:10.1088/0957-0233/17/6/045.

Bruck, H. A., S. R. McNeill, M. A. Sutton, and W. H. Peters. 1989. "Digital Image Correlation Using Newton-Raphson Method of Partial Differential Correction." *Experimental Mechanics* 29 (3): 261–67. doi:10.1007/BF02321405.

Chu, T. C., W. F. Ranson, and M. A. Sutton. 1985. "Applications of Digital-Image-Correlation Techniques to Experimental Mechanics." *Experimental Mechanics* 25 (3): 232–44. doi:10.1007/BF02325092.

Crammond, G, S W Boyd, and J M Dulieu-Barton. 2013. "Speckle Pattern Quality Assessment for Digital Image Correlation." *Optics and Lasers in Engineering* 51 (12): 1368–78. doi:http://dx.doi.org/10.1016/j.optlaseng.2013.03.014.

Edmund Optics. 2017. "Parallax Error." Accessed April 19. https://www.edmundoptics.com/resources/application-notes/imaging/advantages-of-telecentricity/.

Ennis, P J, and A Czyrska-Filemonowicz. 2003. "Recent Advances in Creep-Resistant Steels for Power Plant Applications." *Sadhana* 28 (3): 709–30. doi:10.1007/BF02706455.

Francis, J A, W Mazur, and HKDH Bhadeshia. 2006. "Review Type IV Cracking in Ferritic Power Plant Steels." *Materials Science and Technology* 22 (12). Maney Publishing: 1387–95.

Gao, Jianxin. 2016. "CREEPIMAGE (Developement of a Long Term Creep Monitoring Technique Image Based) - Final Report Summary." http://cordis.europa.eu/result/rcn/145940_en.html.

Haddadi, H., and S. Belhabib. 2008. "Use of Rigid-Body Motion for the Investigation and Estimation of the Measurement Errors Related to Digital Image Correlation Technique." *Optics and Lasers in Engineering* 46 (2): 185–96. doi:10.1016/j.optlaseng.2007.05.008.

Hoffmann, Karl. 2001. "Applying the Wheatstone Bridge Circuit." *HBM S1569-1.1 En, HBM, Darmstadt, Germany*. http://paginas.fisica.uson.mx/horacio.munguia/aula_virtual/Cursos/Instrumentacion II/Documentos/Teoria Ctos Puentes.PDF.

Holdsworth, S. R., M. Askins, A. Baker, E. Gariboldi, S. Holmström, A. Klenk, M. Ringel, et al. 2008. "Factors Influencing Creep Model Equation Selection." *International Journal of Pressure Vessels and Piping* 85 (1–2): 80–88. doi:10.1016/j.ijpvp.2007.06.009.

Hoult, Neil A., W. Andy Take, Chris Lee, and Michael Dutton. 2013. "Experimental Accuracy of Two Dimensional Strain Measurements Using Digital Image Correlation." *Engineering Structures* 46. Elsevier Ltd: 718–26. doi:10.1016/j.engstruct.2012.08.018.

"How Focal Length Affects Viewing Angle." 2017. Accessed April 19. http://av.jpn.support.panasonic.com/support/global/cs/dsc/knowhow/knowhow12.html.

Huchzermeyer, Richard Lynn. 2017. “Measuring Mechanical Properties Using Digital Image Correlation: Extracting Tensile and Fracture Properties from a Single Sample.” University of Stellenbosch.

Hulshof, H J M, P G M Welberg, and L E Bruijn. 2005. “Creep Strain Measurements for Risk Based Monitoring of Steam Pipes and Headers.” In *ECCC Creep Conference*, 12–14. London.

Hulshof, Harry, and Joop Kraijesteijn. 2011. “Creep Monitoring in High Energy Piping.” *ASME 2011 Power Conference*, 1–6. doi:10.1115/POWER2011-55203.

“Image Sensor Size Chart.” 2017. Accessed April 21. https://www.dpreview.com/forums/post/53884953.

“ImageJ User Guide.” 2017. Accessed August 10. https://imagej.nih.gov/ij/docs/guide/146-29.html.

“Imaging System Fundamental Parameters.” 2017. Accessed June 4. https://www.edmundoptics.com/resources/application-notes/imaging/5-fundamental-parameters-of-an-imaging-system/.

Lava, P., S. Cooreman, S. Coppieters, M. De Strycker, and D. Debruyne. 2009. “Assessment of Measuring Errors in DIC Using Deformation Fields Generated by Plastic FEA.” *Optics and Lasers in Engineering* 47 (7–8): 747–53. doi:10.1016/j.optlaseng.2009.03.007.

Lava, P., S. Cooreman, and D. Debruyne. 2010. “Study of Systematic Errors in Strain Fields Obtained via DIC Using Heterogeneous Deformation Generated by Plastic FEA.” *Optics and Lasers in Engineering* 48 (4). Elsevier: 457–68. doi:10.1016/j.optlaseng.2009.08.013.

Lecompte, D., A. Smits, Sven Bossuyt, H. Sol, J. Vantomme, D. Van Hemelrijck, and A. M. Habraken. 2006. “Quality Assessment of Speckle Patterns for Digital Image Correlation.” *Optics and Lasers in Engineering* 44 (11): 1132–45. doi:10.1016/j.optlaseng.2005.10.004.

Lionello, Giacomo, and Luca Cristofolini. 2014. “A Practical Approach to Optimizing the Preparation of Speckle Patterns for Digital-Image Correlation.” *Measurement Science and Technology* 25 (10): 107001. doi:10.1088/0957-0233/25/10/107001.

Luu, Long, Zhaoyang Wang, Minh Vo, Thang Hoang, and Jun Ma. 2011. “Accuracy Enhancement of Digital Image Correlation with B-Spline Interpolation.” *Optics Letters* 36 (16): 3070–72. doi:10.1364/OL.36.003070.

Maharaj, C., J. P. Dear, and A. Morris. 2009. “A Review of Methods to Estimate Creep Damage in Low-Alloy Steel Power Station Steam Pipes.” *Strain* 45 (4): 316–31. doi:10.1111/j.1475-1305.2008.00465.x.

Masuyama, F. 1998. “New Developments in Steels for Power Generation Boilers.” *Advanced Heat Resistant Steel for Power Generation*, 33–48.

Masuyama, Fujimitsu. 2001. “History of Power Plants and Progress in Heat Resistant Steels.” *ISIJ International* 41 (6). 612–25.

Mayr, Peter, and Horst Cerjak. 2010. “The Impact of Welding on the Creep Properties of Advanced 9-12 % Cr Steels.” *Transactions of The Indian Institute of Metals* 9 (2–3): 131–36. doi:10.1007/s12666-010-0018-9.

“Measuring Strain with Strain Gages.” 2016. http://www.ni.com/white-paper/3642/en/.

Molokwane, T.J. 2014. “Weldability Limits for X20 Steel HP Pipework.”

Morris, A., J. Dear, and M. Kourmpetis. 2006. “High Temperature Steam Pipelines - Development of the ARCMAC Creep Monitoring System.” *Strain* 42 (3): 181–85. doi:10.1111/j.1475-1305.2006.00269.x.

Morris, A., J. Dear, M. Kourmpetis, C. Maharaj, A. Puri, and A. Fergusson. 2007. “Monitoring Creep Strain in Power Station Engineering Plant.” *Applied Mechanics and Materials* 7–8 (January): 31–36. doi:10.4028/www.scientific.net/AMM.7-8.31.

Narayanan, A., C. Maharaj, M. Kelly, A. Morris, C. M. Davies, and J. P. Dear. 2016. “Recent Developments in Measuring Creep Strain in High Temperature Plant Components.” *Strain* 52 (6): 467–77. doi:10.1111/str.12187.

Pan, B. 2011. “Recent Progress in Digital Image Correlation.” *Experimental Mechanics* 51 (7): 1223–35. doi:10.1007/s11340-010-9418-3.

Pan, Bing, Zixing Lu, and Huimin Xie. 2010. “Mean Intensity Gradient: An Effective Global Parameter for Quality Assessment of the Speckle Patterns Used in Digital Image Correlation.” *Optics and Lasers in Engineering* 48 (4). Elsevier: 469–77. doi:10.1016/j.optlaseng.2009.08.010.

Pan, Bing, Kemao Qian, Huimin Xie, and Anand Asundi. 2009. “Two-Dimensional Digital Image Correlation for in-Plane Displacement and Strain Measurement: A Review.” *Measurement Science and Technology* 20 (6): 62001. doi:10.1088/0957-0233/20/6/062001.

Pan, Bing, Huimin Xie, Zhaoyang Wang, Kemao Qian, and Zhiyong Wang. 2008. “Study on Subset Size Selection in Digital Image Correlation for Speckle Patterns.” *Optics Express* 16 (10). OSA: 7037–48. doi:10.1364/OE.16.007037.

“R72 Sayce Logarithmic Optical Test Chart.” n.d. http://www.pyser-sgi.com/graticules/optical-resolution-charts/sayce-logarithmic/r72-sayce-logarithmic-test-chart-detail.

Rajan, V. P., M. N. Rossol, and F. W. Zok. 2012. “Optimization of Digital Image Correlation for High-Resolution Strain Mapping of Ceramic Composites.” *Experimental Mechanics* 52 (9): 1407–21. doi:10.1007/s11340-012-9617-1.

Reynolds, A P, and F Duvall. 1999. “Digital Image Correlation for Determination of Weld and Base Metal Constitutive Behavior.” *Welding Journal* 78 (10): 355.

Rooyen, Melody Van. 2016. “Thermal Power Plant Steel Creep Deformation Measurement Using Stereo Digital Image Correlation.” Stellenbosch University.

Rossi, M., P. Lava, F. Pierron, D. Debruyne, and M. Sasso. 2015. “Effect of DIC Spatial Resolution, Noise and Interpolation Error on Identification Results with the VFM.” *Strain* 51 (3): 206–22. doi:10.1111/str.12134.

Rossi, Marco, and Fabrice Pierron. 2012. “On the Use of Simulated Experiments in Designing Tests for Material Characterization from Full-Field Measurements.” *International Journal of Solids and Structures* 49 (3–4). Elsevier Ltd: 420–35. doi:10.1016/j.ijsolstr.2011.09.025.

Rothwell, John, and Peter Mayr. 2014. “The Cross-Weld Performance of 9%Cr Creep-Resistant Steels, and the Influence of Welding Parameters.” In *7th International Conference on Advances in Materials Technology for Fossil Power Plants*, 1313. Waikoloa, HI, United states.

Rubin, D. M. 2004. “A Simple Autocorrelation Algorithm for Determining Grain Size from Digital Images of Sediment.” *Journal of Sedimentary Research* 74 (1): 160–65. doi:10.1306/052203740160.

Schreier, Hubert W, and Michael A Sutton. n.d. “Systematic Errors in Digital Image Correlation due to Undermatched Subset Shape Functions.” *Experimental Mechanics* 42 (3): 303–10. doi:10.1007/BF02410987.

Sposito, G, C Ward, P Cawley, P B Nagy, and C Scruby. 2010. “A Review of Non-Destructive Techniques for the Detection of Creep Damage in Power Plant Steels.” *NDT & E International* 43 (7): 555–67. doi:http://dx.doi.org/10.1016/j.ndteint.2010.05.012.

Sutton, Michael A, Jean-José Orteu, and Hubert W Schreier. 2009. *Image Correlation for Shape, Motion and Deformation Measurements*. Springer US.

Sutton, Michael A, J H Yan, V Tiwari, H W Schreier, and J J Orteu. 2008. “The Effect of out-of-Plane Motion on 2D and 3D Digital Image Correlation Measurements.” *Optics and Lasers in Engineering* 46 (10): 746–57. doi:http://dx.doi.org/10.1016/j.optlaseng.2008.05.005.

“The Paris Agreement.” 2017. http://unfccc.int/paris_agreement/items/9485.php.

Viswanathan, R. 2000. “An Overview of Failure Mechanisms in High Temperature Componenets in Power Plants.”

Xu, Xiuchai. 2017. “Depth of Field.” Accessed April 19. http://www.bigsunphotography.com/depth-of-field-tutorial/.

Yaguchi, Masatsugu, Takashi Ogata, and Takayuki Sakai. 2010. “Creep Strength of High Chromium Steels Welded Parts under Multiaxial Stress Conditions.” *International Journal of Pressure Vessels and Piping* 87 (6). Elsevier Ltd: 357–64. doi:10.1016/j.ijpvp.2010.03.018.

Yu, Hai, Rongxin Guo, Haiting Xia, Feng Yan, Yubo Zhang, and Tianchun He. 2014. “Application of the Mean Intensity of the Second Derivative in Evaluating the Speckle Patterns in Digital Image Correlation.” *Optics and Lasers in Engineering* 60. Elsevier: 32–37. doi:10.1016/j.optlaseng.2014.03.015.

Zyl, F. H. van, G. von dem Bongart, M. E. J. Bezuidenhout, P. Doubell, F. C. Havinga, D. A. H. Pegler, M. Newby, and W. Smit. 2005. “Life Assessment and Creep Damage Monitoring of High Temperature Pressure Components in South Africa’s Power Plant.” In *ECCC Creep Conference*, 934–45.

4.4 Imager E-lite 5M

Category	E-lite 5M
art. no.	1101132
resolution (h×v)	2456 pixel×2058 pixel
sensor type	Sony ICX625
optical size	2/3”
pixel size	3.45 $\mu m \times 3.45\ \mu m$
active area	$8.5 \times 7.1\ mm^2$
spectral range	400-850 nm
full well capacity	7,000 e^-
max. frame rate (at full resolution)	12.2 fps
noise	13 e^-
binning	yes
partial scan	yes
data output type	Gigabit ethernet (1000 Mbits/s)
ADC bit depth	12 bit
synchronization	via ext. trigger
exposure control	programmable
power requirements	+12 to +24 VDC, $\leq$1% ripple
	$\leq$5 W @ 12 V
I/O ports	2 opto-isolated input ports and 4 opto-isolated output ports
lens adapter	CS mount
size (l x w x h)	86.7 mm×44 mm×29 mm (without lens adapter or connectors)
weight	220 g
conformity	CE, FCC, ROHS, IP30

TC23009

Bi-telecentric lens for 2/3" detectors, magnification 1.000 x, C-mount

SPECIFICATIONS

Magnification	(×)	1.000
Image circle Ø	(mm)	11.0

Object field of view (8)		
with 1/3" detector (4.8 x 3.6 mm)	(mm × mm)	4.80 x 3.60
with 1/2.5" detector (5.70 x 4.28 mm)	(mm × mm)	5.70 x 4.28
with 1/2" detector (6.4 x 4.8 mm)	(mm × mm)	6.40 x 4.80
with 1/1.8" detector (7.13 x 5.37 mm) (7)	(mm × mm)	7.13 x 5.37
with 2/3" - 5 MP detector (8.45 x 7.07 mm)	(mm × mm)	8.44 x 7.06

Optical specifications		
Working distance (1)	(mm)	62.2
wF/# (2)		11
Telecentricity typical (max) (3)	(deg)	< 0.08 (0.10)
Distortion typical (max) (4)	(%)	< 0.04 (0.08)
Field depth (5)	(mm)	0.9
CTF @ 70 lp/mm	(%)	> 25

Dimensions		
Mount		C
Length (6)	(mm)	65.0
Diameter	(mm)	28
Mass	(g)	160

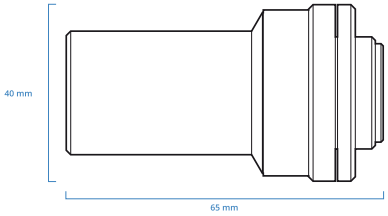

NOTES

1. Working distance: distance between the front end of the mechanics and the object. Set this distance within +/- 3% of the nominal value for maximum resolution and minimum distortion.
2. Working F-number (wF/#): the real F-number of a lens when used as a macro. Lenses with smaller apertures can be supplied on request.
3. Maximum slope of chief rays inside the lens: when converted to millirad, it gives the maximum measurement error for any millimeter of object displacement. Typical (average production) values and maximum (guaranteed) values are listed.
4. Percent deviation of the real image compared to an ideal, undistorted image: typical (average production) values and maximum (guaranteed) values are listed.
5. At the borders of the field depth the image can be still used for measurement but, to get a very sharp image, only half of the nominal field depth should be considered. Pixel size used for calculation is 5.5 µm.
6. Measured from the front end of the mechanics to the camera flange.
7. With 1/1.8" (9 mm diagonal) detectors, the FOV of TC12yyy lenses may show some vignetting at the image corners, as these lenses are optimized for 1/2" detectors (8 mm diagonal).
8. For the fields with the indication "Ø =", the image of a circular object of such diameter is fully inscribed into the detector.

COMPATIBLE PRODUCTS

LTCLHP series
High-performance telecentric illuminators

LTCLHP023-R	Telecentric HP illuminator, beam diameter 16 mm, red
LTCLHP023-G	Telecentric HP illuminator, beam diameter 16 mm, green
LTCLHP023-B	Telecentric HP illuminator, beam diameter 16 mm, blue
LTCLHP023-W	Telecentric HP illuminator, beam diameter 16 mm, white

LTRN series
LED ring illuminators

LTRN023RD	Ring LED illuminator, inner diameter 28 mm, straight type, red 630 nm
LTRN023GR	Ring LED illuminator, inner diameter 28 mm, straight type, green 525 nm

LTRN023BL	Ring LED illuminator, inner diameter 28 mm, straight type, blue 470 nm
LTRN023NW	Ring LED illuminator, inner diameter 28 mm, straight type, white
LTRN075R45	Ring LED illuminator, inner diameter 28 mm, oblique type, red 630 nm
LTRN075G45	Ring LED illuminator, inner diameter 28 mm, oblique type, green 525 nm
LTRN075B45	Ring LED illuminator, inner diameter 28 mm, oblique type, blue 470 nm
LTRN075W45	Ring LED illuminator, inner diameter 28 mm, oblique type, white

LTDM series
Diffusive strobed dome illuminators

LTDMA1-R	Diffusive strobed dome illuminator - small size medium power red
LTDMA1-G	Diffusive strobed dome illuminator - small size medium power green
LTDMA1-W	Diffusive strobed dome illuminator - small size medium power white

CMHO series
Clamping mechanics

CMHO023	Clamping mechanics for TCxx004, 007, 009, 012 and LTCLHP023-X

Calibration patterns
Accurate calibration of machine vision systems

PT004-009	Calibration pattern

IMP Calibration Services (Pty) Ltd

HEAD OFFICE Tel: +27 (11) 916 5000 • Fax: +27 (11) 914 4509 DURBAN Tel: +27 (31) 764 2821
Fax: +27 (31) 764 4288 WESTERN CAPE Tel: +27 (21) 852 6133 • Fax: +27 (21) 852 6129 EASTERN CAPE
Tel: +27 (41) 364 2544 • Fax: +27 (41) 364 2544 FREE STATE Tel +27 (18) 293 3333 • Fax: +27 (18) 293 3333
MPUMALANGA Mobile: +27 82 526 9737 • Mobile: +27 82 600 9740 ADDRESS: Cnr Commissioner and
Christopher Street, Boksburg, 1459 • PO Box 1110, Boksburg, 1460, South Africa
E-mail: info@imp.co.za • Website: www.imp.co.za

sanas Calibration Laboratory 816 1416

IMP Innovative Solutions

Company Reg No: 2016/047509/07

VAT Reg. No: 4210273431

ON SITE CALIBRATION CERTIFICATE
OF A UNIVERSAL TESTING MACHINE
SANAS ACCREDITED LABORATORY FOR FORCE - NO: 816

CALIBRATION CERTIFICATE NUMBER: SHQ-56868 C

COMPANY:	**UNIVERSITY OF STELLENBOSCH**
CONTACT PERSON:	**DR. THORSTEN BECKER**
PHYSICAL ADDRESS:	**BANHOEK WEG, STELLENBOSCH**
LOCATION OF CALIBRATION:	**UNIVERSITY OF STELLENBOSCH, MECHANICAL LABORATORY ROOM 135**
DATE CALIBRATED:	**2016-11-10**
CALIBRATED BY:	**STEFAN ZIETSMAN**
ITEM CALIBRATED:	**UNIVERSAL TESTING MACHINE**
MANUFACTURER:	**MTS**
MODEL NUMBER:	**C44**
UNIVERSAL TESTER SERIAL NUMBER:	**05000076**
LOAD CELL SERIAL NUMBER:	**376349**
CAPACITY OF MACHINE:	**30 kN**
RESOLUTION OF MACHINE:	**0.001 kN**
RANGE CALIBRATED:	**0 kN TO 30 kN**
STANDARD USED:	**50 kN LOAD CELL (159198/CPT0001)**
TRACEABILITY NUMBER:	**IHQ-46057 H**
PROCEDURE FOLLOWED:	**IMP 1001**
CALCULATED UNCERTAINTY:	**± 0.26% OF READING**

The accuracy's of the standards used are, by way of regular inter-comparison, traceable to National Standards, within the limitations of the services available. The values in the certificate are correct at the time of calibration. Subsequently the accuracy will depend on such factors as the care exercised in handling as well as use of instruments, equipment and the frequency of use. IMP Calibration Services (Pty) Ltd cannot be held responsible for values changing, and are therefore not liable except for the recalibration of the equipment where we accept responsibility. No long term stability checks were carried out. This certificate automatically expires if the instrument is repaired or if the seal is broken.

CALIBRATION CERTIFICATE NUMBER: SHQ-56868 C

Results:

TEMPERATURE	1	20.6 °C
	2	20.6 °C
	3	20.6 °C

Reproduceability

Step	UUT	STD			AVERAGE	CORRECTION OF READING
	kN	kN			kN	kN
1	0.000	0.000	0.000	0.000	0.000	0.000
2	15.000	15.021	15.036	15.042	15.033	0.033
3	18.000	18.018	18.033	18.040	18.030	0.030
4	21.000	21.022	21.036	21.045	21.034	0.034
5	24.000	24.022	24.040	24.049	24.037	0.037
6	27.000	27.028	27.045	27.055	27.043	0.043
7	30.000	30.030	30.047	30.059	30.045	0.045

Remarks:

1.) The reported expanded uncertainty is based on a standard uncertainty multiplied by a coverage factor k = 2 providing a level of confidence of approximately 95%, the uncertainty of measurement has been esitmated in accordance with the principles defined in the GUM, Guide to Measurement, ISO, Geneva, 1993.

2.) The calibration was performed in compression.

3.) The machine was not adjusted.

4.) The STD Load Cell was not rotated.

Checked by:

S. CILLERS — Name

Technician — Designation

 — Signature

Authorized by:

 — Name

Technical Signatory — Designation

 — Signature

Date issued: 23/6/2017

**********END**********

IMP Calibration Services (Pty) Ltd

HEAD OFFICE Tel: +27 (11) 916 5000 · Fax: +27 (11) 914 4509 DURBAN Tel: +27 (31) 764 2821
Fax: +27 (31) 764 4288 WESTERN CAPE Tel: +27 (21) 852 6133 · Fax: +27 (21) 852 6129 EASTERN CAPE
Tel: +27 (41) 364 2544 · Fax: +27 (41) 364 2544 FREE STATE Tel +27 (18) 293 3333 · Fax: +27 (18) 293 3333
MPUMALANGA Mobile: +27 82 526 9737 · Mobile: +27 82 600 9740 ADDRESS: Cnr Commissioner and
Christopher Street, Boksburg, 1459 · PO Box 1110, Boksburg, 1460, South Africa
E-mail: info@imp.co.za · Website: www.imp.co.za

Company Reg No: 2016/047509/07

VAT Reg. No: 4210273431

ON SITE CALIBRATION CERTIFICATE
OF A UNIVERSAL TESTING MACHINE
SANAS ACCREDITED LABORATORY FOR FORCE - NO: 816

CALIBRATION CERTIFICATE NUMBER: SHQ-56868 A

COMPANY:	**UNIVERSITY OF STELLENBOSCH**
CONTACT PERSON:	**DR. THORSTEN BECKER**
PHYSICAL ADDRESS:	**BANHOEK WEG, STELLENBOSCH**
LOCATION OF CALIBRATION:	**UNIVERSITY OF STELLENBOSCH, MECHANICAL LABORATORY ROOM 135**
DATE CALIBRATED:	**2016-11-10**
CALIBRATED BY:	**STEFAN ZIETSMAN**
ITEM CALIBRATED:	**UNIVERSAL TESTING MACHINE**
MANUFACTURER:	**MTS**
MODEL NUMBER:	**C44**
UNIVERSAL TESTER SERIAL NUMBER:	**05000076**
LOAD CELL SERIAL NUMBER:	**376349**
CAPACITY OF MACHINE:	**30 kN**
RESOLUTION OF MACHINE:	**0.001 kN**
RANGE CALIBRATED:	**0 kN TO 30 kN**
STANDARD USED:	**50 kN LOAD CELL (159198/CPT0001)**
TRACEABILITY NUMBER:	**IHQ-46057 G**
PROCEDURE FOLLOWED:	**IMP 1001**
CALCULATED UNCERTAINTY:	**± 0.24% OF READING**

The accuracy's of the standards used are, by way of regular inter-comparison, traceable to National Standards, within the limitations of the services available. The values in the certificate are correct at the time of calibration. Subsequently the accuracy will depend on such factors as the care exercised in handling as well as use of instruments, equipment and the frequency of use. IMP Calibration Services (Pty) Ltd cannot be held responsible for values changing, and are therefore not liable except for the recalibration of the equipment where we accept responsibility. No long term stability checks were carried out. This certificate automatically expires if the instrument is repaired or if the seal is broken.

CALIBRATION CERTIFICATE NUMBER: SHQ-56868 A

Results:

TEMPERATURE	1	20.5 °C
	2	20.5 °C
	3	20.5 °C

Reproduceability

Step	UUT	STD			AVERAGE	CORRECTION OF READING
	kN	kN			kN	kN
1	0.000	0.000	0.000	0.000	0.000	0.000
2	15.000	15.055	15.056	15.054	15.055	0.055
3	18.000	18.062	18.065	18.065	18.064	0.064
4	21.000	21.076	21.076	21.078	21.077	0.077
5	24.000	24.086	24.089	24.086	24.087	0.087
6	27.000	27.097	27.100	27.097	27.098	0.098
7	30.000	30.104	30.108	30.110	30.107	0.107

Remarks:

1.) The reported expanded uncertainty is based on a standard uncertainty multiplied by a coverage factor k = 2 providing a level of confidence of approximately 95%, the uncertainty of measurement has been esitmated in accordance with the principles defined in the GUM, Guide to Measurement, ISO, Geneva, 1993.

2.) The calibration was performed in tension.

3.) The machine was not adjusted.

4.) The STD Load Cell was not rotated.

Checked by:

S. CILLIERS — Name

Technician — Designation

 — Signature

Authorized by:

 — Name

Technical Signatory — Designation

 — Signature

Date issued: 23/4/2024

**********END**********

DOMEX®
HIGH STRENGTH STEEL

Domex 355 MC

High Strength Cold Forming Steel

General Product Description

Domex 355 MC is a hot-rolled structural steel with a minimum yield strength of 355 MPa. Domex 355 MC meet and exceed the requirements of S355 MC in EN 10149-2.

Applications

Typical applications are components subjected to demanding forming operations.

Available dimensions

Domex 355 MC is available in thicknesses of 1.80-15.00 mm and widths up to 1600 mm as coils, slit coils and as cut to length in lengths up to 16 meters.

Mechanical Properties

Steel grade	Yield strength R_{eH} (MPa)	Tensile strength R_m (MPa)		Elongation A_{80} % t < 3 mm	Elongation A_5 % t ≥ 3 mm
	min	min	max	min	min
Domex 355 MC	355	430	550	19	23

The mechanical properties are valid in the longitudinal direction.

Impact toughness

	Designation	Test temperature (°C)	Impact energy (J)
Min. impact energy for longitudinal Charpy V-notch test	B	Not tested	
	D	- 20	40
	E	- 40	27

Impact testing according to ISO 148-1 is performed on thicknesses ≥ 6mm. The specified minimum value corresponds to a full-size specimen.

Bending properties

	Sheet thickness, t		
	t ≤ 3 mm	3 mm < t ≤ 6 mm	t > 6 mm
Min. inner bending radius for a 90° bend	0.2 xt	0.3 xt	0.5xt

For both longitudinal and transversal directions.

SSAB

Chemical Composition (Ladle analysis)

C % max	Si % max	Mn % max	P % max	S % max	Al_{tot} % min	Nb % max	V % max	Ti % max	CEV typical	CET typical
0.10	0.03 [1)]	1.50	0.025	0.010	0.015	0.09 [2)]	0.20 [2)]	0.15 [2)]	0.17	0.12

1) Domex 355 MC meets the requirements of category A (thin coatings) for hot-dip zinc-coating in EN 10149-2. Category B for thick coatings is available on request (Si 0.15-0.21%).
2) The sum of Nb, V and Ti is max 0.22%.
The steel is grain refined.

Tolerances

Domex 355 MC is supplied with tolerances in accordance with EN 10051. More narrow tolerances according to the SSAB standard are available on request.

Delivery condition

Thermomechanically rolled.

Surface and edge condition

Domex 355 MC is available in as rolled or pickled surface condition with mill or cut edge.

Fabrication and other recommendations

Domex 355 MC is a cold forming steel not suited for heat treatments at temperatures above 580°C, since the material then may lose its guaranteed properties.

Domex 355 MC has good welding, cold forming and cutting performance.

For information concerning fabrication, see SSAB's brochures on www.ssab.com or consult Tech Support, help@ssab.com.

Appropriate health and safety precautions must be taken when bending, welding, cutting, grinding or otherwise working on the product.

Contact and Information

Tech Support will be pleased to assist you with additional information concerning this SSAB product.